A light-sheet microscope for imaging living biomimetics

Narag, Jadze Princeton C.

Publication date:
2024

Document Version
Publisher's PDF, also known as Version of record

Citation (APA):
Narag, J. P. C. (2024). *A light-sheet microscope for imaging living biomimetics*. DTU Health Technology.

DTU

Technical University of Denmark

A light-sheet microscope for imaging living biomimetics

PhD thesis

by Jadze Princeton Narag

DTU Health Tech
Department of Health Technology

Technical University of Denmark

PhD Thesis

A light-sheet microscope for imaging living biomimetics

Author:
Jadze Princeton C. Narag

Supervisors:
Emil B. Kromann
Niels B. Larsen
Jens E. Wilhjelm

April 2023

Kongens Lyngby, Denmark

Cover image: Laser combiner of the MOSAIC microscope. The laser combiner is used to align seven excitation lasers for various fluorescence microscopy modes in the MOSAIC microscope.

Preface

This PhD thesis has been submitted to the Department of Health Technology at the Technical University of Denmark (DTU) as part of the requirements for obtaining a PhD degree. The research forming the basis for this thesis was carried out over a period of three and a half years, from 01 August 2019 to 31 January 2023, in the Department of Health Technology at DTU.

This project was completed with the guidance and support of my supervisors, Associate Professor Emil B. Kromann, Professor Niels B. Larsen, and Professor Jens E. Wilhjelm. External research was conducted for a period of three months at the Harvard Medical School, under the supervision of Professor Tomas Kirchhausen and Ricardo Bango Da Cunha Correia.

Abstract

The ability to accurately simulate the structure and function of organs is essential in the analysis of diseases, the modeling of human development, and the development of therapeutic treatments. As such, considerable efforts have been made towards creating 3D biomimetic cultures, which provide a more accurate representation of a cell's natural environment than 2D cultures. However, the intricate structure of 3D cultures makes them difficult to image. A method must be employed that enables deep imaging with a wide field of view while minimizing phototoxicity for long-term imaging.

Light-sheet microscopy (LSM) is an ideal imaging method for living samples as it provides optical sectioning, a wide field of view, and minimal phototoxicity. Lately, a new type of microscopy called lattice light-sheet microscopy (LLSM) has emerged. This technique involves the use of a light-sheet created by coherent superposition of Bessel beams, providing a compromise between light-sheet thickness and sidelobe energy density.

The MOSAIC (multimodal optical scope with adaptive imaging correction) microscope integrates LLSM with other microscopy modes into a single instrument. It was developed by Eric Betzig’s group in Janelia Research Campus. Furthermore, the MOSAIC is equipped with adaptive optics to correct for aberrations and provides benefits such as high axial resolution and minimal photobleaching and photodamage.

This thesis focuses on the construction of the LLSM imaging mode in the MOSAIC microscope, its optimization process, and its application for imaging 3D biomimetic cultures. The design behind the MOSAIC relies on modular custom-made components, making the building process straightforward. However, the lattice light-sheet (LLS) mode in the MOSAIC is complex due to the presence of other imaging modes that share components with the LLS optical path. This complexity can lead to an increase in optical aberrations in the instrument.

During the construction of the LLS, some complexities and issues were encountered that were resolved and documented. Most notably, these include design errors in the custom-made components, the absorption of fluorescence dye by the detection objective, and the shift in the light-sheet when aligning with water compared to medium.

Optimizations were carried out to ensure optimal imaging with the instrument. The optimizations include calibrating the spatial light modulator (SLM) for uniform excitation. Additionally, system aberrations are corrected with pupil wavefront correction (PWFC) using the SLM and phase retrieval algorithm using the deformable mirror. The instrument was also optimized for long-term imaging of living samples by incorporating temperature, CO_2, and evaporation controls in the sample chamber.

Three imaging experiments were performed that demonstrated our capability to image both 2D and 3D cultures, showcasing the versatility of the instrument in capturing a wide range of spatiotemporal dynamics, including subcellular vesicle movement and multi-cellular structure of a biomimetic skin culture.

The results showed that living samples can be maintained for a substantial time of 6 hours, but the image quality was impacted by cell degradation and bleaching. We found that the scanning direction of the sample is crucial in imaging 2D versus 3D samples. For 2D samples, a simple translation along the x-axis (horizontal) was sufficient. While for 3D samples, scanning along the xz-axis (detection objective optical axis) was necessary to image deeper structures. Although scanning along the xz-axis provides a limited field of view (FOV), a tiling technique was used to address it. The methods for creating 3D renderings from the images obtained by different scanning directions differ and require different pre-processing. Moreover, the sample mounting process for 3D samples was challenging but was accomplished using a fibrinogen/thrombin glue.

The PSF (point spread function) was measured in the LLS and compared to that of a spinning disk microscope. The measured full width at half maximum (FWHM) of the PSF in the LLS were found to be 325 nm, 316 nm, and 738 nm in the x, y, and z axes, respectively, matching the expected (theoretical) FWHM of 285 nm in the x and y axes and 700 nm in the z-axis.

Interestingly, because of the configuration of the objectives in the LLS, the PSF is rotated relative to the sample coordinates. This leads to an apparent improvement in z-resolution in the sample coordinates. This improved z-resolution was quantified by deriving an equation that indicates a resolution of 649 nm in the sample coordinates.

Tracking of clathrin-coated pits (CCPs) was employed as a demonstration of the wealth of data (e.g., position distributions and movement speeds) that can be extracted with 3D LLS imaging and subsequent image analysis.

The MOSAIC is a useful instrument for imaging 3D cultures, but its design still has some limitations that need to be addressed in future research and development. The results of this thesis provide valuable insights and information for using and improving the design of the MOSAIC microscope.

Danish abstract

Evnen til nøjagtigt at simulere strukturen og funktionen af organer er afgørende i analyse af sygdomme, modellering af menneskelig udvikling og udvikling af terapeutiske behandlinger. Af denne grund, er der inden for den seneste årrække gjort en betydelig indsats for at skabe 3D-biomimetiske kulturer, som giver en mere nøjagtig repræsentation af en celles naturlige miljø end 2D-kulturer. Dog gør den indviklede struktur af 3D-kulturer svær at afbilde med den nuværende teknologi inden for mikroskopi. Deraf er der behov for en metode, der muliggør dyb billeddannelse med et bredt synsfelt og samtidig minimerer fototoksicitet ved billeddannelse over lange tidsperioder.

Light-sheet microscopy (LSM) er en ideel billeddannelsesmetode til levende prøver, da den giver optisk tværsnit, et bredt synsfelt og minimal fototoksicitet. På det seneste er der opstået en ny type mikroskopi kaldet lattice light-sheet microscopy (LLSM). Denne teknik involverer brugen af et ” lysplan” der skabes ved at overlejre Bessel-stråler, hvilket giver et kompromis mellem tykkelsen af lysplanet og lysintensiteten i omkringliggende planer.

MOSAIC-mikroskopet (multimodal optical scope with adaptive imaging correction) integrerer LLSM med andre mikroskopitilstande i et enkelt instrument. Det er udviklet af Eric Betzigs gruppe på Janelia Research Campus. Desuden er MOSAIC udstyret med adaptiv optik til at korrigere for optiske strålebaneforvrængninger og giver fordele såsom høj aksial opløsning og relativt lav fotoblegning og fotoskader.

Denne afhandling fokuserer på konstruktionen af LLSM-billeddannelsestilstanden i MOSAIC-mikroskopet, dens optimeringsproces og dens anvendelse til billeddannelse af 3D-biomimetiske kulturer. Designet bag MOSAIC bygger på modulære specialfremstillede komponenter, hvilket gør byggeprocessen enkel og nem at tilpasse. Light-sheet lattice-tilstanden (LLS) i MOSAIC er imidlertid kompleks på grund af tilstedeværelsen af andre billeddannelsestilstande, der deler komponenter med den optiske LLS-vej. Denne kompleksitet kan føre til en stigning i optiske aberrationer i instrumentet.

Under opbygningen af LLS opstod der komplekse problemstillinger, som blev løst og dokumenteret. Mest bemærkelsesværdigt er disse fejl opstået ved brug af de specialbyggede

komponenter ved absorptionen af fluorescensfarve af detektionsobjektivet og forskydning af lysplanet ved kalibrering med vand frem for medium.

Der blev udført optimeringer for at sikre optimal billeddannelse med instrumentet. Disse optimeringer omfatter kalibrering af spatial light modulatoren (SLM) til ensartet excitation og korrigering af systemaberrationer (optiske strålebaneforvrængninger i selve mikroskopet) med pupil wavefront correction (PWFC) ved hjælp af en SLM og et deformerbart spejl. Instrumentet blev også optimeret til langvarig billeddannelse af levende prøver ved at inkorporere temperatur-, CO_2- og fordampningskontrol i prøvekammeret.

Der blev udført tre billeddannelseseksperimenter, der demonstrerede evnen til at afbilde både 2D- og 3D-kulturer, hvilket viser instrumentets alsidighed til at fange en bred vifte af spatiotemporal dynamik, herunder subcellulær vesikelbevægelse og multicellulær struktur af en biomimetisk hudkultur.

Resultaterne viste, at levende prøver kan opretholdes i et betydeligt tidsrum på 6 timer, men billedkvaliteten/relevansen blev påvirket af celledød og blegning. Vi fandt ud af, at scanningsretningen af prøven er afgørende ved billeddannelse af 2D versus 3D prøver. For 2D-prøver var en simpel translation langs x-aksen (vandret) tilstrækkelig. Mens for 3D-prøver var scanning langs xz-aksen (detektionsobjektivets symmetriakse) nødvendig for at afbilde dybere strukturer. Da scanning langs xz-aksen giver et begrænset synsfelt (FOV), blev der brugt en ”fliseteknik” til at adressere det. Metoderne til at skabe 3D-gengivelser fra billederne er opnået ved at implementere forskellige scanningsretninger og kræver deraf forskellig forbehandling. Desuden var prøvemonteringsprocessen for 3D-prøver udfordrende. Denne blev løst ved hjælp af en fibrinogen-/trombin-lim.

PSF’en (punktspredningsfunktion) blev målt i LLS og sammenlignet med PSF’en i et spinning disk mikroskop. Den målte størrelse (full width at half maximum, FWHM) af PSF’en i LLS var 325 nm, 316 nm og 738 nm langs hehv. x-, y- og z-akserne, hvilket matcher de forventede (teoretiske) FWHM-dimensioner: 285 nm langs x- og y-akserne og 700 nm langs z-aksen.

På grund af den geometriske konfiguration af objektiverne i LLS, roteres PSF’en i forhold til prøvekoordinaterne. Dette fører til en tilsyneladende forbedring i z-opløsning i

prøvekoordinaterne. Denne forbedrede z-opløsning blev kvantificeret ved at udlede en ligning, der indikerer en øget opløsning på 649 nm i prøvekoordinaterne.

Desuden blev sporingen (tracking) af clathrin-coated pits (CCP'er) brugt til at demonstrere det væld af information (e.g, distributioner af position og bevægelse), der kan udvindes fra 3D LLS-billeddannelse og efterfølgende billedanalyse.

MOSAIC er et nyttigt instrument til billeddannelse af 3D-kulturer, men dets design har stadig nogle begrænsninger, som skal behandles i fremtidig forskning og udvikling. Resultaterne af denne afhandling giver værdifuld indsigt og information til brug og forbedring af designet af MOSAIC-mikroskopet.

Acknowledgements

I would like to express my gratitude to my supervisors, Emil B. Kromann, Niels B. Larsen, and Jens E. Wilhjelm, for their invaluable guidance and support throughout my PhD journey. Your insightful feedback, constructive criticism, and constant encouragement have helped me to develop both as a researcher and as an individual. I would also like to thank my labmates, Jaco, Yingchao, Carl Emil, and Lasse, for their invaluable assistance, stimulating discussions, and unwavering support. Their friendship and camaraderie have made the lab a welcoming and inspiring place to work.

I am grateful to Tom and Ricardo, and Gu for the opportunity to learn firsthand how to build the MOSAIC and for their hospitality during my stay in Boston. The experience of working in a world-class research institution has been enriching and inspiring. I would also like to thank my collaborators, Jannik, Philip, Adam, Arjen, Mikkel, Fawzi, and Sally, for their contributions in providing biological samples to image with the instrument and for sharing their expertise in biology. Their insights have been invaluable in interpreting the imaging results.

I would like to extend my gratitude to my friends: Leonid, Alex, Pratik, Eduard, Carlos, Einstom, Marisse, Joji, Ian, for their support, encouragement, and laughter. I am grateful for the memories we have shared and for their unwavering friendship.

Finally, I would like to express my sincere gratitude to Laura for her unwavering support and encouragement throughout this journey. Her patience in reading and providing feedback on countless drafts of this thesis has been invaluable. I am also grateful to Frederik for his assistance in translating the abstract into Danish.

List of figures

List of abbreviations

AAAS	-	American association for the advancement of science
AO	-	adaptive optics
AOTF	-	acousto-optic tunable filter
AP2	-	activator protein 2
BRIC	-	Biotech research & innovation centre
BsmBI	-	bacillus stearothermophilus restriction endonuclease B
CaCl2	-	calcium chloride
Caco-2	-	immortalized cell line of human colorectal adenocarcinoma cells
CCP	-	clathrin coated pits
CME	-	clathrin mediated endocytosis
CO2	-	carbon dioxide
CRISPR	-	clustered regularly interspaced short palindromic repeats
DK	-	Denmark
DM	-	deformable mirror
DMEM	-	Dulbecco's modified eagle medium
DNA	-	deoxyribonucleic acid
DSLM	-	digitally scanned light-sheet microscopy
DTU	-	Technical University of Denmark
ECM	-	extracellular matrix
EFL	-	effective focal length
EGF	-	epidermal growth factor
eGFP	-	enhanced green fluorescence protein
FBS	-	fetal bovine serum
FCS	-	fetal calf serum
FEP	-	fluorinated ethylene propylene
FLIM	-	fluorescence lifetime imaging microscopy
FLIP	-	fluorescence loss in photobleaching
FOV	-	field of view
FPGA	-	field-programmable gate array
FRAP	-	fluorescence recovery after photobleaching

FRET - fluorescence resonance energy transfer
FWHM - full width at half maximum
GPP - genetic perturbation platform
gRNA - guide RNA
GS - Gerchberg-Saxton
HEPES - 4-(2-hydroxyethyl)-1-piperazineethanesulfonic acid
ISC - intersytem crossing
KO - knock out
LLS - lattice light-sheet
LLSM - lattice light-sheet microscopy
LSCM - laser scanning confocal microscopy
LSFM - light-sheet-based fluorescence microscopy
LSM - light-sheet microscopy
MEM - minimum essential medium
MGAT1 - mannosyl (alpha-1,3-)-glycoprotein Beta-1,2-N-acetylglucosaminyltransferase
MIP - maximum intensity projection
MOSAIC - multimodal optical scope with adaptive imaging correction
NHBE - normal human bronchial epithelial
OSM - organotypic skin model
PBS - phosphate-buffered saline
PE - polaris elliptical mirror
PMT - photomultiplier tube
PS - penicillin-streptomycin
PSF - point spread function
PWFC - pupil wavefront correction
ROIs - regions of interest
ROS - reactive oxygen species
SH - Shack-Hartmann
SIM - structured illumination microscopy
SLM - spatial light modulator
SMAD - Sma and Mad-related proteins
SNR - signal-to-noise ratio

SPIM	-	selective plane illumination microscopy
SVGA	-	immortalized cell line derived from human astrocyte
TERT	-	telomerase reverse transcriptase
TGF	-	transforming growth factor
UCPH	-	University of Copenhagen
WD	-	working distance
WFM	-	widefield fluorescence microscopy
WT	-	wild type

Table of contents

Chapter 1. Introduction

1.1 Biomimetics and 3D cell culture

The capacity to precisely simulate the structure and function of organs is crucial in disease analysis, human development modeling, and therapeutic treatment development. As a result, significant efforts have been directed towards modeling key organs such as the gut [1-2], brain [3-4], kidney [5], [6], liver, and lungs [7], [8]. Using these 3D biomimetic cultures, it has been possible to model viral infection [9], to study brain corticogenesis [10], and to establish a personalized screening that identifies the most effective drug for patients with cystic fibrosis [11].

Biomimetic cultures are sometimes referred to as 3D culture, organoid culture, organotypic culture, or organ-on-chips – interchangeably or distinctly depending on the specific field of research. **Figure 1.1** illustrates these terms and their usage to describe different models. **Figure 1.1a** depicts a 2D culture, which involves cells seeded on a flat surface whereas **Figure 1.1b-d** illustrate various 3D cultures. A spheroid is a 3D culture that refers to a collection of multiple cells that often assemble in a nearly spherical form, as cells tend to stick to each other rather than the surrounding environment when engineered correctly. On the other hand, an organoid is a group of cells taken from a specific organ, and typically contains different types of cells from that organ to imitate more of the organ's natural functions. **Figure 1.1c** represents a 3D culture in a transwell insert, which is frequently referred to as a transwell culture. These cultures have a mechanical support on the bottom, in the form of a porous material that allows for diffusion. Transwell cultures effectively mimic biological barriers, such as the skin. **Figure 1.1d** depicts a 3D culture with microfluidic perfusions that deliver medium to the 3D culture and are often referred to as microfluidic cultures or organ-on-a-chip. These types of cultures are useful in modeling 3D vascularization. Several discussions of 3D cultures have been written elsewhere [12-16]. Here, I focus on discussing the challenges and the requirements in imaging biomimetic cultures.

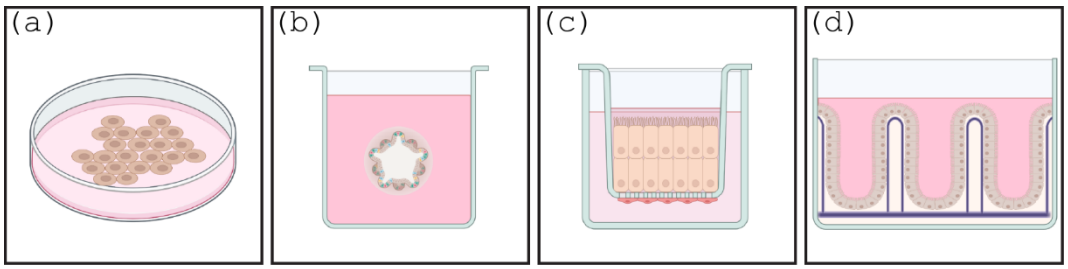

***Figure 1.1. Biomimetic cultures**. **(a)** 2D culture. **(b)** 3D organoid culture. **(c)** 3D transwell culture. **(d)** 3D organ-on-a-chip culture.*

One of the advantages of 3D cultures over 2D cultures is that they more accurately model the architecture and composition of the natural environment of cells. However, 3D cultures are more challenging to image compared to flat 2D cultures. The structure of 3D cultures in some cases is composed of different layers of cells or biomaterials with various optical properties. It is challenging to image through these layers because they degrade the image quality by scattering or refraction of light. Moreover, imaging 3D cultures requires the ability to quickly survey large volumes and to image over extended periods of time.

To effectively image 3D cultures, a variety of requirements must be met. The imaging method must allow for imaging deep into multi-layered samples with a broad field of view, while minimizing phototoxicity to allow for long-term imaging. Additionally, the use of a sample chamber with environmental control is desirable to maintain the integrity and viability of the living 3D culture during imaging.

In the following sections of this chapter, I provide an overview of the most common imaging techniques for 2D and 3D cultures, including confocal microscopy, widefield microscopy, and light-sheet microscopy. Next, I describe a novel light-sheet microscope that I have built. Finally, I describe the structure and goals of this thesis.

1.2 Common imaging techniques

1.2.1 Fluorescence microscopy

Fluorescence microscopy is an imaging technique that utilizes the properties of fluorescence, a phenomenon where molecules re-emit light after absorbing it. The sample is illuminated with light of a specific wavelength, typically using a high-intensity light source such as high-power LEDs or lasers. Then, the fluorescent molecules in the sample emit light of a different, longer wavelength, which is captured in the microscope and used to form an image. The resulting fluorescence image provides information about the distribution and localization of the fluorescent probes and, by extension, the molecules they are bound to. This information can be used to study a wide range of biological processes, such as cell signaling, gene expression, protein-protein interactions, and more. There are several different types of fluorescence microscopy, each with its own advantages and limitations. These include confocal fluorescence microscopy, widefield fluorescence microscopy, and light-sheet microscopy, among others.

1.2.2 Widefield and confocal fluorescence microscopy

The two most prevalent modes of fluorescence microscopy are widefield fluorescence microscopy (WFM) and laser scanning confocal microscopy (LSCM). A schematic representation of these two modes is shown in **Figure 1.2**. Excitation light comes from the side and is redirected downward by a dichroic mirror. The dichroic mirror is designed to reflect light with shorter wavelengths while transmitting longer wavelengths. This separation of the excitation light and the emitted fluorescence is crucial in fluorescence microscopy. The excitation light is focused onto the sample by an objective lens, inducing fluorescence in the sample. The emitted fluorescence is then collected by the same objective lens and directed towards a detection device.

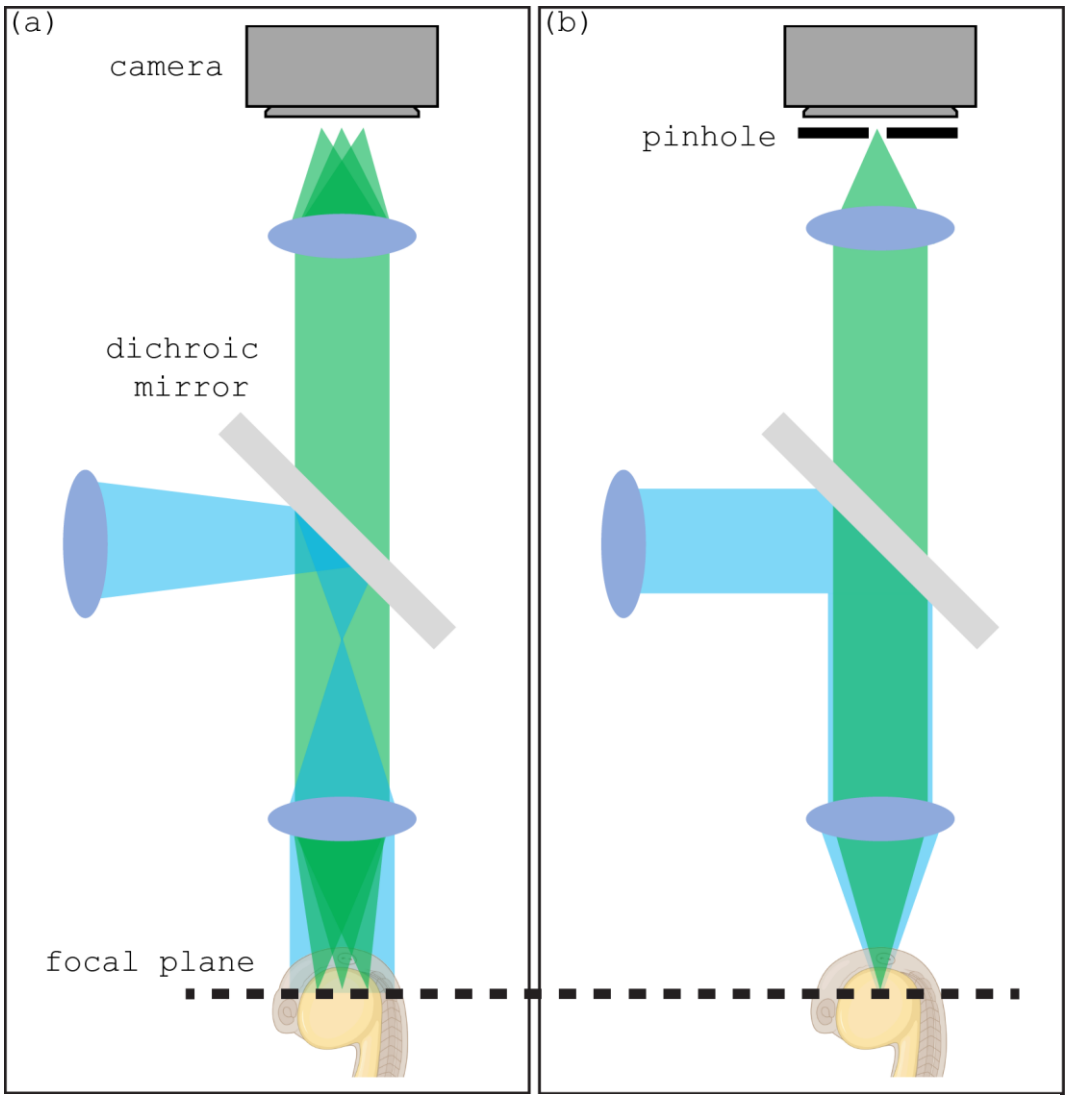

Figure 1.2. Widefield and confocal microscopy setup. (a) *In the widefield setup, the whole field of view is illuminated.* ***(b)*** *In the confocal setup, an excitation point is scanned throughout the sample. The pinhole in front of the detector blocks out-of-focus light and provides optical sectioning.*

In WFM, the excitation beam illuminates a large region within the sample, but the image is sharp for only one plane, namely the focal plane of the detection objective. Emitted fluorescence from planes other than the focal plane causes blurring in the image. In contrast, LSCM uses a focused excitation beam that illuminates a spot in the focal plane of the objective. The emitted fluorescence is focused back to the detector, with a pinhole being used to block out-of-focus blurring caused by light originating from other locations than the focal plane.

The detection is also different between widefield fluorescence microscopy and laser scanning confocal microscopy. For WFM, the signal is directly captured with a camera and the output is an image that can be interpreted directly. For LSCM, the excitation light is focused on a small spot in the sample. To create a whole image, the focused light is scanned across the field of view and the sequential intensity readouts are combined to form an image. A 3D volume can be reconstructed by moving the sample up/down to capture images in different planes.

LSCM and WFM both can produce images with high lateral resolution. The resolution is the minimum distance between two points in which they can still be viewed as separate entities. The limit of the resolution of an optical system is imposed by the Rayleigh criterion,

$$r = 0.61 \frac{\lambda}{NA} \tag{1}$$

where λ is the wavelength of light and NA is the numerical aperture of the objectives. The diffraction limit r in WFM and LSCM considering visible light is about 200 nm.

While both WFM and LSCM have the potential to exhibit similar lateral resolutions, the confocal setup offers images with improved sharpness due to the elimination of out-of-focus emitted light (**Figure 1.3**). However, image acquisition in confocal microscopy is typically slower, as each point within the image must be scanned. When a large field of view is required, WFM may be a more suitable option compared to LSCM.

In conclusion, WFM affords swift image acquisition, but with a resultant blurry background, while LSCM offers improved optical sectioning and sharp images, but at the cost of slower imaging speed. Light-sheet fluorescence microscopy represents a compromise, affording both, fast image acquisition and optical sectioning, which is further explored in a subsequent section.

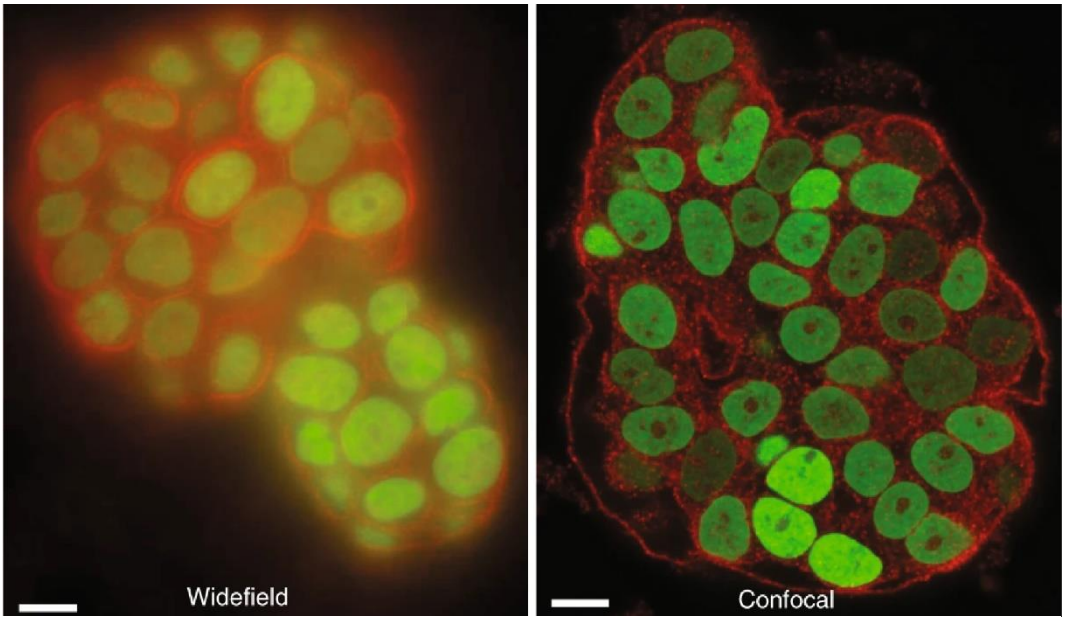

Figure 1.3. Images captured with widefield and confocal microscopy. (a) *The widefield image looks blurry because of out-of-focus light still reaches the camera.* ***(b)*** *The confocal image is sharper because the out-of-focus light coming from other planes are blocked. The scale bars are 10 µm. Reproduced from* [104] *with permission from Springer Nature.*

1.2.3 Light-sheet microscopy

1.2.3.1 Principles of light-sheet microscopy

Light-sheet microscopy (LSM) combines the large field of view acquisition of widefield microscopy and the optical sectioning capability of confocal microscopy. This technique uses an excitation optical path and a detection optical path that are separated from each other, as depicted in **Figure 1.4**. The excitation path generates a thin sheet of light that illuminates a specific plane in the sample. The detection path, aligned perpendicularly to the excitation light-sheet, captures a direct image of the whole illuminated plane, providing a sharp image due to the optical sectioning capability.

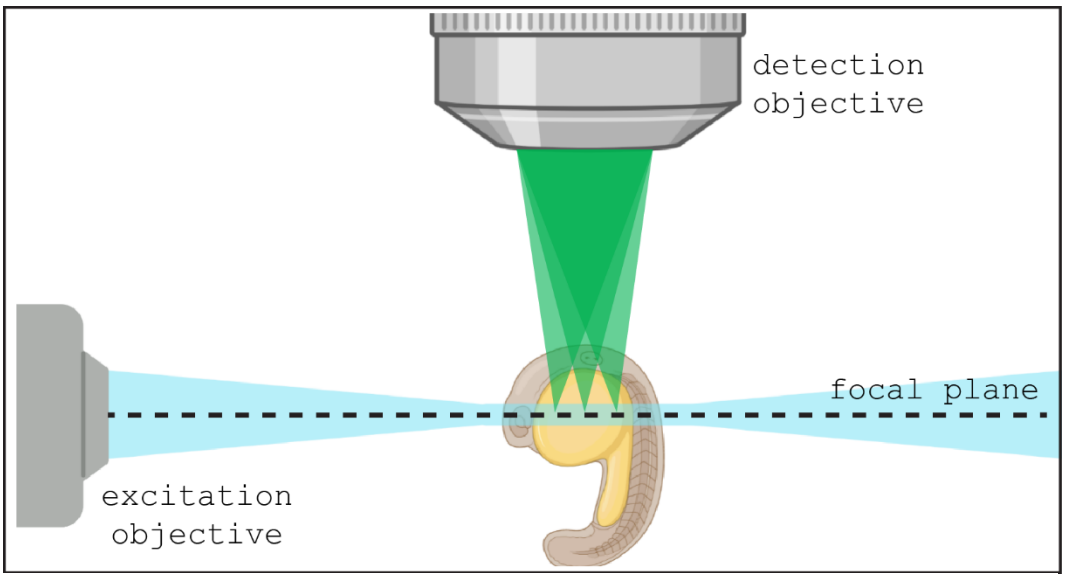

***Figure 1.4. Light-sheet configuration**. In light-sheet microscopy, the excitation and detection objectives are perpendicular to each other. The excitation objective excites a large area in the focal plane of the detection objective.*

Light-sheet microscopy is an ideal choice for imaging living samples, because, aside from optical sectioning and having a wide field of view, there is a great reduction in the total amount of light delivered to the sample compared to the confocal setup and there is minimal photobleaching and phototoxicity [17]–[19], at least along the optical axis of the detection objective. This makes LSM a valuable tool for long-term development studies such as organogenesis [20], cell migration [21], [22] and cardiac development [23]–[26], with the most widely used model organisms being the zebrafish [27]–[31] and drosophila melanogaster [32], [33]. **Figure 1.5** shows the region of the sample that is exposed to photodamage in light-sheet, confocal, and widefield microscopy. For light-sheet microscopy, the plane of illumination is localized to the focal plane of detection path. While for confocal and widefield fluorescence microscopy, the entire axis along the detection objective is subjected to photodamage even though only a small section is in focus. The light exposure outside the focal plane contribute to background signal, fluorophore bleaching, and phototoxicity.

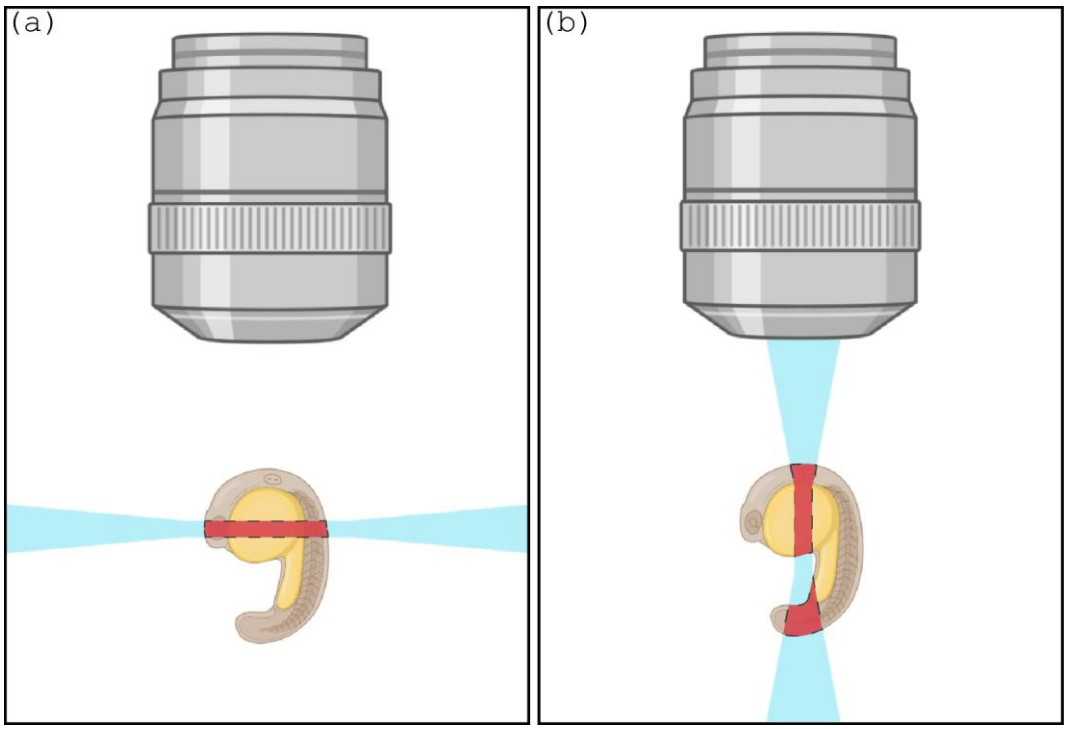

Figure 1.5. Photodamage comparison. (a) *In light-sheet microscopy the plane of excitation is the same as the focus of the detection objective.* ***(b)*** *In both confocal and widefield microscopy, the excitation light imparts photodamage along the whole optical axis of the detection objective although only a single plane is in focus.*

The dimensions of the excitation sheet of light are an important consideration in light-sheet microscopy. **Figure 1.6** shows the different parameters that describe the light-sheet.

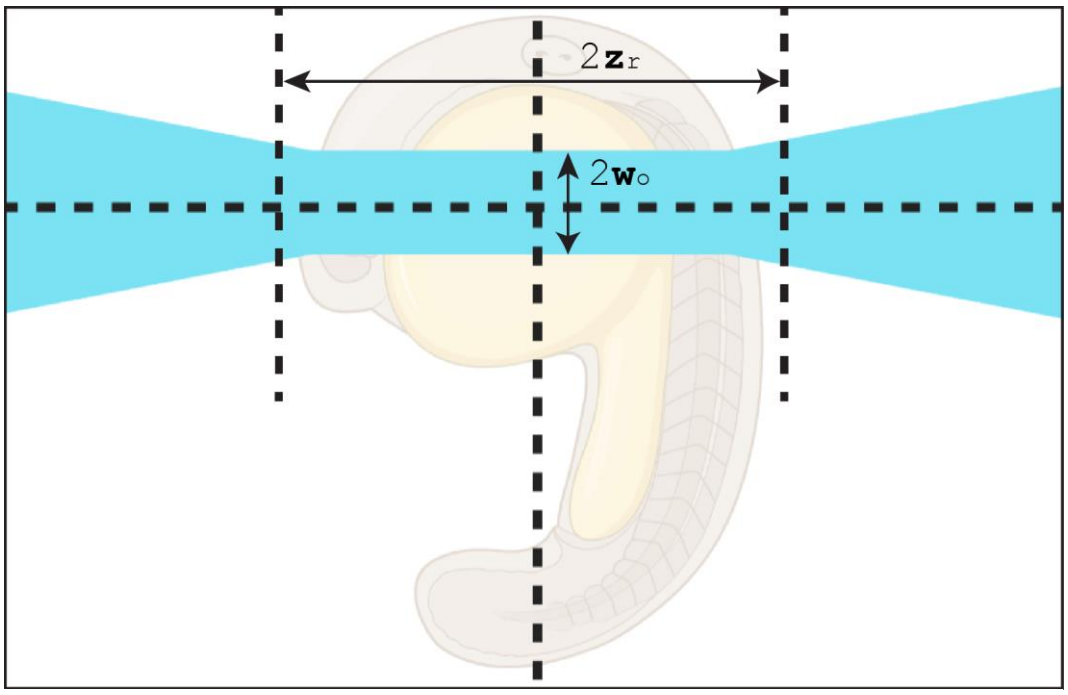

Figure 1.6. Light-sheet parameters. *A focused beam, such as a light-sheet, has a defined waist (ω_o) and length (z_r). The beam waist and beam length are inverse-squared proportional to each other.*

The thickness of the light-sheet is determined by the beam waist ($\boldsymbol{\omega_o}$) of the excitation beam while the length of the light-sheet is determined by the so-called Rayleigh length ($\boldsymbol{z_r}$). The optimum configuration for the light-sheet is to minimize the beam waist $\boldsymbol{\omega_o}$ for better optical sectioning, and to maximize the Rayleigh length $\boldsymbol{z_r}$ for a wider field of view. However, these two parameters are related by

$$\boldsymbol{z_r} = \frac{\pi \boldsymbol{\omega_o}^{\,2} n}{\lambda} \qquad (2)$$

where n is the index of refraction of the medium and λ is the wavelength of light. Reducing the beam waist results in a square reduction of the extent of the light-sheet, leading to a trade-off between creating a thin sheet with better optical sectioning and a long sheet with a wider field of view. The balance between thickness and field of view depends on the specific biological application. Recent advancements in light-sheet microscopy have aimed to address the challenge of balancing these conflicting features. The next section of this chapter explores these recent developments in light-sheet microscopy.

1.2.3.2 Advancements in light-sheet microscopy

1.2.3.2.1 Digitally scanned light-sheets

The light-sheet illumination was traditionally formed by using a cylindrical lens which is a type of lens with a different curvature between its two axes perpendicular to the optical axis. When there is no curvature along one of its axes, a cylindrical lens shapes a beam in only one dimension and focuses the beam into a line instead of a point.

A major advancement in light-sheet microscopy was made by Keller *et al*. [34] in 2008 when they introduced digital scanned light-sheet microscopy (DSLM). This method replaces the use of cylindrical lenses with a focused beam and scans the beam to produce a virtual light-sheet as shown in **Figure 1.7**. The virtual light-sheet is generated by rapidly scanning the beam in synchrony with the readouts from the camera.

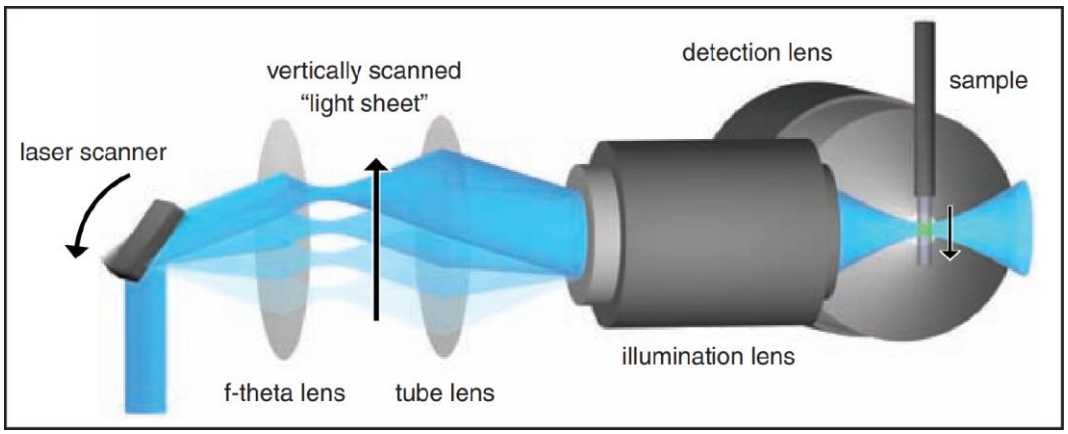

Figure 1.7. Virtual light-sheet by laser scanning. *A static light-sheet can be created using a cylindrical lens that focuses only on a single axis, while a virtual light-sheet can be created by scanning a focused beam. Reproduced from [35]. Reprinted with permission from AAAS.*

There are several advantages of using a scanned light-sheet. First, the light-sheet is more homogenous since each line is illuminated with the same intensity. Also, the extent of the light-sheet can be adjusted easily by changing the amplitude of the scanning.

1.2.3.2.2 Bessel beam light-sheet

The development of DSLM led to the exploration of other exotic light-sheet formations, including the use of non-diffracting Bessel beams [35]–[37].

Bessel beams are characterized as non-diffracting solutions to the scalar-wave equation in free space, meaning that their transverse intensity distribution does not spread as they propagate. Such beams with this property are so called propagation invariant. This makes Bessel beam light-sheets attractive alternative to Gaussian beam light-sheets, because their thickness remain constant over a longer propagation lengths.

Figure 1.8 shows the intensity profile of a Bessel beam, characterized by a central lobe surrounded by concentric rings. While ideal Bessel beams cannot be generated, an approximation has been experimentally achieved through annular illumination of the back pupil of an objective. A thinner annulus provides a better approximation of a Bessel beam but also obstructs more power from the laser source. Despite this, experimental Bessel light-sheets still provide a thinner light-sheet compared to Gaussian light-sheets of the same length [36].

One challenge with Bessel beam light-sheets is that they do not provide perfect optical sectioning, resulting in some out-of-focus blurring. The rings of the Bessel beam prevent the generation of perfect optical sectioning. The Bessel light-sheet does not have a perfect zero intensity above and below the central band. Additionally, more energy goes into the rings of the beam for longer beams, increasing the intensity of the side bands and further contributing to out-of-focus blurring. To address these issues, Betzig *et al*. [38] developed a technique based on the superposition of Bessel beams, which balances the thickness of the light-sheet and the out-of-focus blur of the ring. This new mode is known as lattice light-sheet.

1.2.3.2.3 Lattice light-sheet

The presence of the rings surrounding the central core of the Bessel beam hinders the achievement of perfect optical sectioning. In 2015, Betzig *et al*. [38] addressed this challenge by superimposing multiple Bessel beams to create perfect zero intensities above and below the

central light-sheet. This results in a 2D lattice-like pattern that is referred to as a lattice light-sheet.

The structure of the lattice light-sheet illumination is shown in **Figure 1.8**. There are two major variants: the hexagonal lattice and the square lattice. The first column shows the intensities of the Gaussian, Bessel, square lattice, and hexagonal lattice, respectively, in the pupil plane. The two variants of lattice light-sheet illumination, hexagonal and square lattices, present different features in their central band and side bands. Similar to the Bessel beam, the central sheet of both lattice light-sheets are propagation invariant. However, the side band intensity of the lattice light-sheets increases with propagation length, as is the case with the Bessel beam.

The hexagonal lattice exhibits a thinner central band but with multiple side bands, while the square lattice has a thicker central band with fewer side bands. The square lattice is more widely adopted in the field due to its fewer side bands and better optical sectioning performance.

Lastly, the usage of multiple Bessel beams to generate the lattice light-sheet is much less phototoxic than a single beam, as the same total power delivered is spread across a larger area [39], [40].

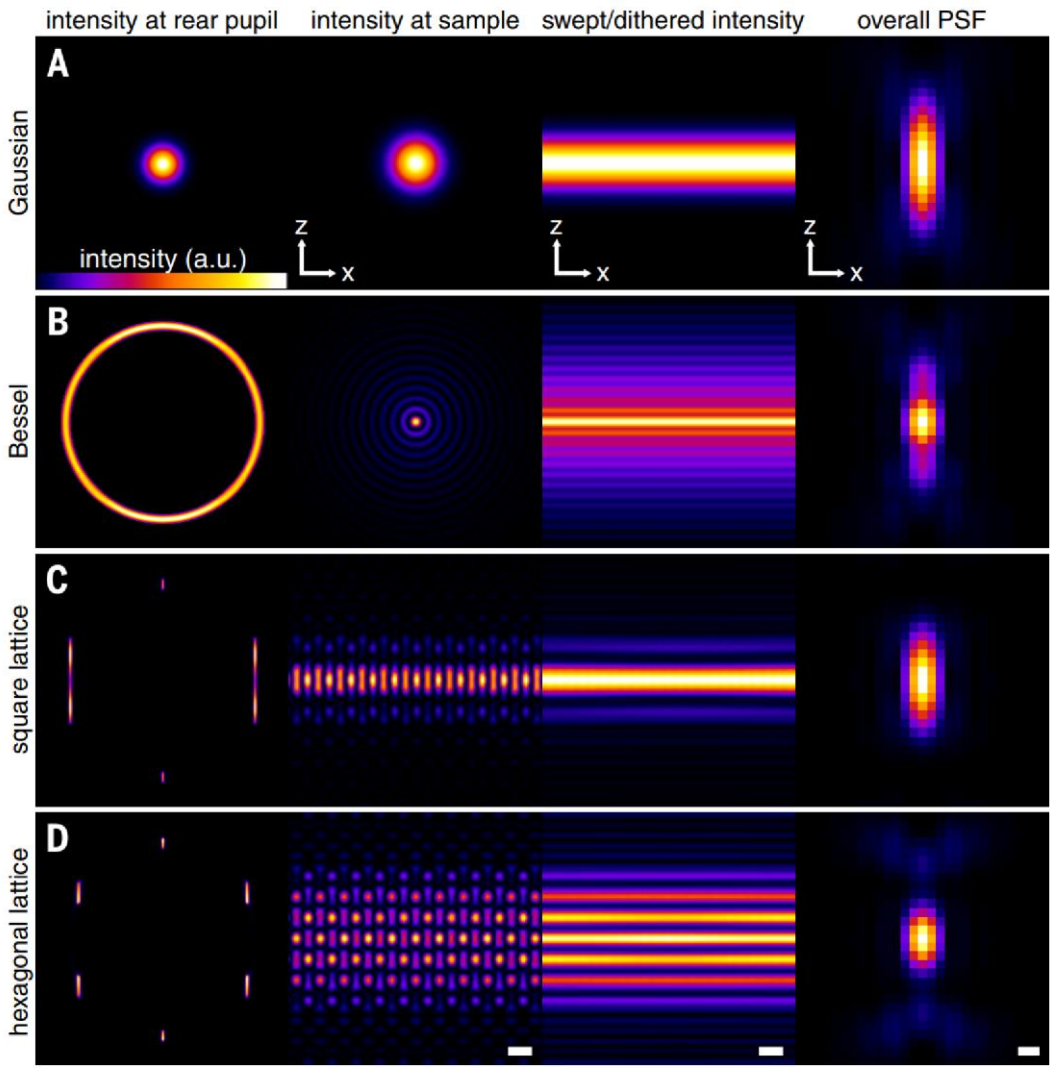

***Figure 1.8. Lattice light-sheet illuminations**. **(a)** Gaussian light-sheet. **(b)** Bessel light-sheet. **(c)** square lattice light-sheet. **(d)** Hexagonal lattice light-sheet. The first column shows the intensities of the Gaussian, Bessel, square lattice and hexagonal lattice, respectively in the pupil plane while the second column shows the intensities in sample plane. The next column shows the light-sheet generated when the beams are scanned. The rightmost column shows the PSF of the different light-sheets, while factoring in the beam forming (detection-PSF) in the detection path between the sample and the camera. Reproduced from [38] with permission from AAAS. The scalebars from left to right are 1.0 µm, 1.0 µm and 200 nm, respectively.*

1.3 An introduction to the microscope that I am building

The implementation of a lattice light-sheet microscope offers various benefits for imaging biomimetic cultures. These benefits include a high axial resolution for optical sectioning, minimal photobleaching and photodamage, and the illumination of the entire field of view for fast acquisitions. Consequently, the Betzig group developed the Multimodal Optical Scope with Adaptive Imaging Correction (MOSAIC), a microscope that integrates lattice light-sheet imaging with other microscopy modes into a single instrument. The instrument allows for

dynamic switching between modes without the need to move the sample. Furthermore, the MOSAIC is equipped with adaptive optics to correct for both system and sample-induced optical aberrations.

1.4 Lattice light-sheet imaging of 3D cultures

Previous studies have demonstrated the potential of LLS for imaging three-dimensional (3D) cultures and providing detailed structural and functional information. Chen *et al.* [41], explored the application of the lattice light-sheet microscopy system for imaging a 3D culture of hippocampal neurons. They showed capability of the LLS to capture live spheroids, unveiling dynamic cellular processes and heterogeneity within the 3D culture models. They highlighted advantages of LLS, such as reduced phototoxicity and improved signal-to-noise ratio compared to traditional imaging techniques.

In another notable work, Schöneberg *et al.* [42], focused on handling and analyzing large datasets obtained from lattice light-sheet microscopy of 3D intestinal epithelial organoids. Here, they presented a computational pipeline to manage the substantial amount of imaging data generated by LLSM and extract meaningful information. They addressed challenges associated with data storage, processing, and visualization, utilizing various computational tools and algorithms. This study emphasized the significance of efficient data handling and analysis techniques to fully leverage the potential of LLS for imaging 3D cultures.

However, it is important to note that these studies utilized the earlier standalone version of the lattice light-sheet instrument. The newer version of LLS, integrated into the MOSAIC microscope, offers several notable advancements, rendering it an appealing choice for imaging 3D cultures.

One key advantage of the newer lattice light-sheet version integrated into the MOSAIC microscope is its enhanced practicality for imaging 3D cultures. The sample chamber and sample holder have undergone a redesign to accommodate larger and more complex 3D culture models. This expanded sample space facilitates the imaging of larger specimens, such as biomimetic cultures.

Additionally, the newer lattice light-sheet version incorporates a new optical element that enables faster imaging by facilitating simultaneous excitation of multiple fluorophores, up to 7 channels. Furthermore, the mask design has been improved, allowing for quick adjustment of the lattice light-sheet parameters. Unfortunately, I cannot discuss these new optical designs in this thesis because of our confidentiality agreement with Janelia Research Campus.

In summary, the introduction of the newer version of lattice light-sheet microscopy integrated into the MOSAIC microscope brings several advantages for imaging 3D cultures. Alongside the ability to combine different imaging modes, the larger sample chamber and sample holder enhance imaging capabilities for more complex and larger specimens. Moreover, the incorporation of new optical elements enables faster imaging and greater practicality in adjusting the light-sheet parameters. These advancements have motivated our choice to build and utilize this new version of LLSM for imaging living 3D cultures in our research.

The focus of this thesis is the construction of the LLS component of the MOSAIC microscope, the optimization process, and its application for imaging 3D cultures. The methodology and goals of the research are described next.

1.5 Goals and structure of the thesis

1.5.1 Goals of the thesis

My work aimed to achieve the four following objectives:

- **Construction of the lattice light-sheet MOSAIC microscope at DTU:** The objective of my work was to build the MOSAIC microscope, which is equipped with lattice light-sheet imaging capabilities, at the Technical University of Denmark (DTU). The process of building the instrument was documented, and the challenges encountered were identified. In this thesis, I suggest solutions to some of these challenges and provide a report on the rest.
- **Optimization of the lattice light-sheet path:** The objective was to optimize the lattice light-sheet path for imaging and report on the results of these optimizations. This

information can serve as a reference point for other researchers that are building similar instruments.

- **Demonstration of the imaging of 3D biomimetic organotypic systems:** The objective was to demonstrate the imaging capabilities of the MOSAIC lattice light-sheet microscope by imaging 3D biomimetic organotypic systems. This exhibits the potential applications of the instrument in complex 3D samples.
- **Production of a guide for imaging and mounting of large 3D cultures:** The objective was to provide a guide for imaging and mounting large 3D organotypic cultures into the MOSAIC, which can serve as a manual for the building and calibration of the instrument.
- **Characterization of the imaging performance of the LLS:** The objective was to characterize the resolving power of the instrument by measuring and calculating its point spread function. Additionally, an equation that gives the apparent increase in the z-resolution (relative to the sample coordinates) is presented. This equation can be useful in tuning the angle of acquisition of the LLS for a desired resolution trade-off between the z and x-resolutions in the sample coordinates.
- **Demonstration of particle tracking with the image captured with the LLS:** The primary goal is not focused on uncovering groundbreaking biological discoveries. Instead, the main emphasis lies in showcasing the wide array of quantitative data that can be obtained by applying particle tracking to the images captured using the LLS. The intention is to inspire and encourage further exploration and utilization of the LLS.

1.5.2 Structure of the thesis

With the above goals in mind, the next chapters of the thesis are structured as follows:

Chapter 2 gives a more in-depth review of fundamental concepts in fluorescence microscopy, lattice light-sheet microscopy, and adaptive optics. This chapter also delves deeper into the recent advancements in these fields.

Chapter 3 presents the steps taken to build the lattice light-sheet (LLS) optical path of the MOSAIC microscope. Moving forward, I will refer to lattice light-sheet optical path of the MOSAIC as the LLS. The chapter provides a comprehensive description of the LLS path, including its components, assembly, and installation. The results of the chapter outline the

difficulties encountered during the building process, offering suggestions for refinements and recommendations for future builders of the MOSAIC.

Chapter 4 focuses on the optimization of LLS imaging in the MOSAIC microscope. The chapter discusses various optimization techniques for LLS imaging, such as using a spatial light modulator (SLM) and deformable mirror (DM) to correct system aberrations.

Chapter 5 documents a practical application of the LLS for imaging 3D biomimetic cultures. The chapter provides a detailed protocol for imaging and mounting large 3D samples and discusses the results of these imaging experiments. The chapter demonstrates the capabilities of the LLS in imaging complex 3D structures. Moreover, it provides insights such as which imaging settings I used and how a stack is acquired by the instrument.

Chapter 6 provides a characterization of the imaging performance of the LLS. This chapter reports the theoretical and the measured PSF of the LLS and offers a comparison with the PSF in a spinning disk microscope. Because of the configuration of the objectives in the LLS, the PSF is rotated relative to the sample coordinates. Thus, there is an increase in the z-resolution in the sample coordinates. The chapter presents an equation for this increase in the z-resolution given the angle of the detection objective (relative to the coverslip) and the PSF of the LLS. Furthermore, the chapter demonstrates the wealth of quantitative data that can be extracted through image-analysis methods like particle tracking.

Although each chapter has its own discussion section, **Chapter 7** gives an overall discussion of the whole thesis regarding the construction, optimization, and application of the MOSAIC microscope. Finally, **Chapter 8**, concludes the thesis with a summary of my findings and explicit recommendations for further refinement of the LLS instrument.

Chapter 2. Theory

2.1 Fluorescence microscopy

2.1.1 Fundamental concepts in fluorescence microscopy

Fluorescence is a phenomenon where light is emitted within a few nanoseconds after absorption of a shorter wavelength light [43]. The difference between the wavelength of the absorbed and emitted light, known as the Stokes shift, is a crucial feature that makes fluorescence a valuable tool in microscopy [44]. By selectively removing the excitation light and allowing the emitted fluorescence to pass, it is feasible to isolate only fluorescence-labeled structures for visualization. One effective method to gain insight into the intricacies of the excitation and emission mechanism is to illustrate the process using a diagram that was originally proposed by Alexander Jablonski in the 1930s shown in **Figure 2.1**.

The diagram depicts the singlet states, $S_{n,}$ on the left-hand side. At the righthand side of the diagram are the triplet states, T_n. Typically, electrons exist in pairs with opposite spins within a single orbital. This pairing causes their magnetic moments to cancel out, creating what is known as a singlet state [43], [44]. A pair of non-bonding electrons can also exist in two distinct orbitals with their spins aligned in parallel. If an atom or molecule possesses such an arrangement of electrons, its overall magnetic moment can be oriented parallel, perpendicular, or antiparallel to a magnetic field. Since these three orientations correspond to slightly different energy levels, the atom or molecule can exist in all three forms, and it is known as a triplet state [43], [44]. The ground state, S_0, denotes the molecule's energy when it is not stimulated by light. On the other hand, the excited singlet states, S_1 and S_2, correspond to situations where an outer electron is promoted to a different orbital. S_2 has higher energy than S_1, and S_1 has more energy than the ground state, S_0.

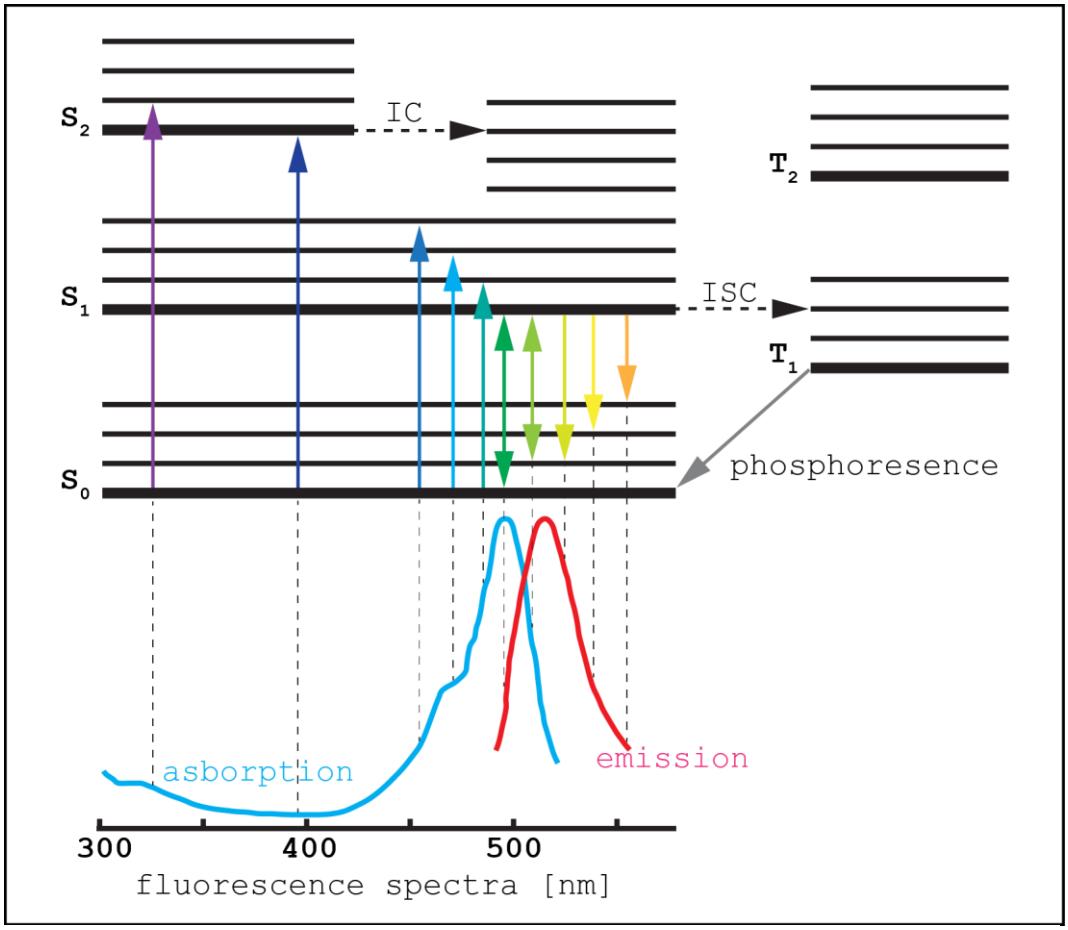

Figure 2.1. Jablonski diagram. *The Jablonski diagram is a graphical representation of the electronic energy levels and transitions in a molecule. The thick lines are different electronic levels, while the thinner lines are vibrational levels. The different electronic transitions are depicted by arrows. The transitions from the singlet states, S_n, to the ground state results in fluorescence while the transition from the triplet state, T_n, results in phosphorescence. IC is internal conversion while ISC is intersystem crossing.*

There are numerous vibrational levels that can be associated with each electronic state [45] as denoted by the thinner lines in **Figure 2.1**. Electrons in the ground singlet electronic state can absorb light and transition to different vibrational levels in the singlet excited vibrational states. However, it is improbable for them to transition from the ground singlet electronic state to the triplet electronic state since their electron spin remains parallel to that of the ground state. Nevertheless, electrons can undergo "intersystem crossing" (ISC in **Figure 2.1**), which is the process by which they spontaneously switch between singlet and triplet states [43], [44].

Fluorescence is one rapid radiative mechanism in which excited electrons release energy by transitioning from the excited singlet states to the ground state, emitting light in the process. While some molecules in the triplet state can return to the ground state without emitting light,

in many cases, they undergo a light-emitting process called phosphorescence. However, this process can take longer to occur as it involves an improbable transition where the electron reverses its spin. Fluorescence typically occurs over 10^{-9} seconds while phosphorescence can occur over 10^{-3} to 10^{0} s [43], [44].

2.1.2 Excitation and emission spectra

The energy that a photon can transfer to the fluorescent molecule is inversely related to the photon's wavelength ($E = hc/\lambda$, where h is Plank's constant and c and λ are the speed and wavelength of light in vacuum, respectively). Fluorescence requires a minimum amount of energy that can cause the transition of an electron into a higher electronic excited state, that is S_0 to S_1. In cases where the energy of the absorbed photon exceeds the amount required for the transition from the ground state to the lowest energy level of S_1, the molecule may undergo further changes in its vibration, rotation, and electronic orbital, potentially reaching an even higher electronic state such as S2. Thus, there is a range of wavelengths that can excite a molecule.

In addition to single-photon excitation, it is also possible for a molecule to be excited by the combined energy of multiple photons. For instance, if two photons with half the energy required to reach the excited state, simultaneously interact with a molecule, their energies can combine to provide for two-photon excitation. However, since the absorption process is very short, high light intensities are required for the low-energy (infrared) photons to coincide in the same location at almost the same time.

To determine the excitation spectrum of a fluorophore, the fluorescence yield can be measured by exposing a sample to varying wavelengths of incident light. The emitted fluorescent light at a different wavelength than that of the excitation light is then recorded. For certain molecules, there exists a limited number of vibrational or rotational states between the highest energy level of S_1 and the lowest level of S_2. Consequently, the absorption spectrum for many fluorophores exhibits a dip between the two peaks associated with exciting to an S_1 level (absorption of longer wavelengths) and to an S_2 level (absorption of shorter wavelengths) as shown in **Figure 2.1**.

The molar extinction coefficient is a measure of the probability that a fluorophore will absorb a photon, expressed in units of $M^{-1}cm^{-1}$. Enhanced green fluorescent protein (EGFP), which

has an excitation maximum of 488 nm, has a molar extinction coefficient of around 60,000, five times higher than that of wild type GFP with an excitation maximum of 470 nm [46]. Fluorophores with high molar extinction coefficients are particularly useful in situations where light intensity needs to be kept to a minimum, such as in the imaging of living tissues or when there are very few fluorophore molecules present.

For efficient fluorophores, the most favorable way to return to the ground state is to emit a photon with enough energy to bridge the difference between the lowest vibrational state of S_1 and any of the vibrational or rotational states of S_0 [45]. The range of wavelengths for the emitted photon of a fluorophore represents its emission spectrum (**Figure 2.1**). Due to the non-radiative transition back to the lowest energy level of S_1, the wavelength of the emitted light is independent of the specific wavelength of the incident light. As a result, it is generally not possible to alter the emission spectrum by changing the color of the exciting light.

When a fluorophore emits light, it does so from the lowest energy level of the excited state, and this emitted photon typically has less energy than the photon that was absorbed. This difference in energy is due to the loss of energy through vibrational relaxation and internal conversion. This is the origin of the Stokes shift. During vibrational relaxation, the excess energy in the fluorophore is transferred to nearby molecules through direct interactions, with water being the most likely recipient in an aqueous environment. Meanwhile, internal conversion (IC in **Figure 2.1**) initially involves isoenergetic transitions between low vibrational states of one electronic state and high vibrational states of a lower electronic state. Although no energy is lost during this process, the excess energy is ultimately dissipated through vibrational relaxation [45].

Sometimes, when fluorophores are excited, a small percentage of them are in higher vibrational states of the ground state. When this happens, the photon can drop back in a bigger energy jump than what was required to reach S_1, which leads to the overlapping of the emission and excitation spectra in **Figure 2.1**. The fluorescence emission spectrum and the absorption spectrum show mirror symmetry because the final transition from the excited state to the ground state typically starts from the lowest vibrational state of S_1. The vibrational transitions occurring during fluorescence emission are the same as those occurring during excitation, and have the same probability in either direction. These transitions typically start from the '0' vibrational state and can move to either the same or higher vibrational states, such as 0, 1, 2,

or 3. For instance, the likelihood of a vibrational transition from S_0 level 0 to S_1 level 3 is similar to that from S_1 level 0 to S_0 level 3 [43]–[45]. This is why the emission peak is the same as the excitation peak but is only shifted.

Understanding the absorbance and emission spectrum of a fluorophore is crucial for determining the optimal filters to use and lasers to excite the dye, as well as for minimizing crosstalk between different fluorescence detection channels during imaging.

Currently, various probes are available that can be used to examine different physiological processes by accumulating in organelles such as mitochondria, endoplasmic reticulum, nucleus, or synaptic vesicles [47], [48]. Additionally, fluorescent sensors have been developed to take advantage of the sensitivity of a fluorophore's absorption and emission properties, to changes in the environment, such as binding to calcium ions [49], [50], hydrogen ions [51], or other molecules of interest. However, imaging multiple fluorophores in the same sample can result in overlapping excitation and emission spectra, leading to crosstalk between signals associated with different fluorophores. In chapter 4, I discuss the crosstalk observed in one of my imaging experiments.

2.1.3 Photobleaching

While a fluorophore can, in theory, undergo an infinite number of cycles between ground and excited states, practical conditions often impose a limit on the number of cycles. For organic fluorophores, the number of cycles is typically limited due to the occurrence of photobleaching, which is a term used to describe the permanent fading of the fluorescent signal. Good fluorophores are estimated to be able to undergo 10,000 - 40,000 cycles before permanent bleaching occurs [45].

There are various mechanisms by which bleaching occurs in fluorophores, and the underlying photochemistry for most fluorophores is not yet fully understood. However, it is evident that the triplet state, which is a long-lived state, provides more opportunities for an excited electron to interact with other molecules than the briefer singlet states [52], [53]. As a result, it is believed that most bleaching is associated with triplet states. Additionally, one crucial factor in bleaching is the interaction between a fluorophore in the triplet state and molecular oxygen.

The triplet state can transfer its energy to oxygen, thus exciting oxygen to its singlet excited state [45], [53]. Singlet oxygen, a type of reactive oxygen species (ROS), is a reactive molecule that can participate in numerous chemical reactions with organic molecules. This leads to covalent modifications of the fluorophore and disables its capacity to fluoresce. [53].

The occurrence of bleaching in fluorophores is a significant concern in various fluorescence-based imaging techniques used in research and diagnostics. While fluorescence microscopy and other imaging technologies have transformed biological research by enabling the visualization of molecular interactions and cellular processes in real-time, bleaching can limit the effectiveness and accuracy of these techniques. The mechanism of bleaching in fluorophores is a complex process that is not yet fully understood. This hinders the development of improved fluorophores with higher photostability. Therefore, ongoing research is focused on identifying the mechanisms underlying bleaching and developing strategies to mitigate or prevent it [53], [54]. Additionally, researchers are developing new fluorescent probes with better photostability to improve the performance of fluorescence-based imaging techniques.

Lastly, although photobleaching is generally seen as a disadvantage because it results in a decrease in the concentration of fluorescing molecules over time, there are cases where it can be advantageous. For instance, the technique of fluorescence recovery after photobleaching (FRAP) can be used to measure the rate of diffusion of a molecule [55], [56]. Additionally, acceptor photobleaching can be utilized in fluorescence resonance energy transfer (FRET) microscopy to establish reference points where there is no transfer of energy between fluorophores [55], [56]. By taking advantage of photobleaching in these ways, it is possible to extract valuable information about the properties and behavior of the fluorescing molecules, even as their concentration decreases over time.

2.1.4 Phototoxicity

At the molecular level, both photobleaching and phototoxicity are linked to the generation of ROS in the sample as a byproduct of fluorescence excitation [54], [57], [58]. These phenomena can pose a significant concern during prolonged imaging experiments such as long time-lapse sequences. Phototoxicity occurs when the photogenerated ROS causes damage to cellular components such as proteins and nucleic acids. In some cases, this can result in cell death,

although other effects may be more subtle, such as the photoinduction of intracellular calcium release or failure to divide [59]. While cell death is the most severe outcome, it is important to note that even the more subtle effects can have significant consequences for experimental outcomes.

To minimize damage to living samples, the ideal approach for fluorescence excitation is to only illuminate the specific focal plane being studied, as in light-sheet microscopy. However, many fluorescence microscopes, including widefield and confocal microscopes, use epi-illumination, where the excitation light is delivered along the detection axis and absorbed by the specimen, both, above and below the focal plane. As a result, phototoxicity is induced throughout the sample [60]–[62]. In 3D imaging, where z-stacks are recorded, every plane that is imaged exposes the entire sample to light, leading to an increase in phototoxicity proportional to the number of imaged planes. Phototoxicity can be significantly reduced by using light-sheet illumination, although the effectiveness of this method can vary depending on the technique used to generate the light-sheet.

2.2 The latest developments in lattice light-sheet microscopy

Light-sheet microscopy is typically implemented using a cylindrical lens to focus a Gaussian beam along one axis, resulting in a sheet of light at the specimen. Alternatively, a different method of light-sheet generation involves scanning a focused Gaussian beam to create a virtual light-sheet [28]. As discussed in **Chapter 1**, for Gaussian beams, there is an inherent tradeoff between the beam waist and the length over which the beam is narrow (confocal parameter).

In 2015, a new technique, called lattice light-sheet microscopy, was developed, which involves the use of carefully crafted coherent superpositions of Bessel beams [38]. LLSM has gained popularity for its ability to provide high-resolution and high-speed imaging with gentle illumination. However, certain critical optical parameters of the lattice, such as light-sheet thickness and propagation length, have not been independently examined. Recently, two studies [63], [64] investigated the properties of the square lattice compared to Gaussian beams, using both simulations and experimental measurements, and suggested that the square lattice does not offer significant performance improvement over Gaussian light-sheets in terms of confocal parameter and thickness. They even claim that for a given light-sheet confocal

parameter, Gaussian beams provide similar axial resolution, but with reduced image blur, and better optical sectioning. Furthermore, they showed that, despite being referred to as a propagation-invariant beam, the square lattice behaves like a divergent beam. However, they were unable to provide an explanation for this. Interestingly, they showed that for all the square lattice light-sheet dimensions listed in the original manuscript [38], a Gaussian light-sheet could be generated with a similar thickness, length, and divergence to the main lobe of the lattice.

Recently, Legant *et al.* [65], one of the authors of the original LLS-article, responded to the findings by demonstrating how different optical lattice illumination patterns can be adjusted to prioritize either axial resolution or optical sectioning. By adjusting both ΔNA and the central NA, it is possible to generate Gaussian-like beams with lower axial resolution and better axial confinement (fewer side lobes), or more lattice-like beams with higher axial resolution and uniformity, but lower confinement. Additionally, the square lattice has an extra parameter that can be adjusted to generate light-sheets with different properties while maintaining the same propagation length. This parameter is the position of the focused line in the back pupil. The authors report that the most uniform beam is achieved by selecting a beam spacing (**Figure 2.2**) that allows the two side lines to inscribe the inner annulus. The optimization of these extra parameters were not mentioned in the original LLS-article [38]. Overall, they suggested that lattice patterns with a ΔNA of 0.1 provide a middle-ground choice between increasing axial resolution and beam uniformity, while not overly sacrificing beam confinement.

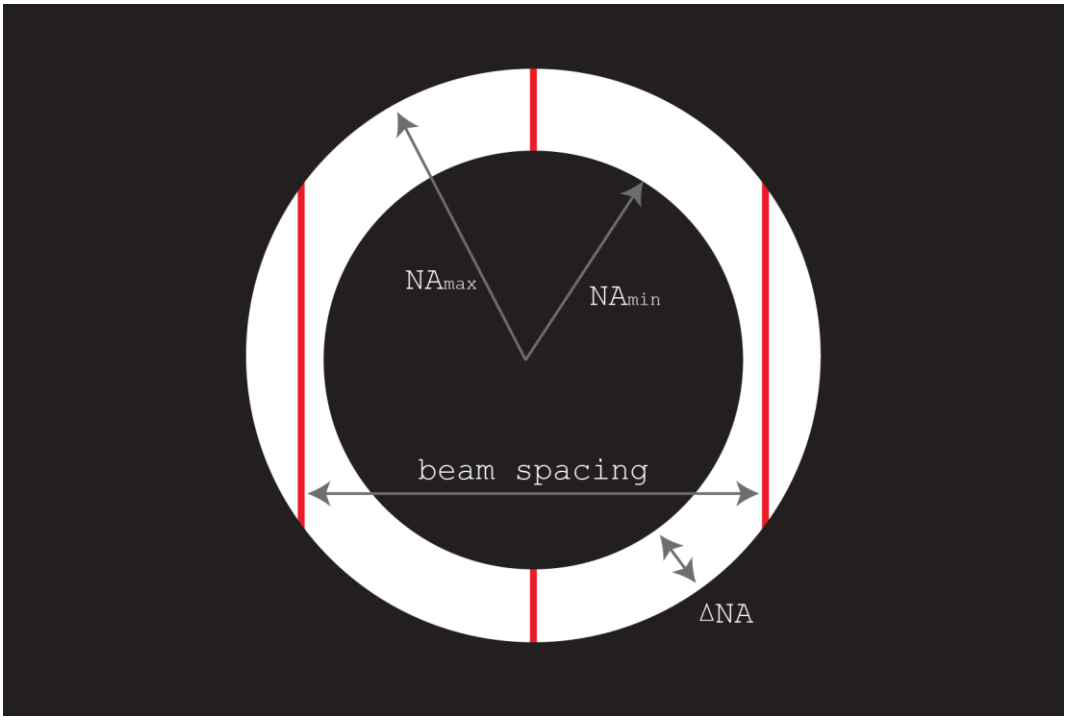

***Figure 2.2 Adjustable beam spacing parameter**. An annular mask is placed in the back aperture to generate the lattice patterns. The red lines are the 'beams' in the pupil plane. The distance between the left and right beam is defined as the adjustable beam spacing parameter introduced by Legant et al.*

However, the optimal pattern to use in lattice light-sheet microscopy will ultimately depend on the specific sample being observed, and the choice of which parameters to optimize will be dictated by the experimental conditions. The ability to adjust between different patterns that cover a range of features is a key advantage of lattice light-sheet microscopy. The ongoing discussions surrounding these considerations serve as evidence of the inherent complexity of lattice light-sheet microscopy.

2.3 Adaptive optics

The imaging performance of a microscope can be influenced by the optical properties of the sample. When imaging thick 3D biomimetic samples, spatial variations in the refractive index of the sample can introduce optical aberrations that reduce image quality, particularly when imaging deep into the sample. Consequently, this limits the amount of specimen that can be observed by the microscope, often restricting the depth to a few cell-layers near the surface. Moreover, aberrations have the potential to cause spreading of the focus, both laterally and axially, resulting in a decrease in focal intensity. The distortion of the focal spot can cause

reduced resolution and blurred images between adjacent planes along the optical axis, while the reduced intensity can lead to a loss of image contrast.

Wavefront aberrations are usually described mathematically by the infinite series of Zernike polynomial, written as Z_n^m, where *m* and *n* are integers that denote the order of the polynomial. The polynomials are orthogonal in the unit circle, meaning that they are mathematically independent of each other. The first 15 Zernike polynomials are shown in **Figure 2.3** while their effect on the point spread function is shown in **Figure 2.4**.

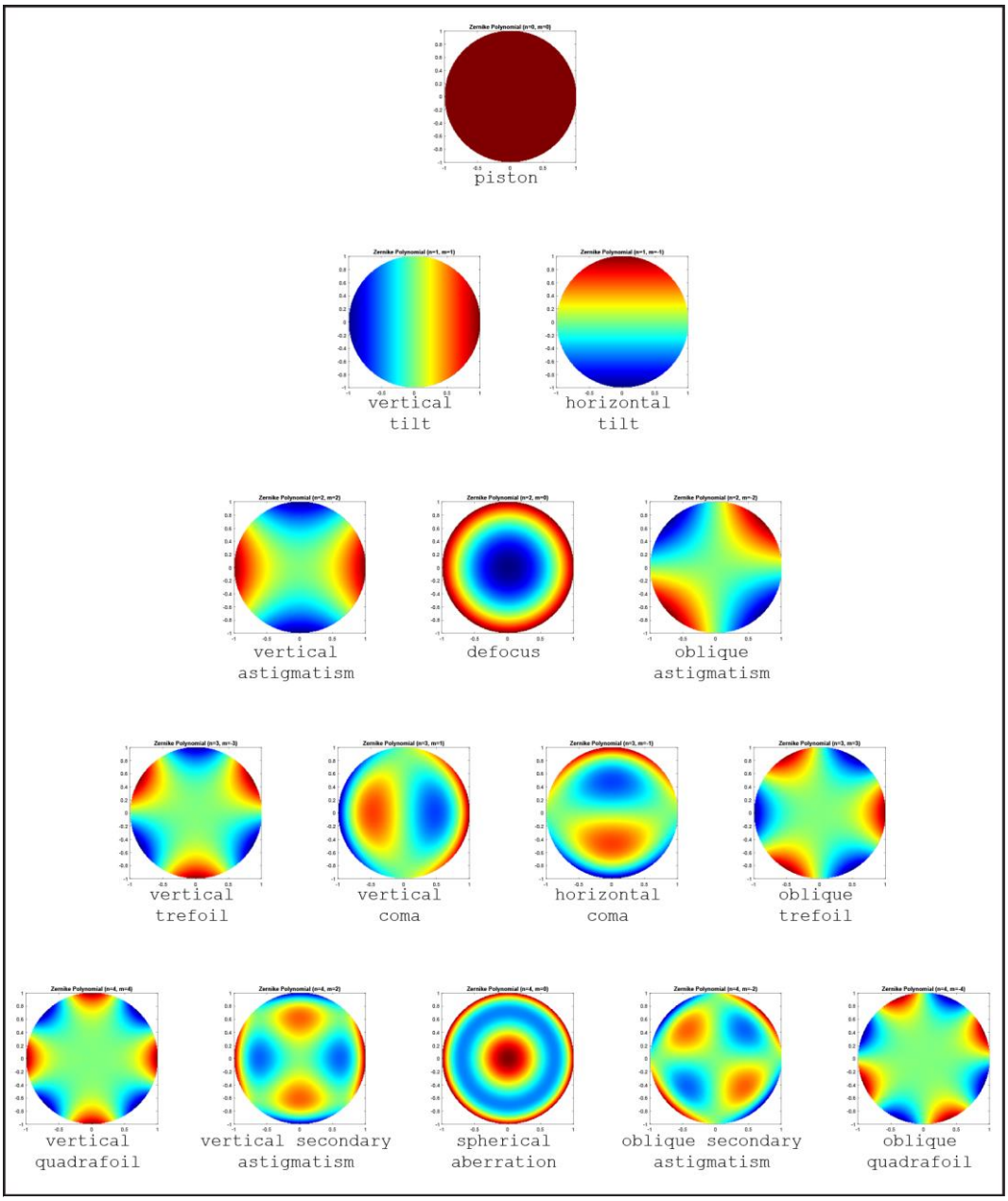

Figure 2.3. First 15 Zernike Polynomials*. Zernike polynomials over the unit circle represent known wavefront aberrations.*

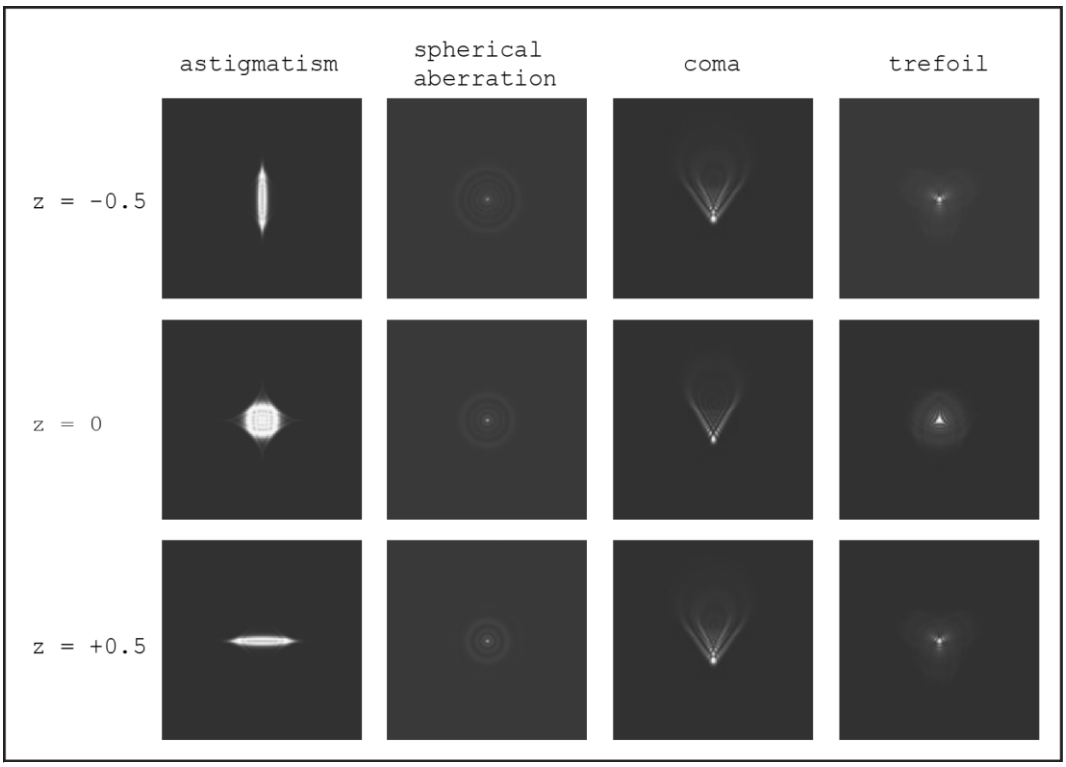

Figure 2.4. Effect of aberrations to the point spread function. *The Zernike modes have characteristic effect on the PSF. Here z is the position from the focal plane in microns. Reproduce from* [105] *with permission from Elsevier.*

Adaptive optics (AO) refers to a collection of techniques that can adaptively correct aberrations in an optical system. Originally designed to mitigate wavefront distortions arising from the earth's atmosphere in telescopes, adaptive optics is a concept that relies on identifying the aberration, whether it is sample-induced or inherent to the optical system. AO employes a wavefront modulator to introduce the negative of the distortion and minimize the overall aberration [66]. Two varieties of adaptive optic techniques exist: sensor-based adaptive optics involves direct measurement of the aberrated wavefront, while the other approach, known as sensor-less adaptive optics, does not directly measure the wavefront but instead relies on image metrics. These two varieties are illustrated in **Figure 2.5**.

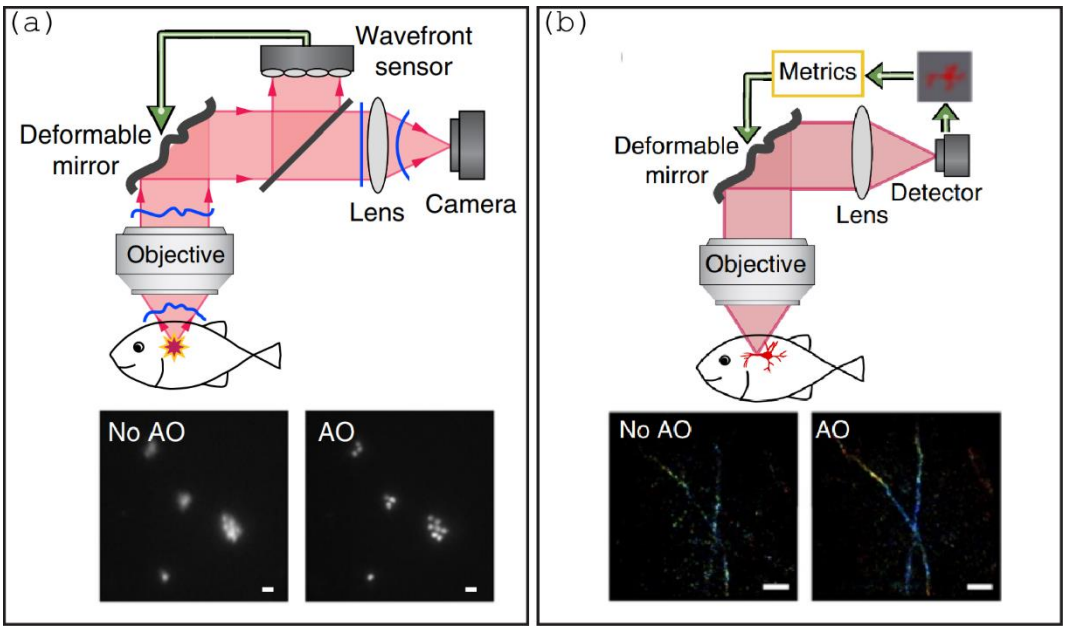

Figure 2.5. Adaptive optics modalities. (a) *Sensor-based AO systems use wavefront sensors to measure the aberrations present in the optical system. The sensor measures the phase distortions in the wavefront and sends this information to a control system, which then adjusts the DM or SLM to correct the wavefront distortions.* ***(b)*** *Sensor-less AO systems, on the other hand, do not use wavefront sensors to measure the aberrations. Instead, they rely on iterative algorithms to control the DM or SLM to minimize the wavefront error. In these approaches, the DM or SLM is adjusted to optimize an image quality related parameter. The scale bars are 2 µm (a) and 10 µm (b). Edited from* [67] *with permission from AAAS.*

2.3.1 Sensor-based adaptive optics

There have been numerous developments in direct wavefront sensing techniques for adaptive optics, with the Shack-Hartmann (SH) wavefront sensor and interferometric sensors [71-72] being the most prominent. These techniques require a point-like reference source, called a "guide star" (a term derived from its use in astronomy), to produce a wavefront that is well-defined.

To perform wavefront sensing using a SH wavefront sensor, the wavefront is segmented by an array of lenses and the light rays within each segment are focused onto a camera. The displacements of individual light foci are then used to calculate the local slope of each wavefront segment, which allows for the reconstruction of the wavefront (**Figure 2.6**). However, this method only works effectively when there are enough unscattered photons from the guide star reaching the sensor, as scattering can result in a loss of phase information, leading to diffusive foci on the wavefront sensor [67].

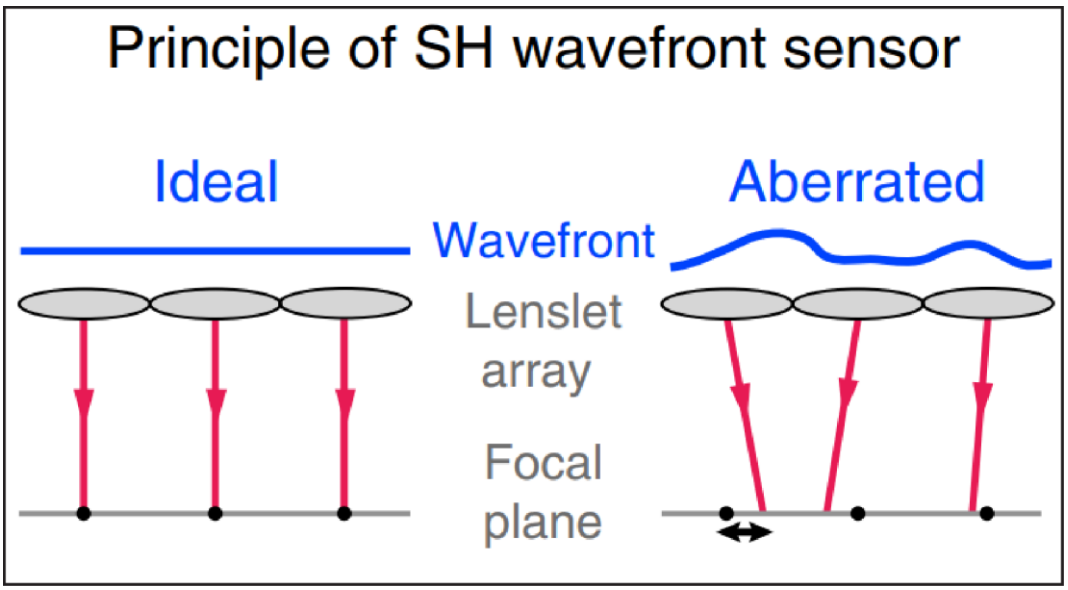

Figure 2.6. Shack-Hartmann wavefront sensor. *The Shack-Hartmann sensor consists of a lenslet array, where each lenslet forms an image of the wavefront onto a detector. The wavefront coming through each lenslet is focused onto a single spot on a detector, creating a unique pattern for each lenslet. The deviations of the spot pattern from a perfect grid are analyzed to determine the shape of the wavefront. Reproduced from* [67] *with permissions from AAAS.*

The initial use of adaptive optics in imaging biological specimens involved the direct sensing of wavefronts to achieve high-resolution imaging of the retina [68]. The aberration of human eyes was measured using light reflected from the retina as a guide star. In another study, Espinosa *et al*. [69], used two-photon excitation to produce a guide star and correct for sample-induced aberrations in roundworms (Caenorhabditis elegans) and mouse brain. Azucena *et al*. [70], [71] used an SH wavefront sensor in a widefield microscope to measure the aberration in Drosophila embryos by injecting them with fiducial fluorescent beads to serve as guide stars. Similarly, Jorand *et al*. [72] incorporated fiducial beads into 3D multicellular tumor spheroids and used them to correct the aberrations induced by the spheroids in a light-sheet microscope.

These studies utilized a closed-loop system between a wavefront sensor and a deformable mirror to minimize the detected wavefront error. In addition to deformable mirrors, spatial light modulators (SLMs) can also be used as wavefront modulators. Although they have been used in adaptive microscopy [73], their use has not been widespread. The primary limitations of SLMs are their dependence on polarization and wavelength, which will result in some signal loss and requires thorough calibration for compatibility with the, typically, broad fluorescence spectrum of fluorescent markers.

2.3.2 Sensor-less adaptive optics

In sensor-less AO, image-analysis-based algorithms are used to control deformable mirrors or spatial light modulators without the need to measure optical aberrations directly. These iterative algorithms compensate for unknown aberrations and improve image quality by optimizing a merit function based on a parameter such as image brightness [74], [75], contrast [76], [77], sharpness [78] or a merit based on spatial frequency [79]. However, the success of these algorithms depends on the initial guess of the optimization process, the employed algorithm, and the stopping criteria. The optimization process can be influenced by the quality of the initial guess (starting parameters for the iterative algorithm), as well as the algorithm used for optimization. The stopping criteria determines when the algorithm should be terminated, which is important for preventing over- or under-correction of aberrations.

As an example, Albert *et al*. [80] used an optimization algorithm that mimics the process of natural selection to optimize the shape of a deformable mirror. This algorithm, called the genetic algorithm, involves creating a random population of individuals. Then, the population is subjected to a merit function and the most fit individuals are randomly crossed to produce the next generation. Here, an individual is represented by a trial shape of the DM and each individual has 37 “chromosomes”, which correspond to the voltages on the 37 actuators of the DM. The fitness of each individual is evaluated by power of the laser focus in the confocal plane as measured by a PMT (photomultiplier tube). Random mutations are introduced in each generation to prevent convergence to a local maximum. The process continues until the population includes the optimum solution. The level of genetic mutation in the parents of each generation is a measure of the stability of the population and can be used to stop the evolution process. This algorithm allows for finding the global optimum mirror shape that will yield the tightest focus for each beam position on the sample. While sensor-less schemes can be effective, the optimization process requires careful consideration of the initial guess, the stopping criteria and the convergence of the algorithm to ensure successful aberration correction.

Additionally, it is important to note that not all distortions in microscopy images are caused by the sample being examined. While great care is taken to design high-resolution microscopes

that operate at the diffraction limit, aberrations can still arise from imperfections in the optical system. If a lens is used off-axis or with the wrong image conjugate, aberrations can occur to some extent. These distortions can also arise when the system is not used under ideal conditions, such as with the wrong wavelength or temperature.

There are two sensor-less methods available in the MOSAIC to correct system aberrations. One is based on the work of Ji *et al*. [81], where the back pupil of the objective is segmented, and each segment is steered using an SLM to recover a diffraction-limited focus. This is a similar principle to how an SH wavefront sensor measures aberrations. However, in this approach, the slope of each wavefront segment is directly calculated from the displacement of the corresponding light ray from the desired focus. Another technique available for the MOSAIC is based on the work of Hanser *et al*. [82]. Here the wavefront is calculated from the intensities of defocused PSF using a modified Gerchberg-Saxton algorithm. This is done by iterative Fourier transforms of the images starting with a guess phase function. The measured PSF intensity is imposed after each of the Fourier transforms. The implementation of this method in the MOSAIC is discussed in **Chapter 3**.

Chapter 3. Experiment I: Building the LLS

3.1 Introduction

In this chapter, I will detail my work to implement the MOSAIC microscope. To premise my in-depth discussions of challenges and solutions in this implementation, I open this chapter with a description of the microscope as a whole. The MOSAIC microscope is characterized by the following features:

- **Multiple fluorescence imaging modes**. The MOSAIC includes lattice light-sheet microscopy with adaptive optics, structured illumination microscopy (SIM), confocal laser scanning microscopy, multipoint airy scan microscopy, two-photon (2P) laser scanning microscopy, 2P Bessel light-sheet microscopy, 3D single-molecule localization microscopy, among others. A strength of the MOSAIC is the feature to switch quickly between imaging modes and to use them synergistically without the need to transfer or move the sample. This is done with custom-made flip mirrors that can change the optical path within seconds.
- **Aberration correction with adaptive optics**. The MOSAIC has two adaptive components, namely the spatial light modulator (SLM) and deformable mirror (DM). These can be used to correct both aberrations in the excitation light path and in the detection light path. System-induced aberrations come from flawed optical components or imperfect alignment, while sample-induced aberrations originate from optical heterogeneities and refractive index mismatch. The sample-induced aberration correction relies on the use of 2P excitation to form a guide star inside the sample.
- **A fixed hardware design philosophy**. The MOSAIC design is based on custom-engineered optical components and large metal frames, called mainframes, that serve as the support structure. These frames feature well-defined holes and pins to precisely locate the mounting of the optical components.
- **A closed-source control software**. The MOSAIC uses a closed-source LabVIEW-based control software, that communicates with instruments via USB and FPGA (Field-Programmable Gate Array) board. The FPGA provides real-time processing capabilities for data input and output.

- **Large sample chamber**. The MOSAIC features a relatively large sample chamber with a volume of about 40 mL. The sample chamber is also equipped with temperature-control, CO_2 gas control, and evaporation compensation.

While these features are distributed and intertwined across the whole instrument, and not confined to specific areas, **Figure 3.1** exemplifies each feature. Below, I will briefly describe the parts of the instrument, emphasizing the LLS imaging mode, which was my primary focus during my PhD work. Next, I will go into detail on practical considerations pertaining to the construction of the instrument. These practical considerations are the pitfalls that I observed in building the instrument and the solutions to some of them. Finally, I discuss the routine initialization that I perform before imaging which can useful for users of the MOSAIC.

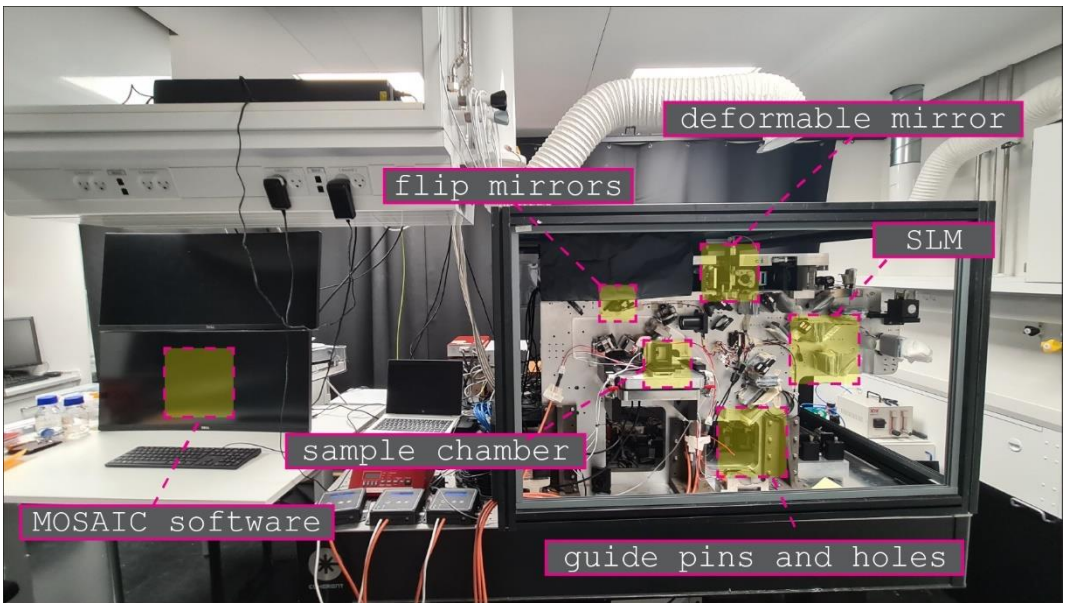

Figure 3.1. The MOSAIC. *The MOSAIC has a couple of features such as flip mirrors to support multiple imaging modes, deformable mirror and SLM for aberration correction, closed-source software, large sample chamber and predefined holes and pins for mounting components.*

3.2 Lattice light-sheet optical path

Due to the confidentiality agreement with Janelia Research Campus, the schematic of the lattice light-sheet optical path cannot be shown in this thesis. However, the primary components of the instrument are shown in this section. The discussion starts from the laser combiner, where the excitation source originates, and ends at the acquisition cameras, where the excitation is detected.

The laser combiner is located in the bottom mainframe of the MOSAIC shown in **Figure 3.2**. Here the excitation lasers are mounted. It also consists of several dichroics and mirrors to align the lasers to coincide with each other into one excitation beam. There are seven excitation lasers with wavelengths 405 nm (diode laser, rated 100 mW), 445 nm (diode laser, rated 100 mW), 488 nm (fiber laser, rated 500 mW), 514 nm (fiber laser, rated 1 W), 560 nm (fiber laser, rated 1 W), 607 nm (fiber laser, rated 1 W), and 642 nm (fiber laser, rated 2 W). The laser intensities are modulated by an acousto-optic tunable filter. Then, the excitation laser passes through a Powell lens to make a light-sheet.

Figure 3.2. Laser combiner. *The laser combiner is used to co-align the excitation lasers. It is located in the bottom mainframe of the MOSAIC. The AOTF modulates the excitation power of the laser. The Powell lens transforms the excitation beam into a light-sheet.*

A cylindrical lens collimates the light-sheet, while another cylindrical lens in a translation stage is used to change the thickness of the beam impinging on the SLM. Next, the lasers reflect off the dichroic stack which is a series of dichroic filters that are stacked together. The dichroic stack separates the different laser wavelengths. The separated beams then impinge onto the SLM which is conjugated to the sample plane and directly imprints the lattice pattern. The beams reflect to the same dichroic stack, which recombines the different laser wavelengths. As detailed later in this chapter, I identified some challenges in aligning this part of the instrument.

An annular mask is located in the pupil plane to block the zero-order diffraction from the SLM. Then, the beam goes into the galvanometric scanning mirrors which are conjugated to the pupil plane and are used to scan the beam along orthogonal axes. These galvanometric mirrors are so-called z-galvo and x-galvo mirrors. Finally, the beam reaches the excitation objective (20x 0.6 NA, WD 5.5 mm). A flip mirror, shown in **Figure 3.3**, is located just before the excitation objective, allowing to redirect the beam into the inspection path. In the inspection path, there are two cameras conjugated to the sample and pupil plane, respectively.

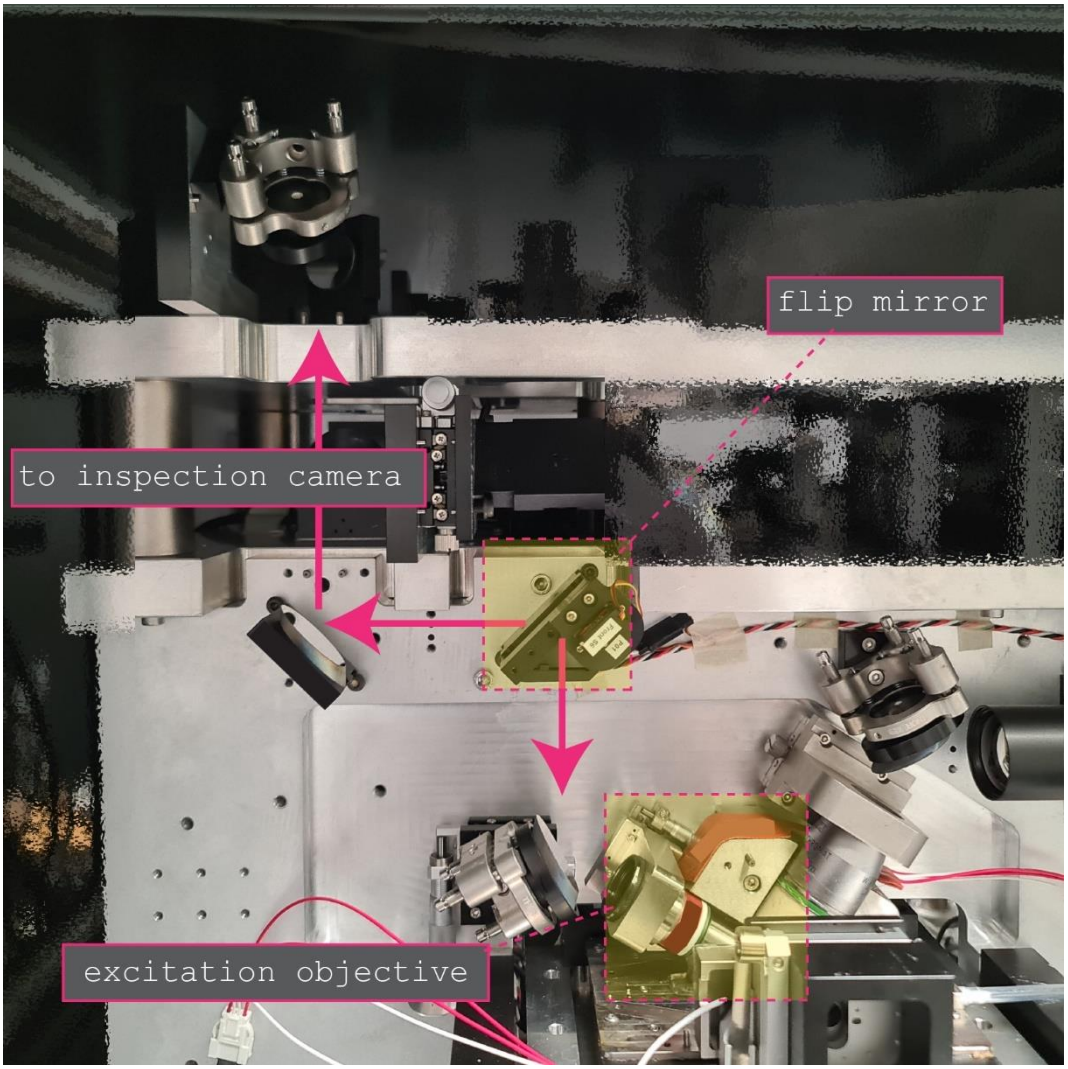

***Figure 3.3. Inspection path**. A flip mirror before the excitation objective can be toggled to direct the illumination beam towards the excitation objective or towards the inspection path. In the inspection path, there are two cameras conjugated to the pupil and sample plane, respectively.*

The detection path starts from the detection objective (20x 1.0 NA, 1.8 mm). Conjugated to the pupil of the detection objective is the deformable mirror shown in **Figure 3.4**. A longpass

dichroic mirror as shown in **Figure 3.5** separates emitted fluorescence into camera A and camera B with a multi-passband filter in front of each camera. These filters can easily be replaced to match the excitation and emission that we want to separate. A schematic of the detection path and our filters is shown in **Figure 3.6**. The longpass dichroic mirror has a threshold at 561 nm while the multi-passband filter has laser-blocking 'notches' centered at 405 nm, 488 nm, 561 nm, and 635 nm. With this configuration, we aim to capture fluorescence from markers excited by the 405 nm and 488 nm lasers in camera A, and fluorescence from markers excited by the 560 nm and 642 nm lasers in camera B.

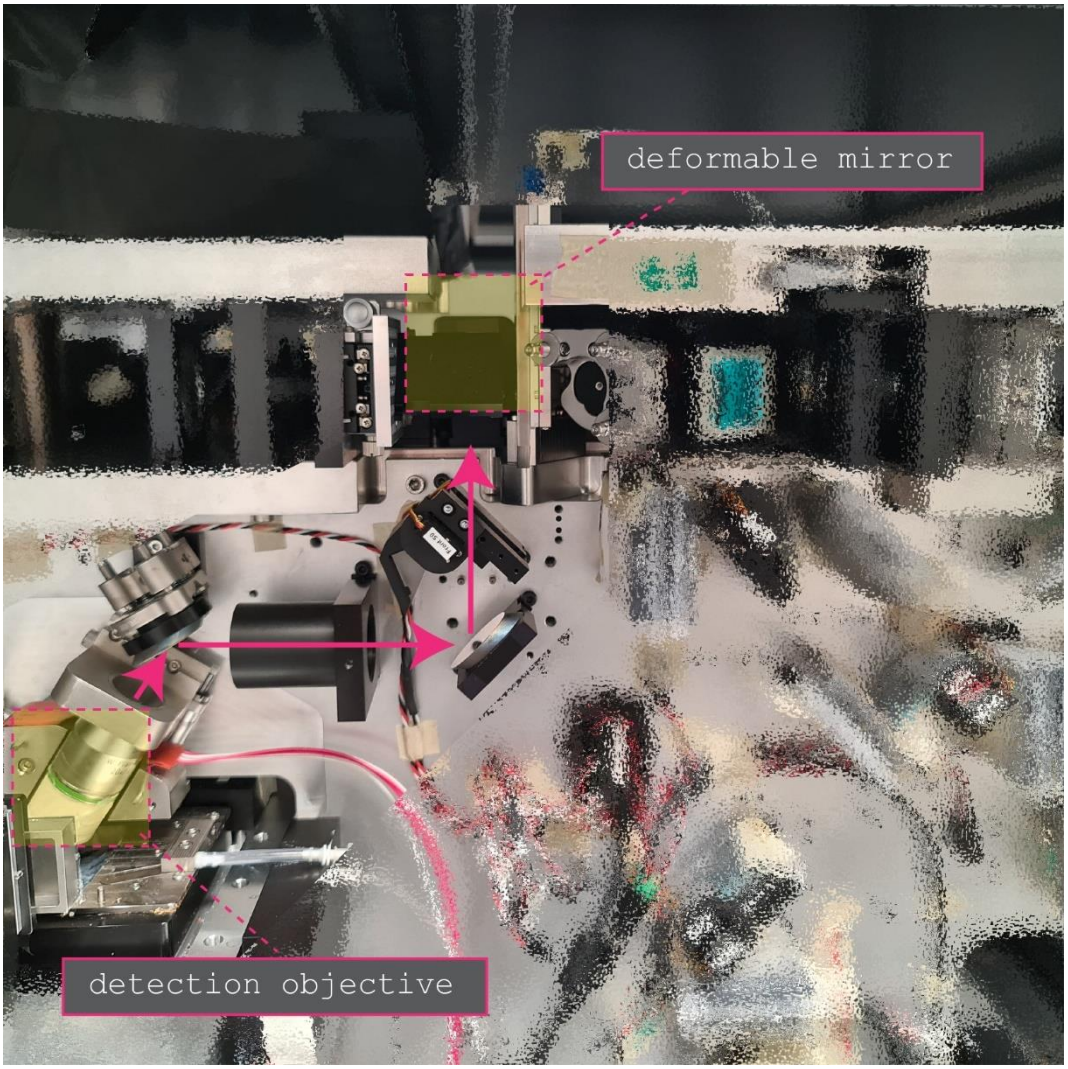

***Figure 3.4. Detection path**. In the detection path, a deformable mirror is conjugated to the back pupil of the detection objective. Arrows indicate the detection path.*

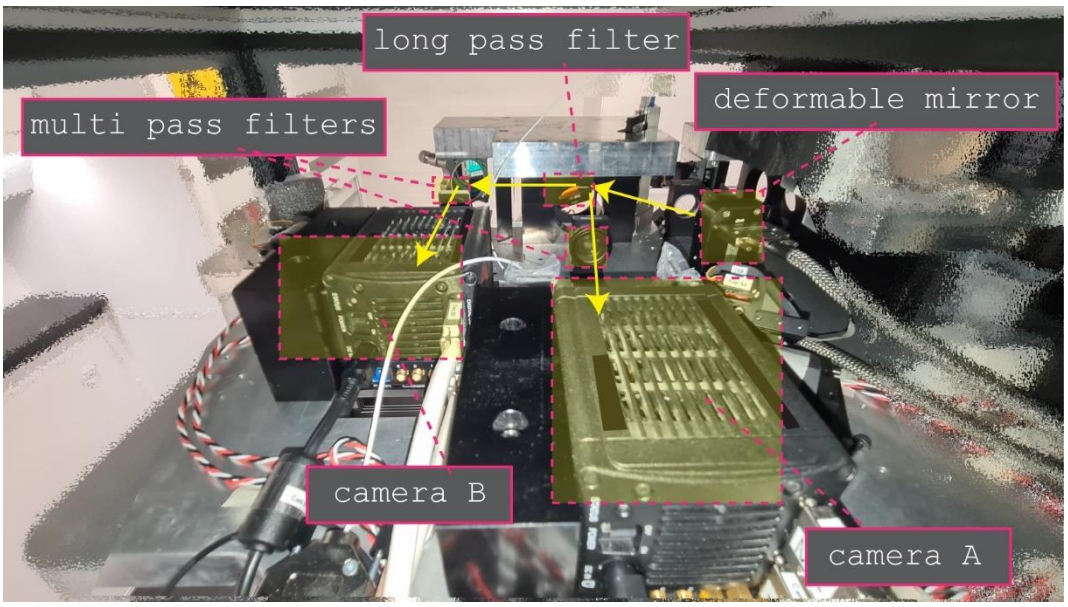

Figure 3.5. Detection cameras. *Cameras A and B are separated by a longpass filter. Arrows indicate the detection path.*

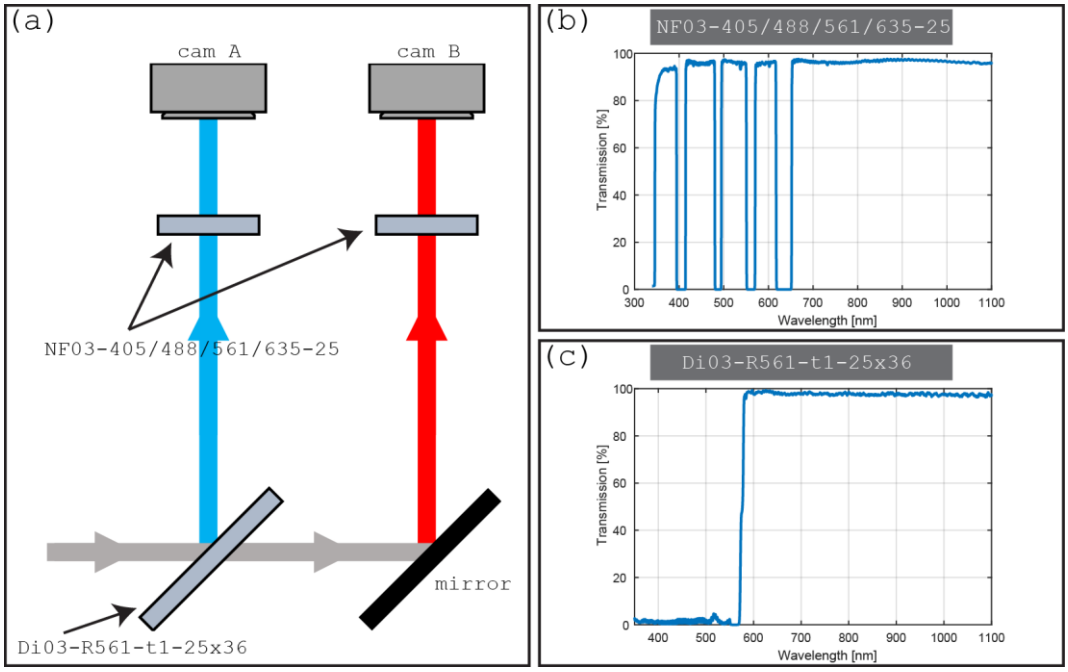

Figure 3.6. Filter configuration*.* ***(a)*** *Schematic of the filters and the camera path. Cameras A and B are separated by the longpass filter (561 nm threshold). A multi-passband filter is used in front of each camera to block the excitation lasers.* ***(b)*** *Multi-passband transmission spectrum.* ***(c)*** *Longpass filter transmission spectrum.*

The optical components of the instrument are not mounted to an optical breadboard with standardized mounting holes. Instead, the components are mounted on custom-made metal mainframes that feature pre-positioned mounting holes specifically designed for the optical components. These mounting positions are secured by small pins or pegs, as illustrated in **Figure 3.7**. The pins and pegs serve to precisely determine the position and orientation of the optical components, ensuring that they are properly aligned and stable.

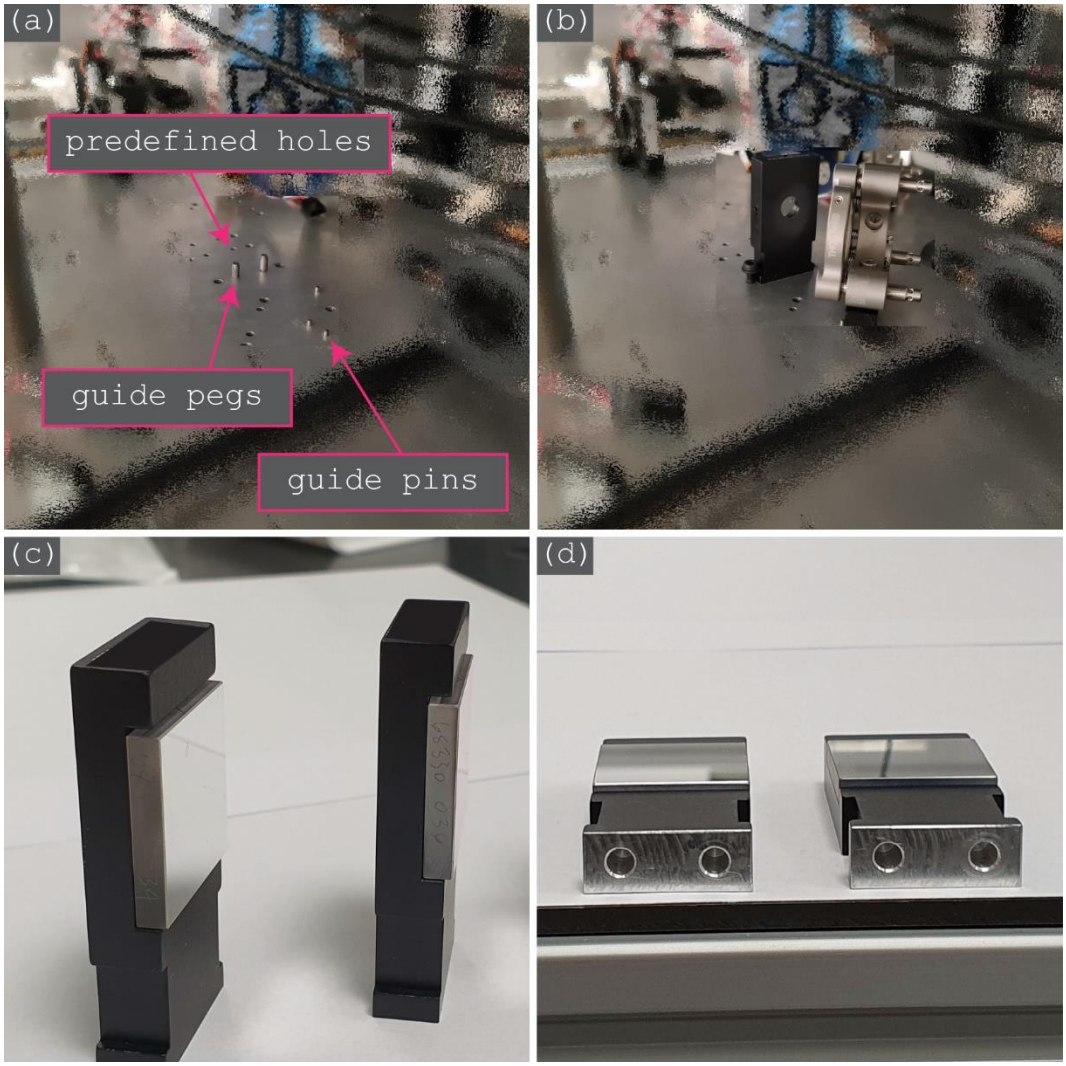

Figure 3.7. Custom made components. (a) *The mainframes have predefined holes and guides.* ***(b)*** *Mounting of the optical components using the predefined holes and guides.* ***(c)*** *Custom-made mirror.* ***(d)*** *Guide holes under the custom-made mirror.*

3.3 Practical considerations

I encountered several challenges while aligning and using the instrument. Some of these challenges are due to manufacturing errors, some are due to the complexity of the optical path, and some are unexpected details that appear after continuously using the instrument. In this section, I describe some of these challenges and how I solved them.

3.3.1 Challenges in the alignment of the beam path

The alignment process of the instrument is designed to be straightforward, relying on the accurate positioning of optical components within pre-defined holes and the use of guide pegs and pins to ensure proper position and rotation. However, this process is dependent on the precise manufacturing of both, optical and mechanical parts. In instances where components are not manufactured correctly, the resulting alignment errors can be challenging to detect and correct, as they may not become apparent until several optics downstream. Furthermore, due to the limitations imposed by the mounting constraints, it can be non-trivial to compensate for these errors with the use of downstream optics.

3.3.1.1 The dichroic stack is not parallel

The dichroic stack, which separates laser wavelengths, is comprised of multiple dichroic filters layered together. The observed issue with our dichroic stack is that the separated beams are not parallel, as shown in **Figure 3.8**.

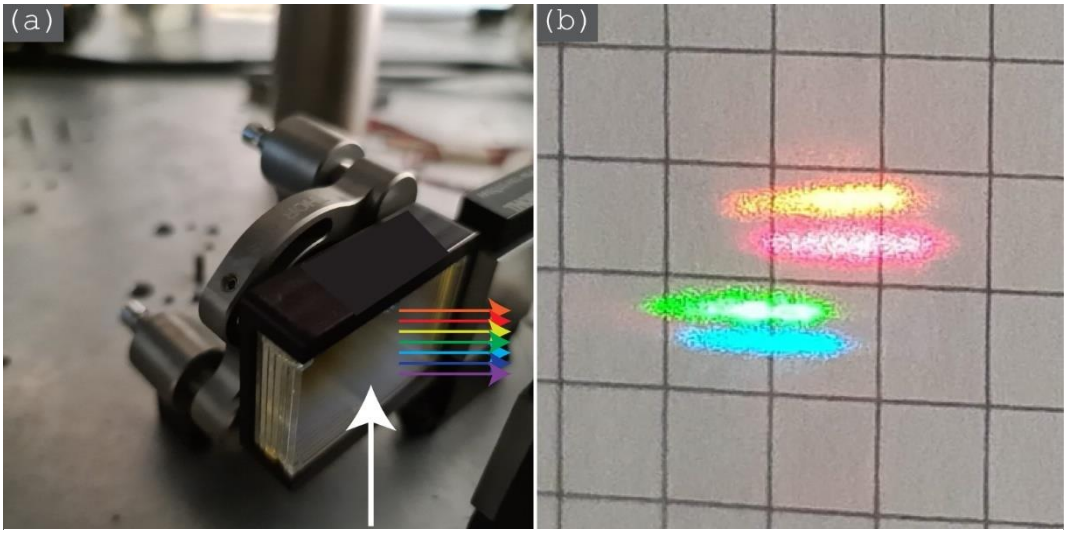

Figure 3.8. Dichroic stack. (a) *The dichroic stack separates the individual excitation lasers.* ***(b)*** *The separated wavelengths are not on the same axis.*

The deviation of the separated wavelengths in the dichroic stack may be caused by a misalignment of the individual dichroic filters, as well as an off-axis alignment of the individual lasers. However, upon testing the stack with a white light laser, the off-axis output of the wavelengths persisted, suggesting that the issue lies with the dichroic stack itself.

We contacted the manufacturer regarding this issue. However, they did not have a solution. Citing that it is challenging for them to quantify the parallelism of the individual dichroic filters and to characterize the performance of the dichroic stack outside of the MOSAIC.

Reports of similar issues with dichroic stacks have been documented by other instrument builders. The effect of this issue with respect to the performance of the instrument is that the different wavelength intensities will not be uniform in the SLM. Despite this, the deviation in our dichroic stack was not so significant, and I was able to compensate for the deviation by adjusting the individual excitation lasers in the laser combiner. However, this also resulted in a loss of optimal alignment with the AOTF, leading to a reduction in power throughput. Nevertheless, in my experience, the output power of the lasers is more than enough.

Recently, the production process of the dichroic stack has undergone a change by the manufacturer, who now uses microbeads instead of glass spacers for the assembly of the filters. The manufacturer claims that this process exhibits improved tolerance for parallelism. However, the performance of the dichroic stack outside of the MOSAIC remains unquantified.

3.3.1.2 Not enough adjustment mirrors

The alignment between the dichroic stack and downstream instruments is critical. One challenge associated with this is that some mirrors share mounting screws, as exemplified in **Figure 3.9**. During the process of securing Mirror 4, I observed that mirror 1 experiences slight movement, which resulted in the misalignment of the whole configuration.

Our solution to this is to grind down the mount of mirror 1 so that it does not interfere with mirror 4. It can also help to remove the pegs in the mirrors to allow for more degrees of freedom in adjustment. My suggestion is to replace these mirrors with kinematic mirrors to allow for more adjustment. Unfortunately, the custom-made metal boards do not allow the mounting of generic kinematic mirror mounts. Moreover, even if a mirror is positioned on the pegs, it can still rotate a bit. It would be useful to have far-away positions for targets, to ensure that the mirrors are perfectly aligned after they are fastened.

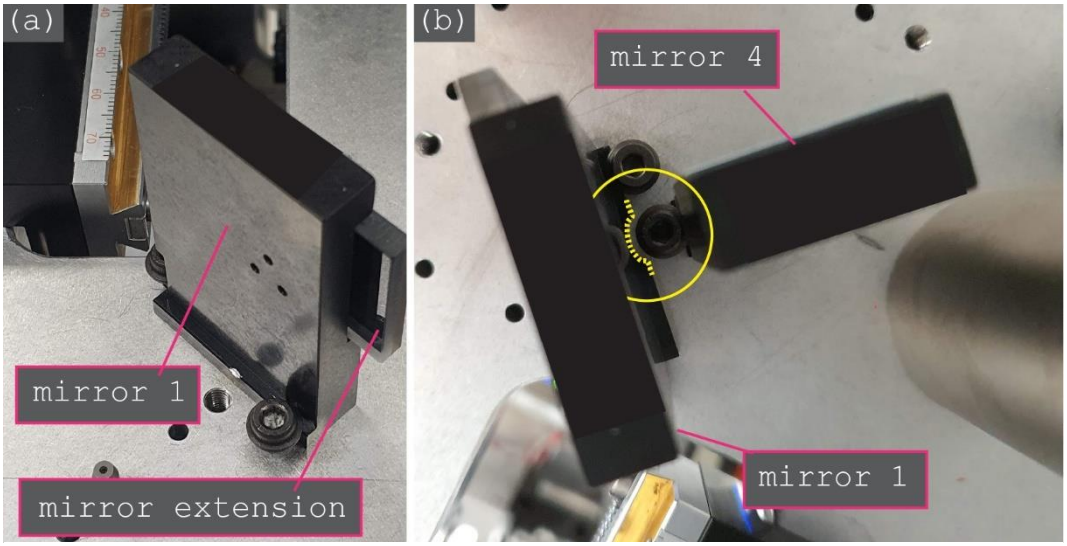

Figure 3.9. Mirror 1 and mirror 4 interfere with each other. (a) *When mounting mirror 4, the mounting bolt pushed into mirror 1 and ruined the previous alignment.* ***(b)*** *Our solution to this is to grind down the mount of mirror 1 so that there is enough space to fasten mirror 4 with a bolt.*

3.3.1.3 Annular mask generates double back reflection

While in LLS mode and applying the hex lattice pattern on the SLM, the pupil-conjugated alignment camera shows unexpected patches of light (circles in **Figure 3.10a**) in places that should have been blocked by the mask. These patches of light are parts of the 6 spots of the hex lattice pattern as shown in the projection of the beam in front of the z-galvanometric mirror (**Figure 3.10b**). I figured that these reflections originate between the back side of the mask and the AR-coated windows in a mount positioned after the mask.

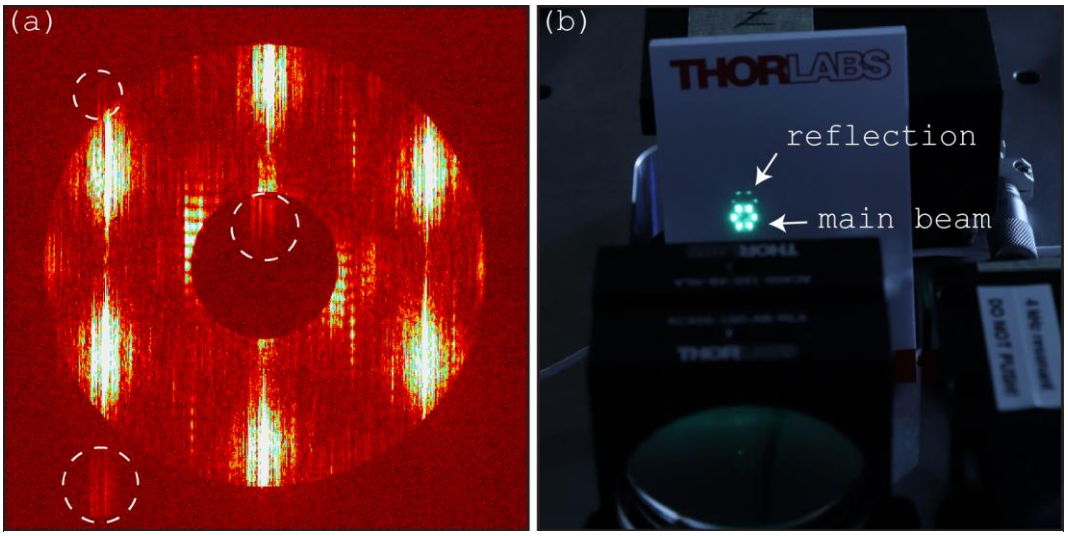

Figure 3.10. Double back reflection. (a) *double back reflection as seen in the pupil conjugate inspection camera.* ***(b)*** *double back reflection projection in front of z-galvanometric mirror.*

First, the beam travels through the annular mask. Then, a small fraction of the beam, which is less than 1.25% (according to the specifications of the AR-coated window), gets reflected back upstream towards the mask. Subsequently, this light is reflected back downstream with almost 100% efficiency from the reflective back side of the mask.

It should be emphasized that the double reflections are only visible when the laser power is set to a high setting (>100 mW) and the mask is set to 0.600/0.200 (outer NA/inner NA), which is not intended for the hex lattice.

I propose that the reflection from the mask could be reduced if the mask is flipped. That is, if the downstream-facing side of the mask was dark instead of the silver-colored/coated. The mask could be absorptive in future iterations of the setup or the downstream AR-coated windows could be removed altogether. For the current set-up, I removed one of the windows.

3.3.1.4 The periscope mirror is thicker than intended

The thickness of the periscope mirrors in **Figure 3.11** exceeds the specifications. The periscope setup consists of a bottom mirror and a top mirror. A comparison of the thickness of these mirrors with the 3D model indicates that the top mirror and the bottom mirror are, respectively, 1.1 mm and 2.9 mm thicker than intended. These mirrors are not mounted on kinematic mounts, which made the adjustments challenging. To compensate for the deviation, I manually removed the guide pegs and repositioned them.

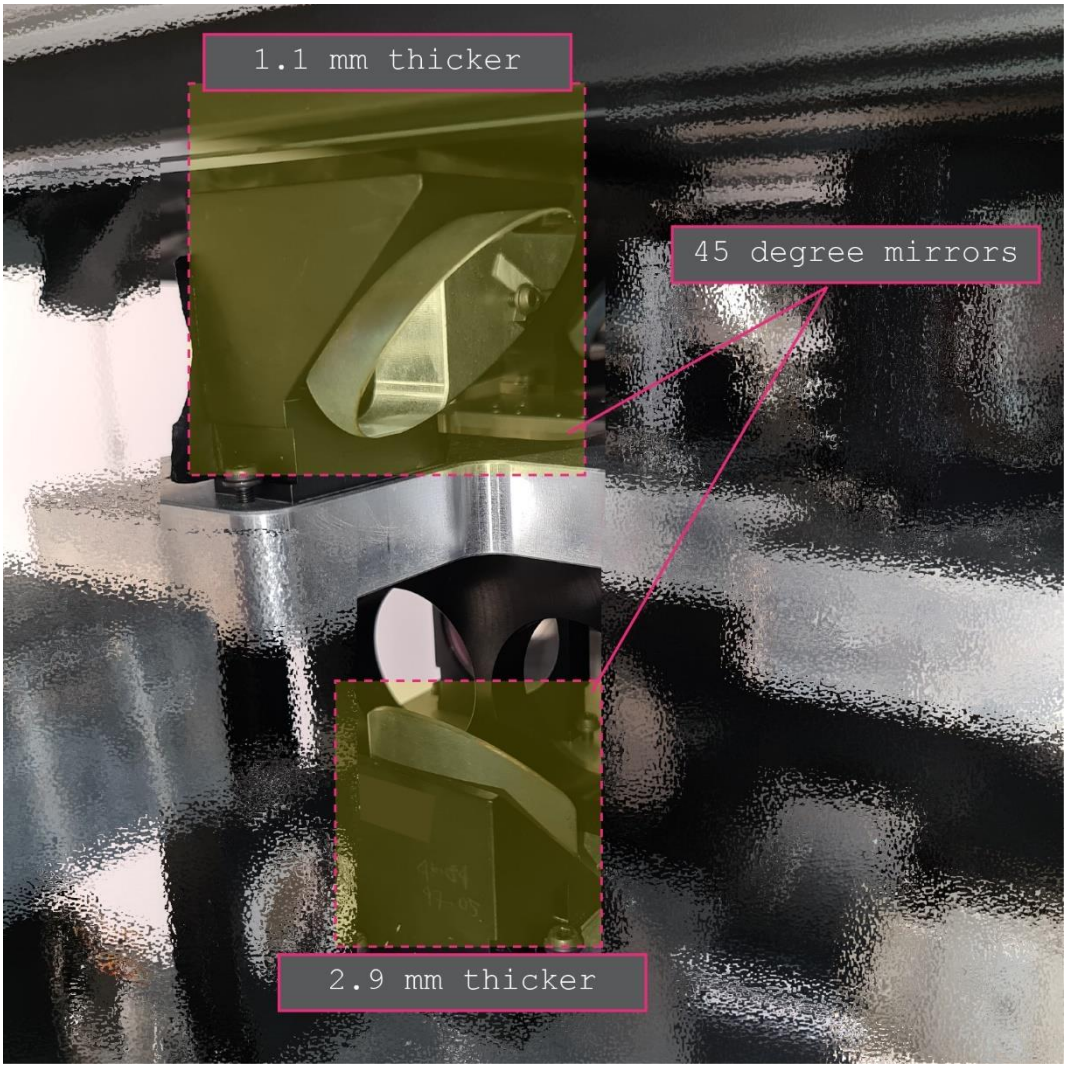

Figure 3.11. Periscope mirror. *The mirrors thickness is not as expected. The top periscope mirror is 1.1 mm thicker while the bottom mirror is 2.9 mm thicker than intended. This results in unintended offset of the beam after the periscope formed by the two mirrors.*

3.3.1.5 Elliptical mirror is flawed

After aligning the LLS path, I used the sample inspection camera to evaluate the profile of the beam. Upon inspection, I observed that the Bessel beam was severely aberrated, as shown in **Figure 3.12a**. To identify the source of this aberration, it was necessary to inspect the beam in front of each optical component. This posed a challenge due to the limited space available for the additional mirrors and cameras required to pick off the beam. In some cases, it was necessary to use multiple mirrors to redirect the beam to an auxiliary camera.

Through this pick-off method, I was able to determine that the aberration was caused by the mirror (show in **Figure 3.12**). The mirror is a custom-made optical component composed of

three parts: an elliptical mirror, a custom-made mirror frame, and a mirror mount. The mirror is glued to the frame and then the assembled component is mounted into the mount.

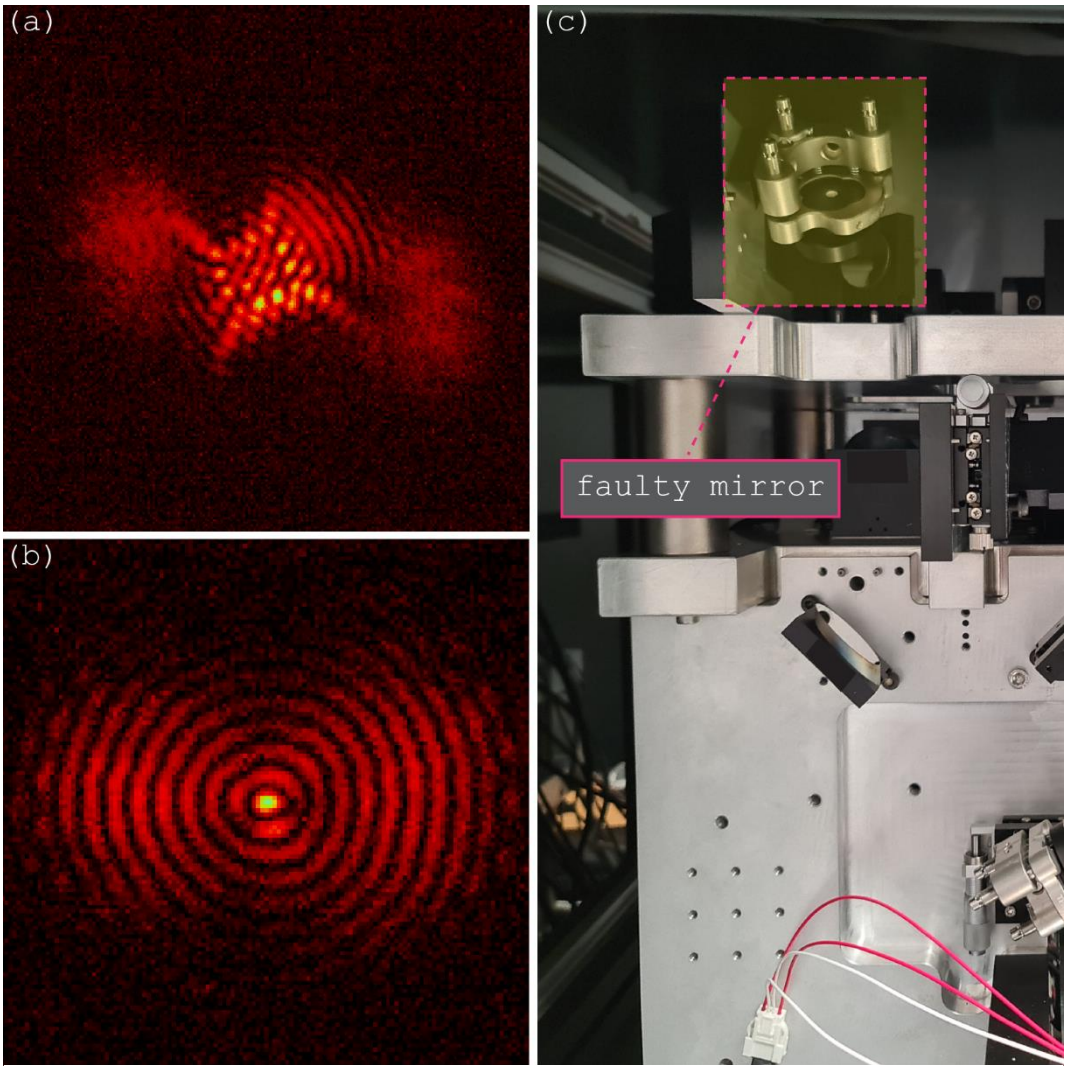

Figure 3.12. Faulty mirror. (a) *Aberrated Bessel beam viewed on an inspection camera.* ***(b)*** *Unaberrated Bessel beam.* ***(c)*** *Faulty mirror causing the aberration.*

The initial method of gluing the mirror to the frame may have resulted in a distortion or warping of the mirror surface. Originally, I used superglue and applied it to the entire front face of the frame. Upon considering this as a possible contributor to the observed aberration, I modified both the type of adhesive used and the application method. I used epoxy instead of superglue and applied it through a hole that I drilled in the backside of the frame. The holes were approximately 3 mm in diameter.

The revised method for attaching the mirror to the frame seems to have improved the beam profile, as shown in **Figure 3.12b**. However, it remains inconclusive whether the observed aberration was solely attributed to the previous gluing method or if the mirrors were inherently flawed. While the flatness of the mirror was not directly assessed here, the deviation from an ideal Bessel beam profile was used as an indicator. Correction for less severe mirror aberrations can also be achieved by using the SLM for pupil wavefront correction, as discussed in **Chapter 3**.

3.3.2 Challenges in alignment in the sample chamber

Next, I outline challenges that I encountered during the usage of the imaging instrument. These challenges are associated with imaging fluorescence-labeled samples and refractive index matching for aligning the light-sheet.

3.3.2.1 Detection objective absorbs fluorescein

During my initial imaging experiments, I noticed that, after 10-15 min, there was a strong background fluorescent signal arising from the sample chamber. Eventually, I established that the detection objective was leaching fluorescent dye, absorbed during previous experiments, when submerged in the medium.

Figure 3.13 shows how the background signal increases over time in the sample chamber. These images were captured by the endoscope camera that can view inside the sample chamber. In this experiment, at timepoint t=0 min, I added 40 mL of PBS in the sample chamber and activated the 488 nm excitation laser at 100 mW. This setting is much higher than what I use to image cells, but here the goal was to probe where the fluorescent signal originated from. During the first 5 min (**Figure 3.13a-b**), there was no background fluorescence as one would expect when imaging PBS. However, after 10 min (**Figure 3.13c**), the background signal became visible and increased even more after 15 min (**Figure 3.13d**). I removed the fluorescent PBS and replaced it with fresh PBS and repeated the same experiment 20 times for a total of 5 hours. I observed the same effect of the fluorescence appearing after about 10 to 15 min. This experiment suggests that the source for the background is either the objectives or the sample

chamber itself. Moreover, the signal did not seem to diminish after 5 hours of trying to dissolve the fluorescence.

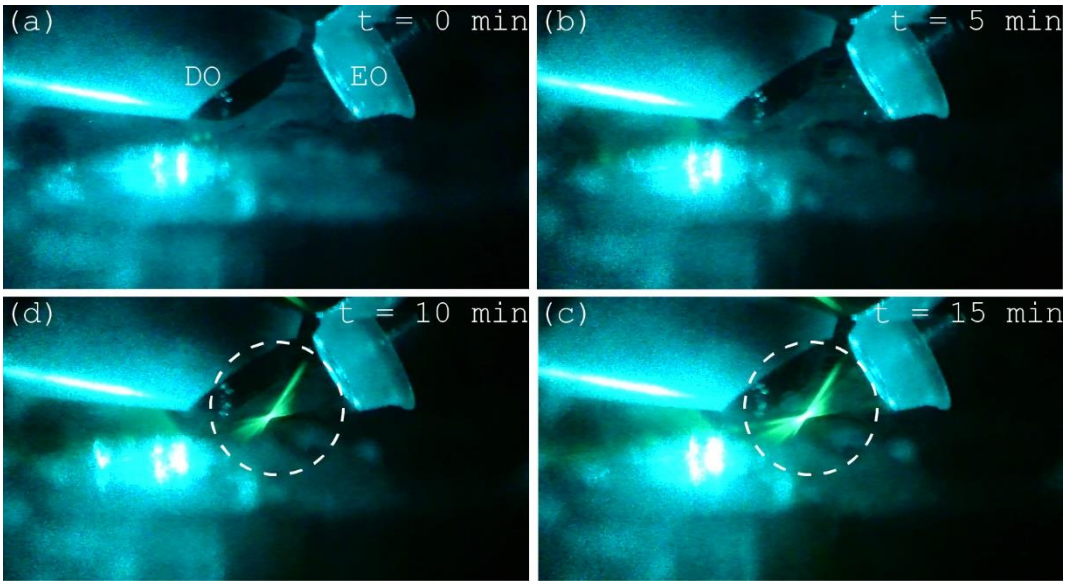

Figure 3.13. Background fluorescence*. The detection objective leaches fluorescein into the sample chamber.* ***(a),(b)*** *No visible background fluorescence is observed from 0 min to 5 min.* ***(c),(d)*** *There is a strong fluorescence background after 10 min that increases in intensity at 15 min. DO is the detection objective while EO is the excitation objective.*

I checked if the sample chamber was a source of the fluorescence by filling PBS in the sample chamber but not submerging the objectives. After 20 min, the objectives were submerged, and I observed that there was no background fluorescence. This suggests that the sample chamber was not a source of the background fluorescence. Finally, I isolated the detection and excitation objectives. I removed only the detection objective while keeping the excitation objective attached and repeated the same experiment of imaging every 5 min. I observed no background fluorescence even after 20 min as shown in **Figure 3.14**. As a final check, I reinserted the detection objective and repeated the experiment. Now I noted that the fluorescence background appeared again after 10-15 min, similar to **Figure 3.13**.

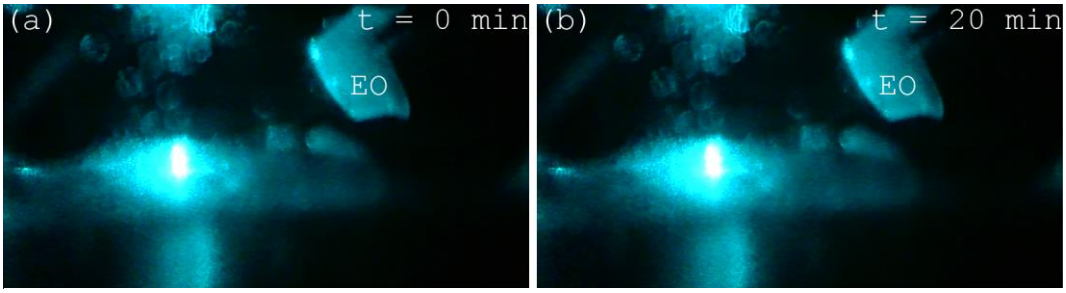

Figure 3.14. Background fluorescence without the detection objective*. Without the detection objective there was no background fluorescence arising between the two timepoints.* ***(a)*** *t = 0 min.* ***(b)*** *t = 20 min.*

Upon inspection of the detection objective, I noticed a yellow ring around the rubbery material near the tip of the objective as shown in **Figure 3.15**. This is where I suspected that the objective absorbed the fluorescent dye. When exposing the detection objective directly to the the 488 nm excitation laser, the yellow ring seemed to emit fluorescence. I tried to wash and wipe the fluorescent ring. However, neither PBS, nor water, nor acetone, nor alcohol were effective in removing the fluorescent ring. I contacted the manufacturer, but they could not offer any solution. They, however, confirmed that the rubber material is only on the exterior of the objective and that the fluorescent dye cannot reach the inside of the objective via the rubber material.

Figure 3.15. Fluorescein absorbed by the detection objective*. The detection objective absorbs fluorescent dye (fluorescein) from the medium. The dye slowly leaches during imaging and causes a high background.*

As a short-term solution to this problem, I covered the rubber part of the objectives with parafilm. A permanent solution would be to replace the objective with a new one or to completely dissolve the absorbed dye. However, it is part of the initialization routine to image the light-sheet in a dye solution to check for correct alignment. Thus, the objective will always be exposed to dye during routine imaging, and there will always be the risk of dye being absorbed unless the detection objective is covered.

Our collaborators in Boston also reported that their objective absorbed fluorescent dye. However, for them, it was the excitation objective and not the detection objective that absorbed the dye. Their solution was to use Alexa488 dye instead of fluorescein during the routine alignment of their light-sheet. I suspect that it was also the fluorescein that was absorbed in my detection objective and switched to Alexa488 since then. However, I did not test if the detection objective absorbs only specific dyes.

This issue may be unique to this version of the lattice light-sheet microscope. In the earlier version of the lattice light-sheet microscope, the sample holder and sample chamber were considerably smaller and only the tips of the objectives touched the imaging medium.

3.3.2.2 Spatial shift of the light-sheet due to a change of medium

I observed that there was significant translation in the focus of the light-sheet when aligning using Alexa488 dye in water compared to Alexa488 dye in medium.

It is common practice to align the light-sheet with a mixture of fluorescent dye in water. For example, when imaging large samples, such as a whole zebrafish, the fish is kept inside a tiny FEP (fluorinated ethylene propylene) tube with medium. The tube is submerged in water during light-sheet imaging. For this configuration, the amount of medium around the sample is negligible compared to the surrounding water. Therefore, the light-sheet is aligned with fluorescent dye in water.

For the MOSAIC, however, the sample is mounted on a glass coverslip and is completely surrounded by medium during imaging. Furthermore, the objectives have substantial working distances, which amplify the impact of the index of refraction of the medium. **Figure 3.16** shows the alignment of the light-sheet with Alexa488 dye in water versus Alexa488 dye in medium. The light-sheet becomes defocused and is also shifted to the right, when changing from water to medium. This translation and the defocus is consistent with the change in the index of refraction of the medium. To address this issue, a mixture of Alexa488 dye and the intended imaging medium is used during alignment instead of using dye dissolved in water. The disadvantage is that a lot of medium is expended.

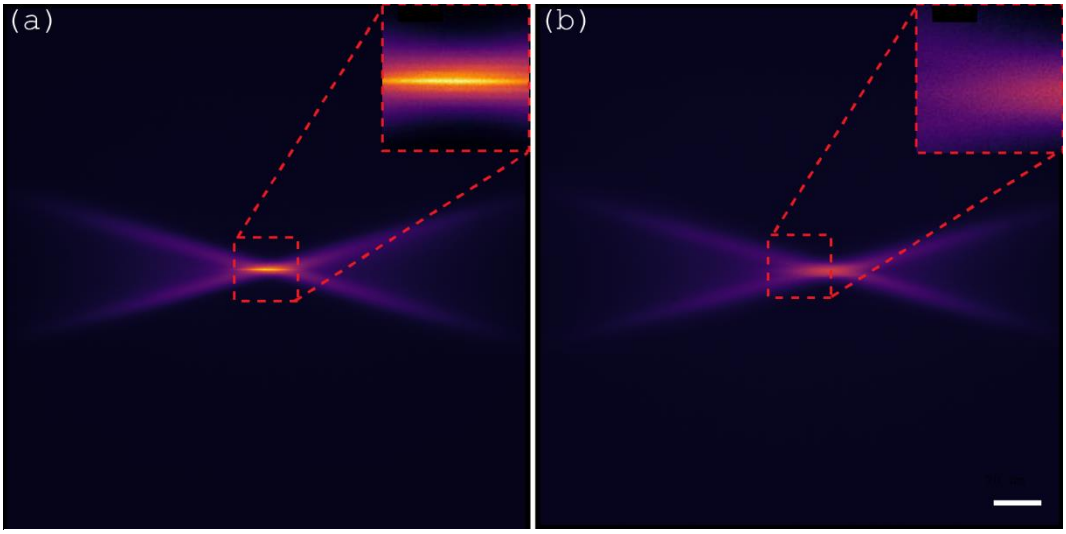

Figure 3.16. The focal plane of the light-sheet shifts when changing medium. *The light-sheet falls out of focus and is translated along the optical axis of the excitation objective, when changing from water to medium. The scalebar is 20 µm.*

3.4 Initialization routine

It is good practice to confirm that the LLS is aligned before commencing live sample imaging. Below, I describe the initialization routine that I perform to ensure that the light-sheet is aligned inside the sample chamber, that the temperature is stable, and that the PSF is near-optimal. This routine is performed before every experiment detailed in this thesis.

The instrument is turned on two hours before the experiment to allow for the temperature to equilibrate. The excitation lasers, cameras, deformable mirror, sample stage controllers, and the galvanometric scanning mirrors are turned on (other electronics not in this list are always on). The optical path is set to LLS and the excitation beam is directed to the inspection camera to check the beam profile. The SLM is set to Bessel beam mode for the 488 nm, 560 nm, and 642 nm lasers and the 0.400/0.300 mask is used. The sample inspection camera is used to check that the center of the beams coincide with each other while the pupil inspection camera is used to check that the mask is centered along the optical path.

Then, the flip mirror is positioned to direct the path to the excitation objective. To align the light-sheet, it is imaged in a dye solution. The solution is prepared by adding Alexa488 dye (final concentration = 0.13 µM) to preheated (37 °C) medium to make a final volume of 37.5 mL. The fluorescent solution is then transferred to the sample chamber. The sample chamber is moved 10 mm up to immerse the objectives. The sample chamber is heated at 37 °C with an

evaporation compensation of 1.5 mL/h, and with a 5 % CO_2 supply. The sample chamber is allowed to equilibrate for 10 min.

After 10 min, I imaged the fluorescent solution. The illumination is set at 488 nm, 100 mW, 100 % AOTF power, and 200 ms exposure. The detection objective is translated to focus on the excitation beam. It is useful to use a limited FOV of the camera (either 256 × 256 pixels or 128 × 128 pixels) to see the beam more closely. The excitation objective was translated to position the excitation beam in the center of the FOV of the camera.

Two mirrors before the excitation objective, shown in **Figure 3.17**, are then adjusted slightly to further align the excitation beam. Mirror A can be translated, to make sure that the light-sheet is straight along the x-axis of the camera FOV. While mirror B can be tilted to make sure that the light-sheet is in the center of the FOV. It is useful to define two regions of interest (ROIs) on both sides of the camera FOV and compare the maximum intensities of the ROIs to make sure that the beam is centered. Lastly, mirror B can be translated to make sure that the excitation beam is in the focal plane of the detection objective. For this alignment, the imaging parameters are changed to 50 ms exposure and the z-galvanometric mirror was set to dither 10 µm to check that the maximum intensity occurs at the focal plane of the detection objective.

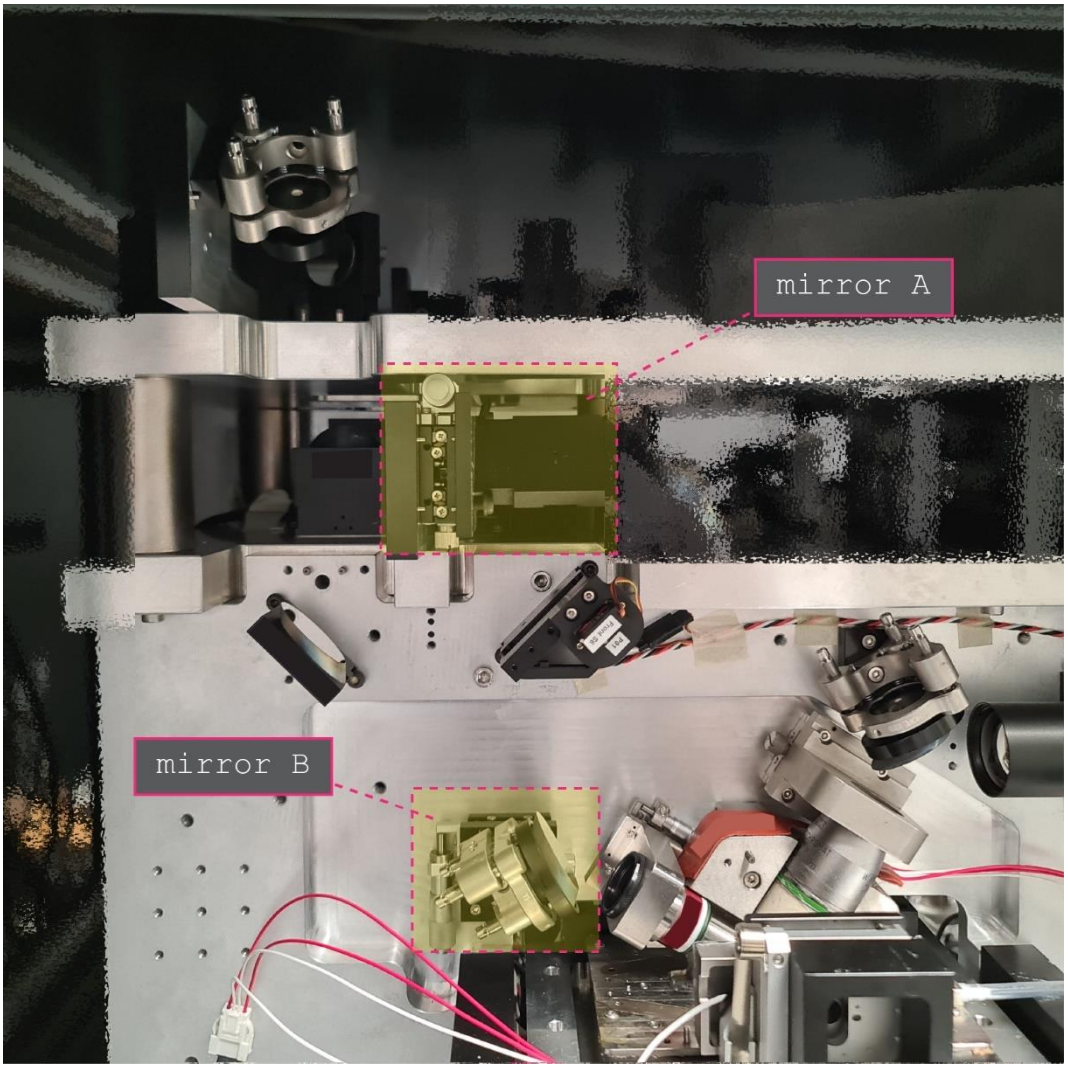

Figure 3.17. Mirrors to help align the light-sheet*. To help align the light-sheet, mirror A can be translated while mirror B can be translated and titled.*

3.5 Discussion

I have implemented and built the instrument following the blueprints of the Betzig group. Although the design of the lattice light-sheet microscope is documented with much detail, it is not without flaws. During the building of the lattice light-sheet, I had firsthand experience with some complexities and issues that could be solved or simplified. The items that I have outlined in the section titled '**Practical considerations**' are my contribution to help other builders of the MOSAIC.

The design philosophy behind the MOSAIC was modular. This means that there are guides such as holes, pins, and pegs that snap the custom-made components into their positions. This

makes the building process straightforward. However, this relies on very precise manufacturing of the custom-made components. If one component is misaligned or has a manufacturing error, it becomes challenging to compensate due to the absence of adjustment mechanisms in most components. Furthermore, these types of errors are not easy to recognize. Sometimes they only become apparent downstream the optical path. I suggest incorporating more mounting holes for distant alignment-target positions since the fixed mirror can still experience slight movement on the alignment pins. This can help check if the fixed mirrors are mounted appropriately. This would be particularly useful for aligning components near the SLM.

Some of the custom-made parts have only been designed recently and are not matured in terms of being characterized precisely. The parallelism of the dichroic stack, as I reported above, is an example of this. Moreover, some custom-made components have no application outside the MOSAIC microscope and thus, it is also difficult for the manufacturer to give feedback on their performance.

My discovery of the dye being absorbed in the objective is quite new and unexpected. These objectives are water-immersion objectives and are supposed to handle submergence in water containing fluorescent sources. I proposed a solution by covering the objective. Another solution could be to change the angles of the objectives. Because of the geometry of the objectives and the size of the sample chamber, the objectives need to be submerged deep into the chamber. If the detection objective is tilted more vertically, then the water level might not reach the rubber part of the objective. In the previous versions of the lattice light-sheet, the sample chamber and holder are smaller and only the tip of the objectives are submerged in the medium. Thus, the absorbance of fluorescent dye by the objectives was not a problem.

Lastly, I observed that the shift in the light-sheet when changing the imaging medium was significant for the instrument especially since the objectives have long working distances. This must be considered when imaging with the light-sheet in a different medium. Additionally, the temperature of the chamber could also have an effect on the index of refraction of the imaging medium. Thus, the user should give some time for the sample chamber and the medium to equilibrate in temperature.

Chapter 4. Experiment II: Optimizing the LLS

4.1 Introduction

In this chapter, I describe the optimization process that I applied to the LLS path to obtain the lattice illumination profile and imaging PSF shown in **Figure 4.1**. Some of these optimizations are based on previous work of other groups. Here, I describe the principles behind these optimizations and discuss how they are applied to the MOSAIC. I discuss the SLM calibration where the LLS pattern is created. Additionally, I describe two system-aberration correction methods implemented in the LLS. The pupil wavefront correction is used to correct aberrations in the excitation path, while phase retrieval is used to correct aberrations in the detection path. Lastly, I address the optimization of the sample chamber for long-term live sample imaging.

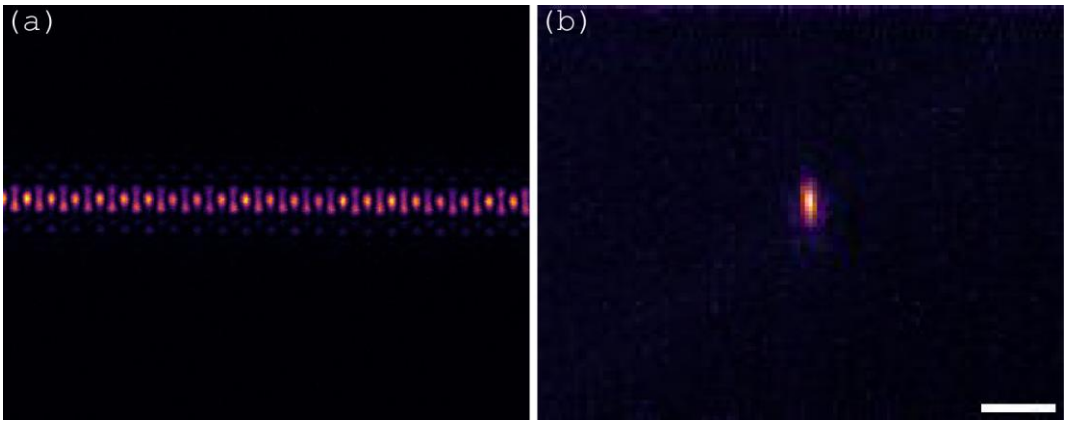

Figure 4.1. Lattice light-sheet illumination profile and imaging PSF. (a) *Square lattice excitation beam captured with the sample inspection camera.* ***(b)*** *Imaging PSF using 0.1 µm fluorescent bead. The scale bar is 2 µm.*

4.2 Optimizing the excitation and detection paths

4.2.1 SLM calibration

The lattice pattern is encoded in the light-sheet by the spatial light modulator (SLM). An SLM is a device composed of an array of birefringent liquid crystals that exhibit different indices of refraction depending on the orientation of the crystals. The local variation in the index of refraction produces a phase difference that results in the creation of the lattice pattern, once the

zero-order reflection from the SLM is subsequently removed by a mask. The orientation of the liquid crystals can be adjusted by modulating the voltage applied to the SLM, as demonstrated in **Figure 4.2**. Additionally, the index of refraction of the liquid crystals is also dependent on the wavelength of the laser that is being modulated. Therefore, to accurately modulate the lattice pattern, a separate calibration is required for each of the seven lasers available in the instrument. However for the MOSAIC, instead of having a global calibration for each wavelength, the SLM is divided into seven regions that are locally calibrated to each wavelength. This enables simultaneous imaging with multiple wavelengths.

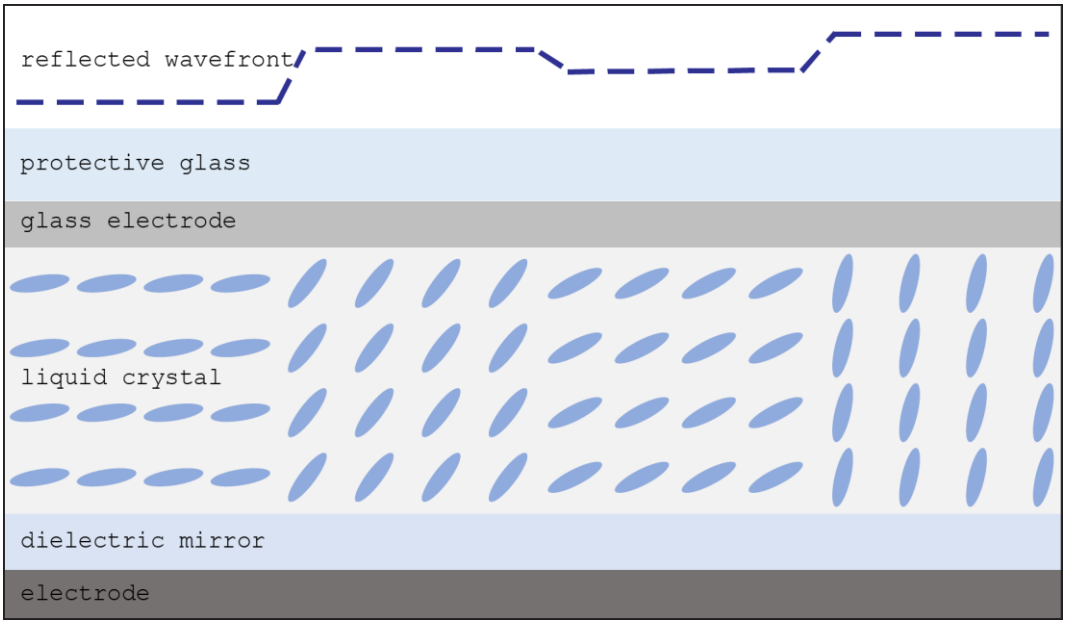

***Figure 4.2. SLM liquid crystal array**. The SLM is composed of liquid crystals that have different indexes of refraction depending on their orientation. The orientation of the liquid crystals is controlled by the voltage between the electrodes.*

The input to the SLM is an 8-bit grayscale image and each pixel gray value corresponds to an orientation of the liquid crystals. However, it is more useful to know how the gray value affects the phase of the reflected beam instead of how it affects the orientation of the liquid crystals. This is the purpose of calibrating the SLM – to determine how the phase changes with the input gray value. The setup for the SLM calibration is shown in **Figure 4.3**.

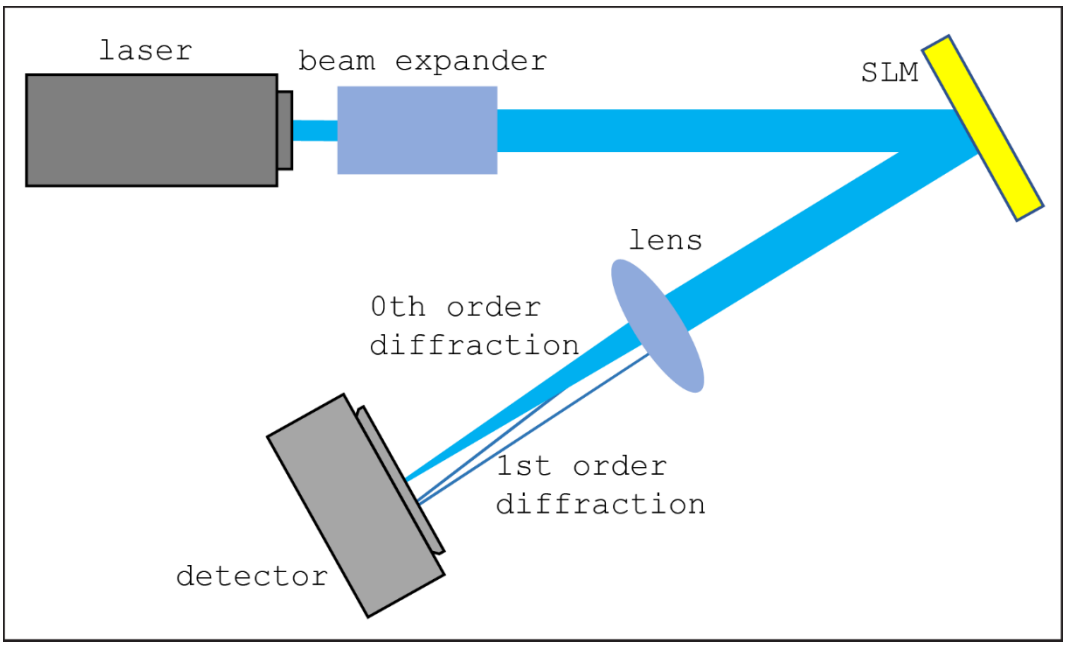

Figure 4.3. SLM calibration setup. *A grating pattern is encoded in the SLM and is imaged in the focal plane. The grating height is varied, and the first-order intensity is measured. In the MOSAIC, this optical path can be modelled by using the SIM path (which allows to illuminate the whole SLM with a single laser) and imaging at the pupil-conjugate inspection camera.*

For the SLM calibration of the MOSIAC, the optical setup in **Figure 4.3** is equivalent to the SIM illumination path with the imaging path directed toward the inspection cameras. The whole SLM is illuminated by the excitation beam and the mask is set to empty. The diffraction from the SLM is measured at the Fourier conjugate plane by the pupil inspection camera. A step grating pattern is loaded to the SLM. The period of the step grating is 6 pixels and the step height is varied from 0 to 255 grayscale value. As the grayscale value is increased, the intensity of the first-order diffraction is measured. A cosine graph is fitted, and the curve is used for the calibration of the grayscale value and the process is repeated for each of the laser wavelengths. This can be automatically perform using the MOSAIC software. As an example, the grayscale value versus the first-order diffraction intensity for 514 nm excitation is shown in **Figure 4.4**. The intensity drops back to minimum at 160 grayscale value. Meaning that the useful range of grayscale value for 514 nm is only from [0,160]. The whole [0,255] range is remapped to [0,160]. That is, a 2π phase shift corresponds to 160 grayscale value.

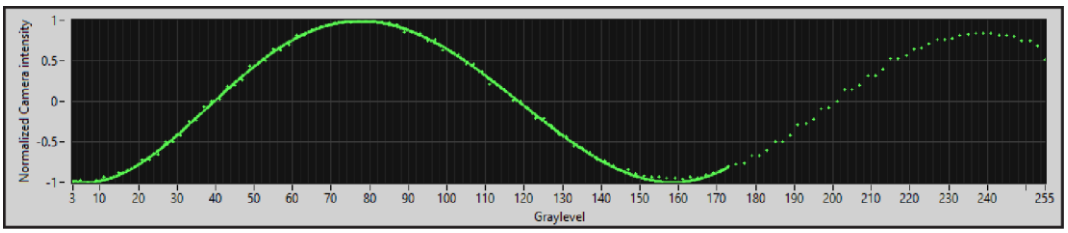

***Figure 4.4 Grayscale value vs first-order diffraction intensity**. A cosine graph is fitted to the input grayscale value versus the diffraction intensity.*

The result of the phase calibration is shown in **Figure 4.5**. The uncalibrated hexagonal lattice (**Figure 4.5a**) and square lattice (**Figure 4.5b**) show a characteristic stripe pattern which makes their intensity non-uniform. This 'striping' is a result of incorrect wrapping of the phase. In contrast, the calibrated hexagonal lattice (**Figure 4.5c**) and calibrated square lattice (**Figure 4.5d**) have a more uniform intensity over the field of view. For the single Bessel beam, the difference between a phase calibrated and uncalibrated pattern is less noticeable since it only spans a small field of view.

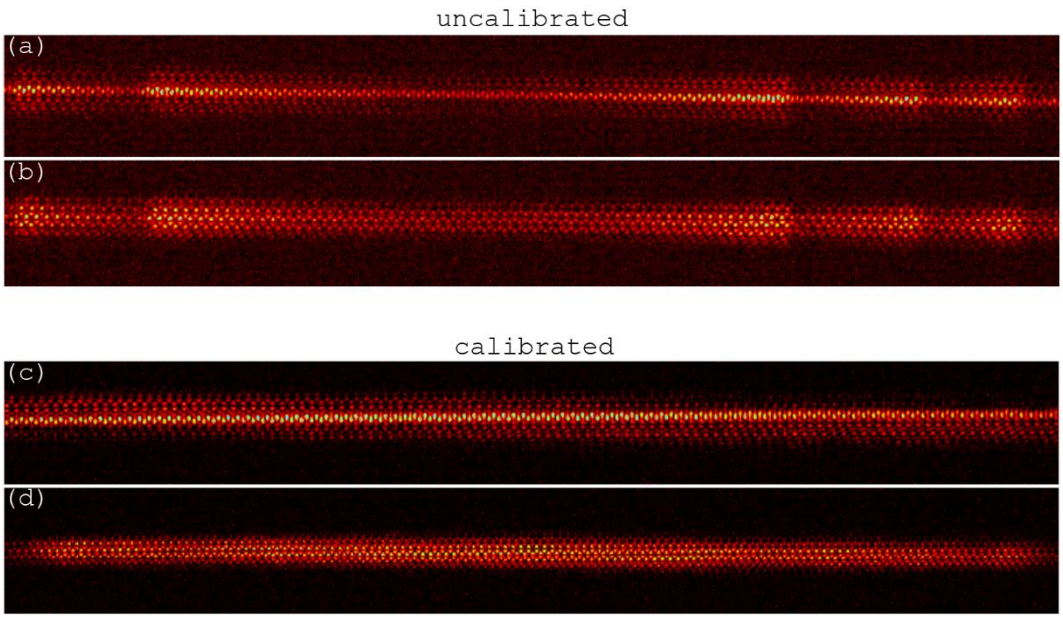

***Figure 4.5. SLM phase calibration result**. **(a)** Square lattice prior to phase calibration. **(b)** Hexagonal lattice prior to phase calibration. **(c)** Square lattice after the phase calibration. **(d)** Hexagonal lattice after phase calibration. The uncalibrated lattices show stripes which result in discontinuous phase wrapping. The calibrated lattices, on the other hand, have more uniform intensity.*

4.2.2 Pupil wavefront correction

Another application of the SLM is to correct system aberrations in the excitation path. We implemented the wavefront correction technique following the work by Ji *et al.*, [83]. This method is based on the idea that a diffraction-limited focus is formed when all rays intersect at a common point and are in phase to maximize interference. The presence of inhomogeneities in the sample can cause the deflection of light rays or introduce phase shifts, leading to aberrations in the focus. By conjugating the SLM to the back pupil of the objective, it is possible to steer the rays back into focus and compensate for the phase shifts. It is not possible to correct the unlimited number of light rays, but the SLM can be split into N regions for correction purposes. The number of regions can be increased to enhance the correction. However, according to Ji *et al.*, an N value of about 100 is adequate for microscopy applications, especially when the variations are smooth.

The schematic of this procedure is shown in **Figure 4.6**. First, a reference image is captured with all the N beams 'on'. Then, all but one of the N beams is turned 'off'. This is done by putting a phase ramp in the N-1 subregions so that they are directed to a field stop. The inhomogeneity in the sample is manifested by a translation of the focus relative to the reference image. To measure the translation of the focus, the positions of the centroids are compared. For more complex samples, image correlation can be used for measurement. From the translation of the focus, the deflection angle can be calculated, and the opposite value can be imparted by the SLM with the appropriate phase ramp for the subregion. This is repeated for all the N subregions until all the N beams intersect at a common point.

After correcting for beam deflection, the phases of each beam are optimized through a process of intensity maximization. This is achieved by selecting a reference beam and adjusting the phase of another beam until the intensity at the focus is at its maximum. The beam is then turned off, and the process is repeated for the remaining N-2 beams.

The optical path to implement the procedure is shown in **Figure 4.7a**. A pulsed laser is used for two-photon excitation. Two galvanometric mirrors conjugate with each other, scan the beam along transverse directions. Then, the SLM is conjugated to the back focal plane of the objective. In the detection path, a photomultiplier tube is used as a detector.

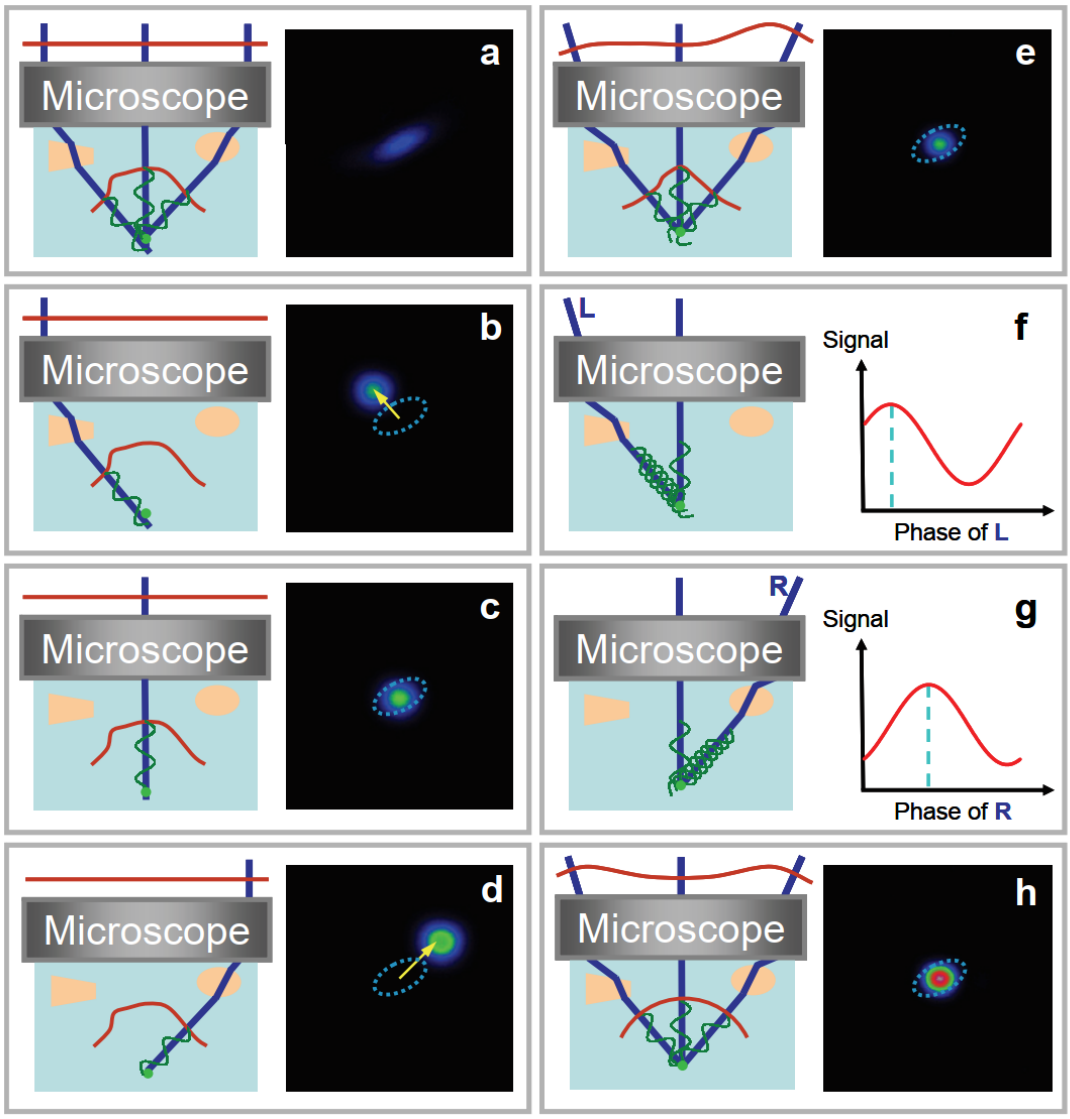

Figure 4.6. Procedure for AO pupil segmentation by Ji et al. (a) *Wavefront (red) is distorted by refractive index inhomogeneities (orange), resulting in an imperfect image of a reference bead* ***(b, c, d).*** *By imaging the left, center, and right subregions, the tilt of each beamlet can be measured from the displacement of the focus.* ***(e)*** *After compensation with the SLM, the beamlets intersect at a common point.* ***(f)*** *The optimal phase offset is determined by interfering the left beamlet with the central reference beamlet at several phase offsets (green sinusoids) and finding the best match (dashed cyan line).* ***(g)*** *The same process is applied to the right beamlet resulting in* ***(h)*** *a final corrected wavefront and a recovered diffraction-limited focus. Reproduced from* [83] *with permission from Springer Nature.*

For the MOSAIC, the SLM is not conjugated to the back pupil because it is not used to correct for aberrations in the sample. Instead, the SLM is conjugated to the sample plane because it is mainly used for producing the lattice structure. Still, the SLM can be used to correct aberrations induced in the optical path.

Flaws in optical components like mirrors can cause imperfection in the excitation lattice. Since many mirrors of the MOSAIC are located close to the pupil plane, the SLM in the sample plane

can be used to correct for the potential aberrations induced by these mirrors using the pupil segmentation algorithm described above. In the context of the MOSAIC, we call this aberration correction the pupil wavefront correction (PWFC). The PWFC in the instrument is shown in **Figure 4.7b**. The path follows the LLS illumination path while imaging is performed using the sample inspection camera. The use of an annular mask with a numerical aperture of 0.600/0.200 is implemented to block the undiffracted beam from the SLM and effectively map the numerical aperture region of an annulus.

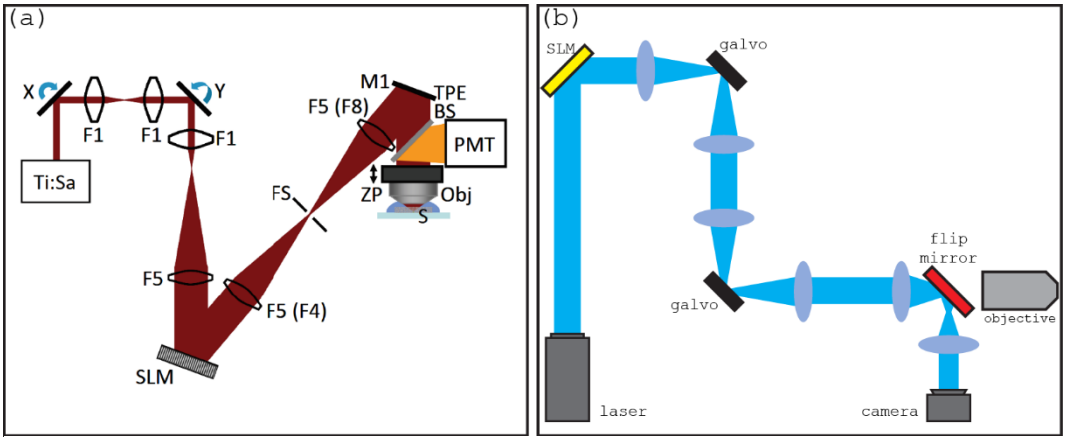

Figure 4.7. Optical path of the pupil segmentation ***(a)*** *Optical path for aberration correction by Ji et al.* [83]. ***(b)*** *Optical path for aberration correction in the excitation light path of the MOSAIC. In* ***(a)****, the SLM is conjugated to the sample plane while in the MOSAIC it is conjugated to the back focal plane of the objective.* ***(a)*** *is reproduced from* [83] *with permission from Springer Nature.*

The result of the PWFC, in **Figure 4.8**. This result demonstrates a noticeable improvement after application of PWFC routine. Notably, the PWFC routine increased the intensity of the central spot and improved the symmetry of the rings, particularly the first ring. It is important to note that if the initial Bessel beam is already symmetric (due to a proper alignment and absence of system-induced aberrations), then the PWFC routine will not have a significant impact, or may even slightly degrade the beam quality. In **Figure 4.8c**, the initial Bessel beam is already symmetric and the central spot has a good intensity modulation compared to the rings. As expected, application of the PWFC routine, as shown in **Figure 4.8d**, result in minimal changes. In fact, the lattice pattern shown in **Figure 4.1** is generated without PWFC. The PWFC routine requires stable beams without much optical drift. I observed that it is helpful to put the enclosure on when using the PWFC routine. The enclosure is a custom-made box for the MOSAIC microscope.

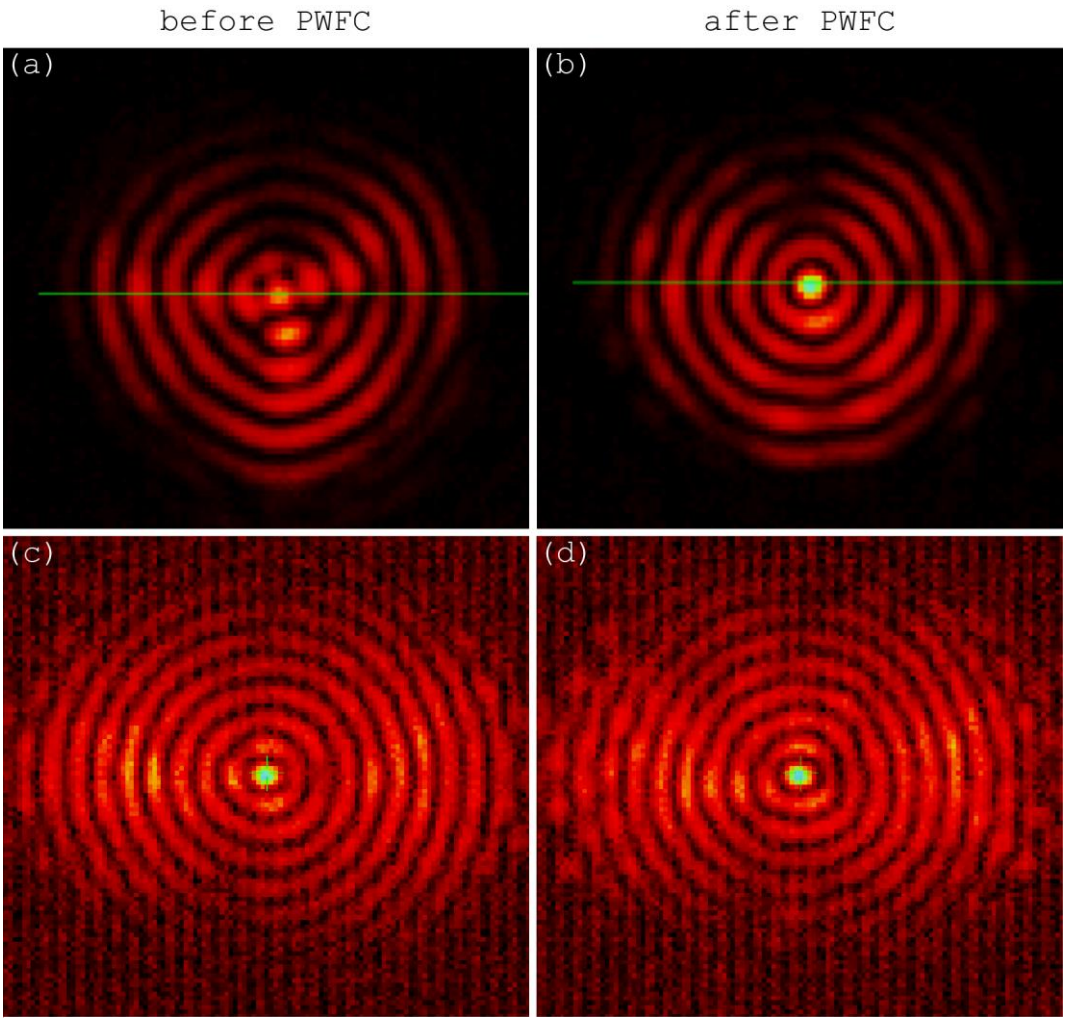

Figure 4.8. Pupil wavefront correction. (a) *Aberrated Bessel beam.* ***(b)*** *Bessel beam after pupil wavefront correction. The corrected beam is more symmetric.* ***(c)*** *An initially symmetric beam shows* ***(d)*** *minimal improvement with PWFC.* ***(a)*** *and* ***(b)*** *are reproduced from the MOSAIC guide by Dan Milkie. The vertical stripes in* ***(c)*** *and* ***(d)*** *results from cropping the camera FOV.*

4.2.3 Phase retrieval

The methods described above ensure that the excitation path is optimized and calibrated. In this section, I discuss how I optimized the detection path.

The optimization of the detection path was achieved by using a phase retrieval algorithm. A deformable mirror was used to correct the phase distortions in the wavefront. The use of a deformable mirror instead of an SLM in the detection path is preferred as the deformable mirror allows a higher photon collection efficiency (i.e., less loss of fluorescence signal). This is

because SLMs have a lower fill factor, meaning that a portion of the photons collected by the detection objective never make it to the detector, while the deformable mirror is a continuous reflective membrane that reflect almost all photons toward the detector. Although the DM has fewer actuators than the SLM has pixels, higher reflection efficiency is prioritized over the resolution of the correction device, especially in the detection path.

The direct measurement of phase is challenging as we can only measure intensity directly. This loss of phase information when making a measurement is called the "phase problem". To overcome this challenge and determine the wavefront aberration in the detection path, we use a phase retrieval algorithm developed by Hanser *et al.* [82]. This algorithm is based on the Gerchberg-Saxton (GS) algorithm.

The GS algorithm shown in **Figure 4.9** is an iterative method to extract phase information of light using two intensity measurements. The two intensity measurements are usually Fourier conjugates of each other. The problem is posed as follows: Given that we only know the intensity at $x = 0$ (source position) and the intensity at another position $x = F$, can we deduce the phase? The GS solution to this is to impose a 'guess' initial field at the source. The phase of the guess field can be anything (usually it is set to random or a flat phase) while the intensity of the guess field is the measured intensity at the source coordinates. Then, the guess field is computationally propagated to the position F. This is done by applying a propagator function to the source field, but if position F is at the Fourier plane, then the computation simplifies to a Fourier transform. This gives a computed phase and computed intensity at position F. The computed intensity at F will not be the same as the measured intensity at F. So, we change the computed field at F to have the same intensity as the measured intensity while keeping the computed phase. This field is then Fourier transformed back to the source coordinates. Again, the computed intensity will not be the same as the measured intensity at the source. So, the measured intensity at the source position is imposed while keeping the computed phase. The resulting field will be the new guess field and the algorithm is repeated until the error between the measured intensities and the calculated intensities converges.

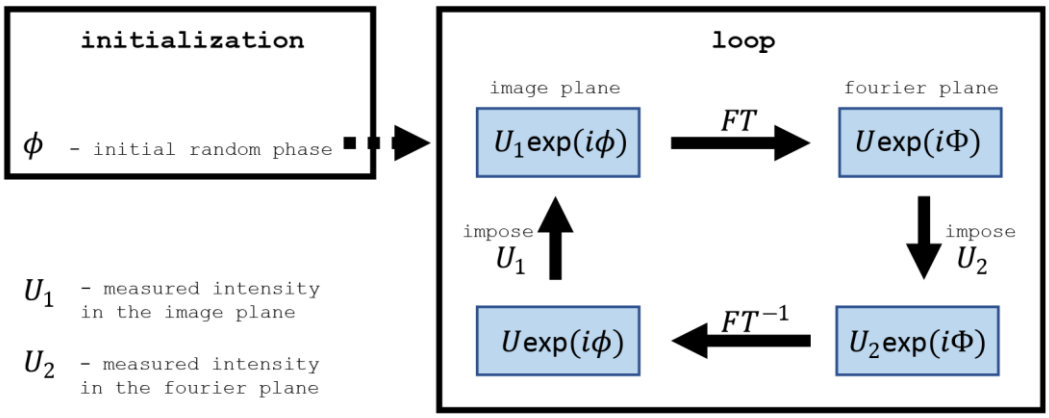

Figure 4.9. GS algorithm. *The GS algorithm is an iterative algorithm for determining the phase of light based on two recorded intensity measurements.*

The phase retrieval implemented for the MOSAIC follows from Hanser *et al.* [82] which is a modification of the GS algorithm. The schematic for the algorithm is shown in **Figure 4.10**. The measured intensities come from the cross section of the PSF at different axial positions *z* = -3, -1, +1, +3 µm. Like the GS algorithm, it starts with a guess function. Here, the guess function is a flat phase with an intensity of unity over the support (defined by the objective NA) of the objective back aperture and zero elsewhere. Then, a defocus that corresponds to the different *z* positions is applied to the guess function. This results in four different functions, called pupil functions, with different defocus. These four pupil functions are each Fourier transformed to obtain a complex-valued PSF at the different *z* positions. The phase of the computed complex-valued PSF is kept, while computed intensities are replaced by the intensities from the measured PSF. The complex-valued PSFs are refocused and then averaged. This averaged PSF becomes the updated guess function, and the algorithm is iterated until the error between the measured intensities and the calculated intensities converges.

In practice, I used 0.1 µm beads as point sources to image the PSF. The beads were glued to the coverglass following **10.2 Bead gluing protocol** in the **Appendix**. The imaging medium used was composed of FluoroBrite DMEM with 1 % PS (penicillin-streptomycin), 1 % Glutamax, 20 mM HEPES (4-(2-hydroxyethyl)-1-piperazineethanesulfonic acid) and was performed at 37 ºC to match the refractive index of the later live cell studies. To generate the PSF, the bead was translated 10 µm axially with in steps of 0.1 µm. From the resulting images of the PSF, the modified GS algorithm detailed above was applied. The negative of the obtained wavefront is applied to the DM.

Experiment II: Optimizing the LLS

An important consideration is that for the phase retrieval algorithm, a widefield illumination is assumed. There are two ways to implement a widefield illumination in the MOSAIC. The first option is to use the SIM excitation path with all the SLM pixels in the ON state. This is originally how the algorithm is intended to be applied in the MOSAIC. However, following discussions with our collaborators in Boston, we found another approach to simulate a widefield excitation using the LLS excitation instead. A widefield illumination was simulated by LLS excitation by scanning the x and z galvanometric mirrors to follow the bead as the stage is moving, meaning that the galvanometric mirrors were also scanned to sweep the light-sheet 10 µm laterally in steps of 0.1 µm, effectively keeping the bead exposed in the same way at all imaging positions.

The PSFs before and after phase retrieval-based aberration correction are shown in **Figure 4.11a-b**. Here, widefield excitation is simulated by letting the light-sheet follow the bead, as the bead moves up during the xz PSF acquisition. Prior to aberration correction, the xz PSF is aberrated with what seems to be coma-aberration since the PSF seems to be curving. With the correction, the aberration is reduced which results in a more symmetric PSF. Finally, the PSF of the square lattice is shown in **Figure 4.11c**. Compared to the widefield PSF (1.45 µm FWHM), the imaging PSF of with lattice light-sheet illumination (0.74 µm FWHM) is more localized in the axial direction which is an indication of better optical sectioning.

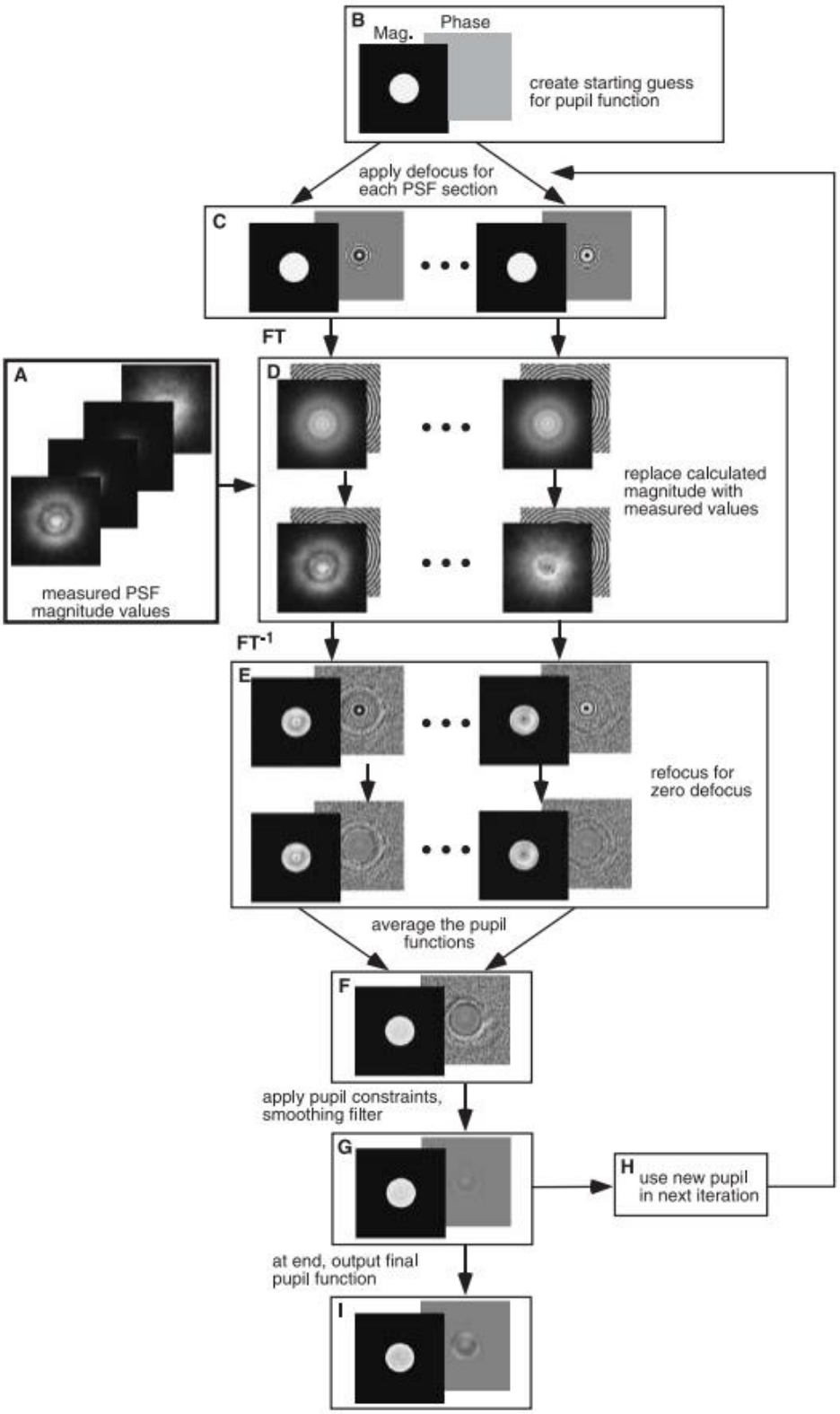

Figure 4.10. Schematic for phase retrieval algorithm by Hanser et al. *Reproduced from* [82] *with permission from John Wiley and Sons.*

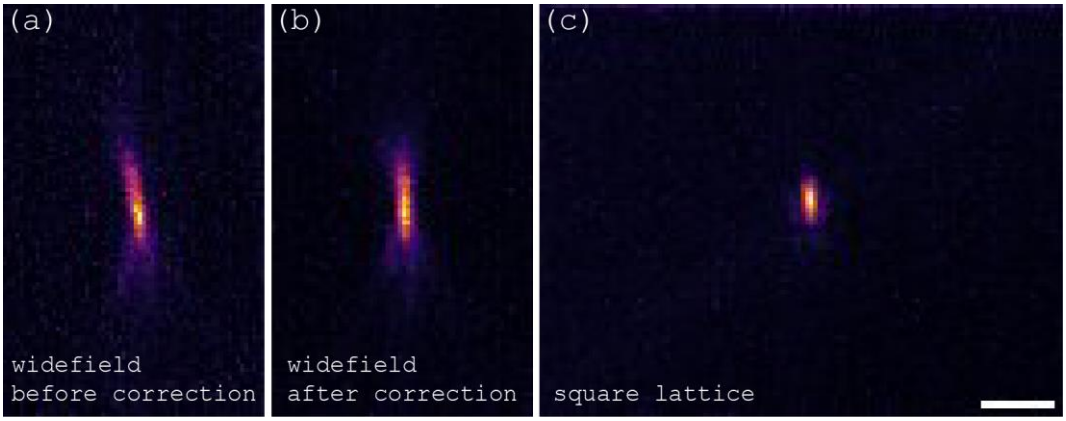

***Figure 4.11. PSFs with phase retrieval aberration correction**. **(a)** Widefield xz PSF without the phase retrieval correction. The PSF is aberrated with what seems to be a coma-aberration. **(b)** Widefield imaging PSF with the phase retrieval correction which resulted in a more symmetric PSF. **(c)** The PSF for a square lattice with a more localized PSF than the widefield case, indicating better optical sectioning. The scale bar is 2 µm.*

4.3 Optimizing for live sample imaging

The calibration methods detailed above ensured that the optical system was optimized. The correction of the intensity profile of the excitation beam and the detection PSF have been performed and imaging of fixed beads with the microscope was also achieved. With the goal of imaging of living biological specimens, steps were taken to optimize the environmental conditions in the sample chamber of the MOSAIC. I outline these steps below. First, I describe the design of the sample holder and chamber, which is crucial in determining the geometric limitations of samples that can be imaged using the instrument. Additionally, I elaborate on the environmental controls implemented in the sample chamber, including temperature control, CO_2 regulation, and evaporation compensation.

4.3.1 The sample chamber and sample holder

The sample chamber, depicted in **Figure 4.12a**, is designed as a rectangular basin with inner dimensions of 6.4 cm × 7.5 cm × 1.3 cm. It is mounted on a stage which can move up/down by a distance of 12 mm. When the stage is in the lowered position, the sample chamber can be extracted like a drawer, providing access for the user to mount the sample. When the stage is elevated, the objectives are immersed in the medium, ready for imaging. Special care should

be taken when pulling the sample chamber out. If the chamber is pulled out while it is in the elevated position, it will hit the tips of the objectives. This can affect the alignment or even damage the objectives.

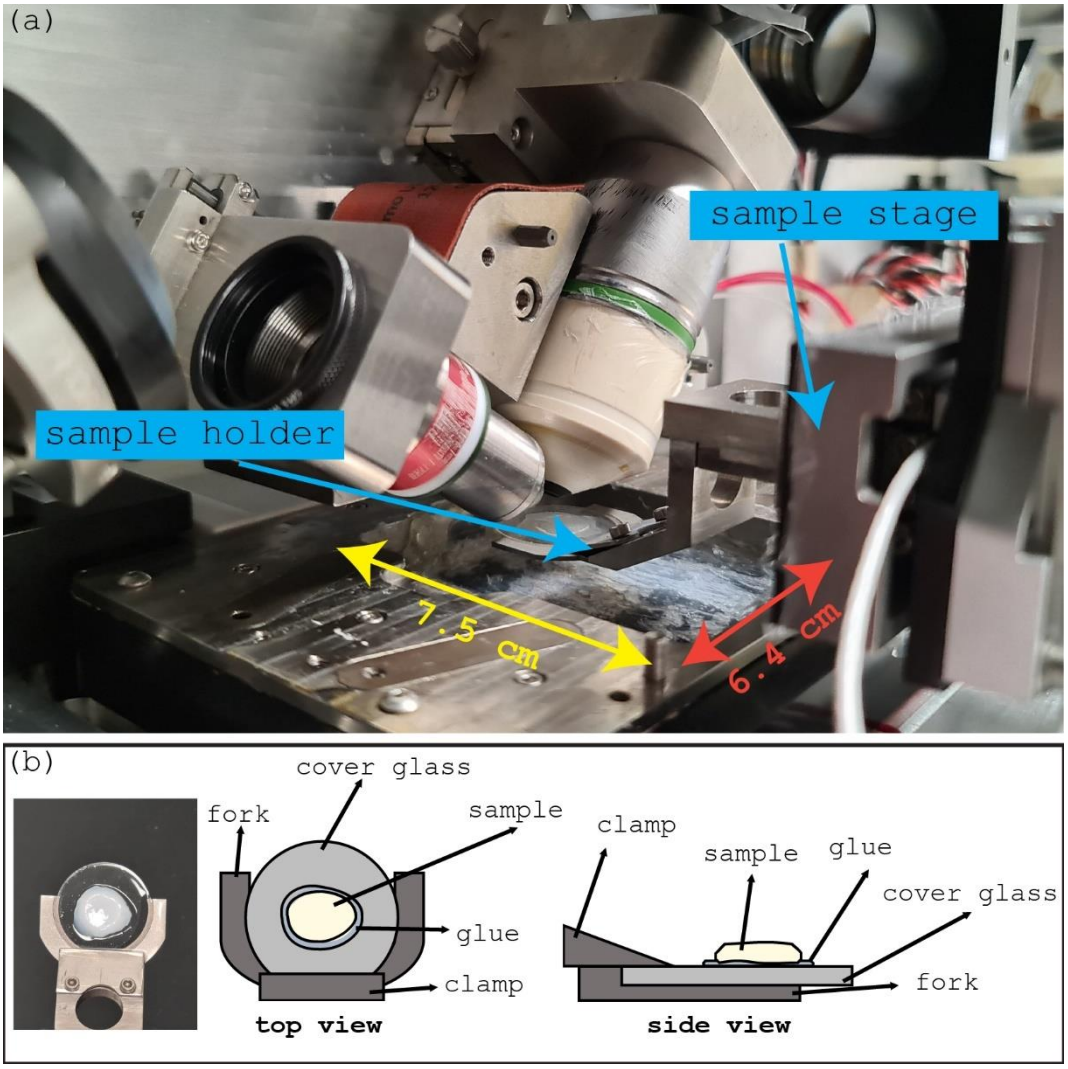

***Figure 4.12. Sample chamber and sample holder**. **(a)** The sample chamber is a rectangular basin that can move up and down to submerge the objectives. **(b)** A custom-made fork clamps the cover glass where the sample is attached. The fork can then be mounted to a 3D stage via magnets.*

The coverglass is held by a custom-made "fork" as shown in **Figure 4.12b**. The fork is attached with magnets to a 3D sample stage. The sample stage is independent of the sample chamber movement. The objectives, the stages, and the fork define a constraint to the size of the sample that can be imaged using the instrument (shown in **Figure 4.13**).

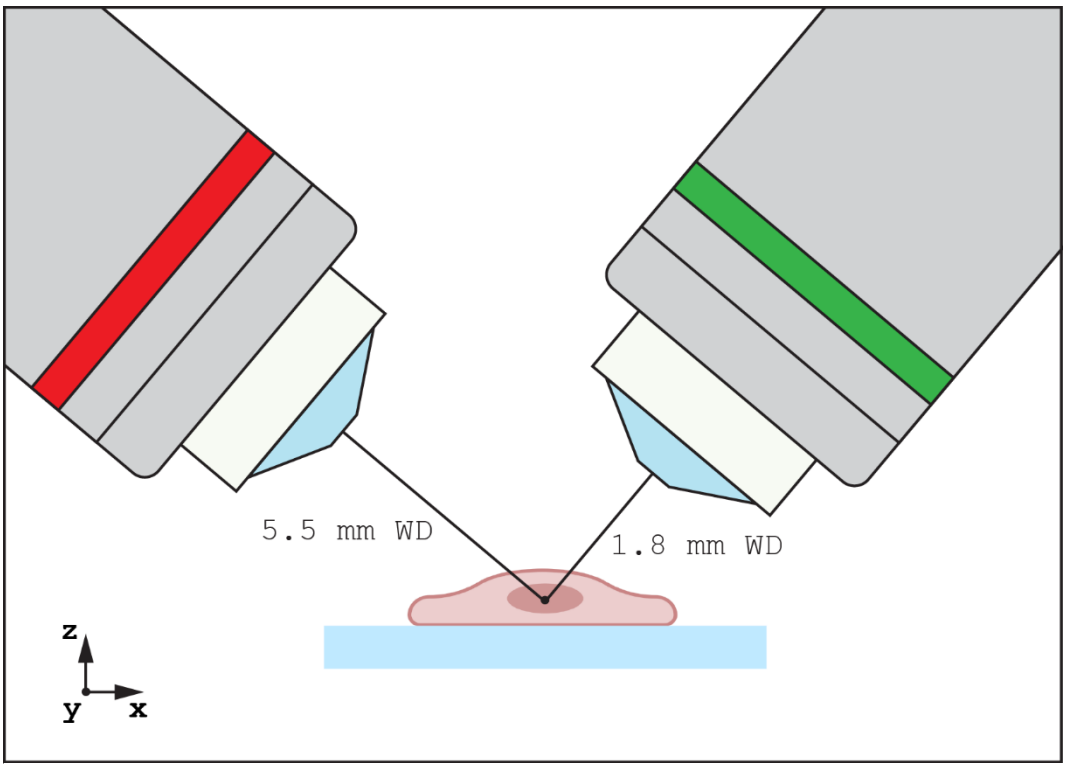

Figure 4.13. Constraint to sample size and sample mounting*. The working distances (WD) of the excitation objective and detection objective, as well as the position of the coverglass, limits the size of the sample that can be mounted.*

4.3.2 Environmental controls

The sample chamber is equipped with environmental controls to regulate temperature, CO_2 supply, and evaporation as shown in **Figure 4.14**.

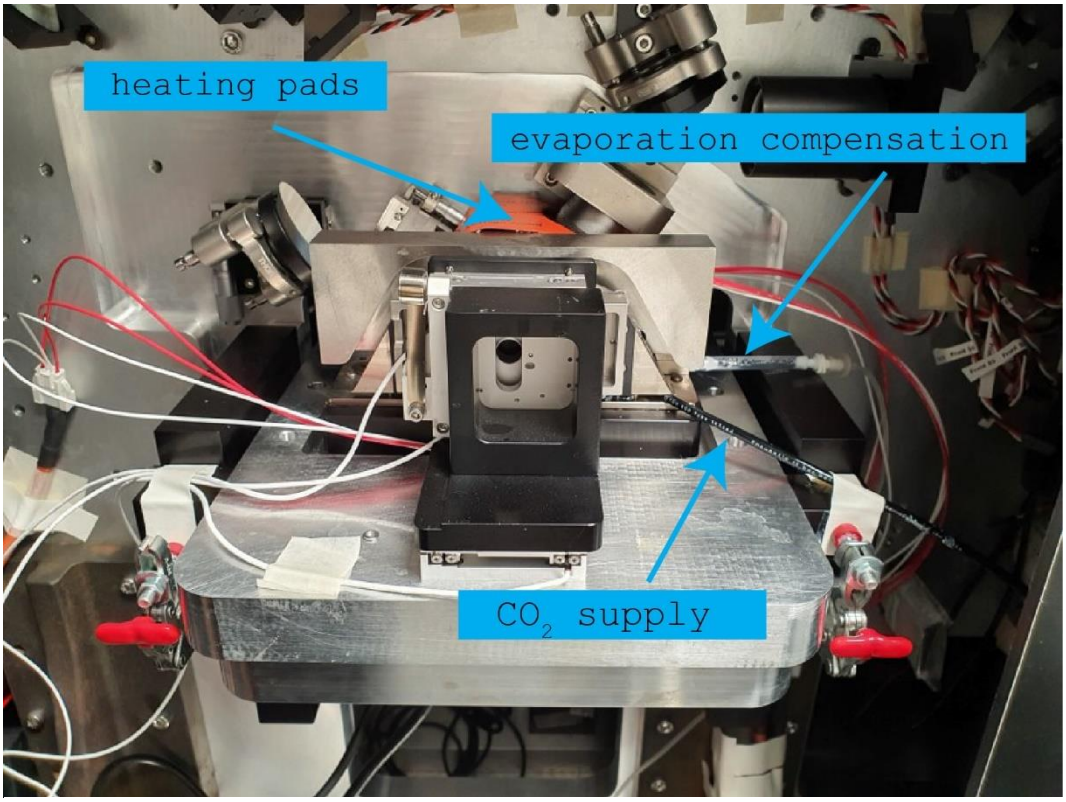

Figure 4.14. Environmental control. *The sample chamber is equipped with temperature control, and tubing for CO_2 supply and evaporation compensation.*

Three heating pads surround the sample chamber. One of the heating pads is attached directly to the bottom of the sample chamber. The two other pads are located above the chamber, one behind and one in front of the objectives. The temperature of each pad can be set using the temperature controller outside of the enclosure. A steady supply of 5 % CO_2 flows into the sample chamber via the black tube coming in from the right side. Lastly, the evaporation is compensated by a continuous supply of Milli-Q water, since the dissolved compounds are assumed not to evaporate. The evaporation rate was measured from the change in the absorbance of an added food dye, quinoline yellow, in the sample chamber over 4 hours. Every hour 0.5 mL of the solution was extracted, and its absorbance was measured. **Figure 4.15** shows the amount of liquid in the sample chamber over time calculated by measuring the absorbance over time normalized to the initial absorbance of the non-volatile water-soluble dye, and then taking the reciprocal to get the relative amount of remaining liquid. From the slope of the best fit line, the evaporation loss was measured to be 1.5 mL/h.

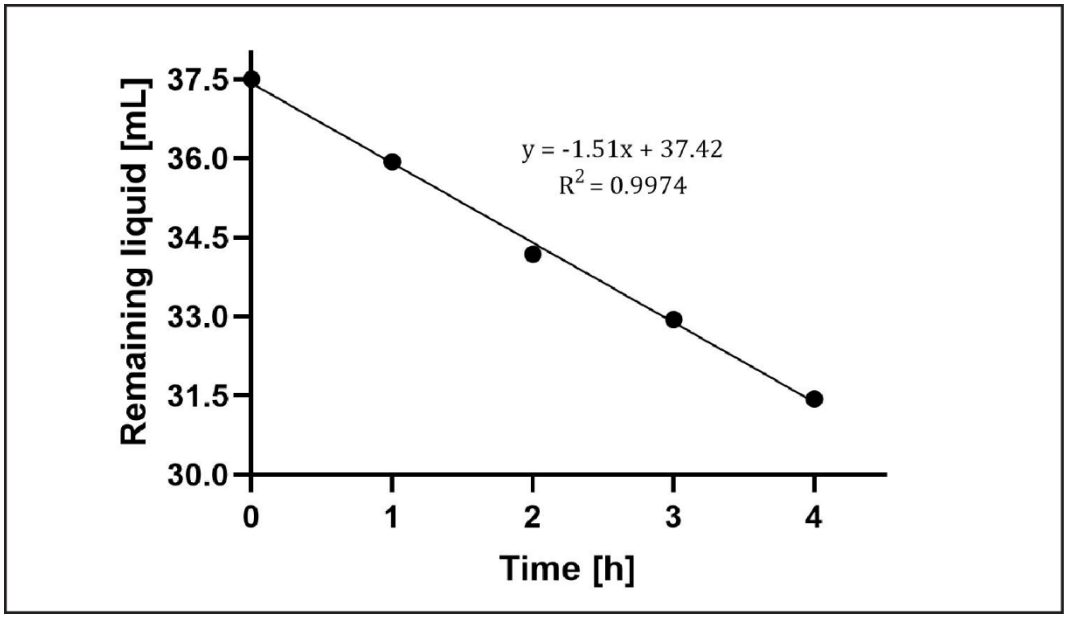

Figure 4.15. Evaporation rate. *From the absorbance of quinoline yellow, the evaporation rate in the sample chamber of the LLS was measured to be 1.5 mL/h.*

4.4 Discussion

The design of the LLS optical path in the MOSAIC is complex due to the presence of other imaging modes that share components with the LLS optical path. This complexity can lead to an increase in optical aberrations. To mitigate these aberrations, I carried out optimization protocols that included calibrating the SLM to achieve uniformity in the excitation beam as well as correcting system aberrations in both the excitation and detection paths using PWFC and phase retrieval algorithms, respectively. Moreover, I optimized the LLS for imaging live samples by incorporating temperature, CO_2, and evaporation controls in the sample chamber. It was noted that, if the paths are already well aligned, these optimizations may not result in significant improvement as in the case of the PWFC. Thus, I have decided not to routinely apply PWFC as the excitation beam is nearly optimal.

It is essential to consider that the PWFC, based on the inspection camera, includes aberration compensation in the inspection path that may not be present in the LLS optical path. Moreover, the PWFC does not correct for any aberrations occurring in the excitation objective or the mirror located immediately before it. Therefore, it is crucial to verify that the mirror immediately before the excitation objective and the mirrors in the inspection path do not exhibit any aberrations.

Other imaging modes were necessary to align as they are critical in some optimization techniques. For example, the SIM path is necessary for the SLM calibration. The SIM path was also originally intended to simulate a widefield illumination for the phase retrieval algorithm. However, an alternative method to simulate a widefield illumination using the LLS path was implemented after discussions with our collaborators in Boston.

It is worth mentioning that the instrument also has the capability to correct for sample-induced aberrations using the deformable mirror, although this function is currently not operational, as we have not yet implemented the two-photon laser necessary to evoke a ‘guide-star fluorescence signal’ inside the sample.

Chapter 5. Experiment III: Imaging with the LLS

5.1 Introduction

In this chapter, I discuss the imaging experiments performed using the LLS. The chapter is structured into five sections. The introduction provides an overview of the imaging parameters used for the different experiments. The following three sections present a detailed analysis of the imaging procedures and results obtained from imaging three distinct samples. Finally, a discussion section concludes this chapter by highlighting the key insights gained from the imaging experiments.

The first sample we imaged is a 2D monoculture of cells genetically modified to express AP2, a key protein of clathrin-mediated endocytosis, tagged with enhanced green fluorescent protein (eGFP). This sample has been well-characterized by our collaborator and serves as a reference point for the performance of the LLS. The main objectives of this experiment were to confirm the sustained viability of samples within the sample chamber and to check the compatibility of the dyes that we plan to use in the other experiments. The second sample is a CRISPR/Cas9 modified 2D skin culture. The aim was to observe morphological changes in the mutant sample compared to a wild type sample, specifically focusing on the formation of lamellar bodies in the mutant culture. The third sample is a 3D organotypic skin model (OSM), which consists of multiple cell types grown in a transwell. The focus of this experiment was to track the behavior and migration of T-cells in different strata of the skin over time.

The imaging parameters used in these different experiments were optimized to suit the specific samples and the desired observations. Below I provide an explanation of the key parameters:

- **Number of stacks:** A stack is a 3D volume consisting of multiple 2D images. The number of stacks determines the number of 3D volumes over time.
- **Number of images per stack:** This determines how many 2D images are captured to form a single 3D stack.
- **Step size:** This is the distance that the sample stage moves after taking an image in a stack.
- **Stage movement range:** The range is the total stage movement after taking all the images in a stack. In my experiments, the sample stage movement was either along the horizontal

direction (*x*-axis) or along the optical axis of the detection objective (*xz*-axis). The step size, stage movement range, and the total number of images are not independent. Choosing a value for any two of the parameters imposes the value of the third parameter.

- **Exposure:** is the requested sensor collection time on the camera. A longer exposure time leads a longer illumination time and a brighter image. However, the tradeoff is a low time resolution and a higher rate of photobleaching and phototoxicity.
- **Stack capture time:** The total amount of time to capture a single stack. Stack capture time, exposure, and the number of images per stack are not independent. Choosing a value for any two of the parameters imposes the value of the third parameter.
- **Rest between stacks**: The time delay between when each 3D stack is captured. It sets the time interval of a 4D acquisition (3D + time).
- **Total acquisition time for all stacks:** The overall time it takes to capture a 4D acquisition.
- **Power:** The laser power imparted on the sample. Higher power yields more fluorescence, until the fluorescence process is saturated. It also leads to greater phototoxicity and faster photobleaching.
- **Channels:** The number of different colors we wish to probe in the sample. This can be considered the 5th dimension. Because the channels are acquired sequentially, additional channels increase the time to capture a stack.
- **Tiling:** is a special parameter used for imaging the 3D OSM. The tiling defines the size of the array of 3D stacks that are stitched to form a single image.

Figure 5.1a-b shows how a stack can be acquired using two possible sample stage movement directions. The acquisition motion can be either along the horizontal (x-axis) or along the axis of the detection objective (xz-axis). For an acquisition along the x-axis, the images need to have an offset before being stacked on top of each other to create the 3D image. Otherwise, the resulting stack will not capture the geometry of the sample (**Figure 5.1c**). While for an acquisition along the xz-axis, the images can simply be stacked on top of each other (**Figure 5.1d**). A pre-processing step called ‘deskewing’ can be applied to an acquisition along the x-axis to recover the correct geometry of the sample (**Figure 5.1e**)

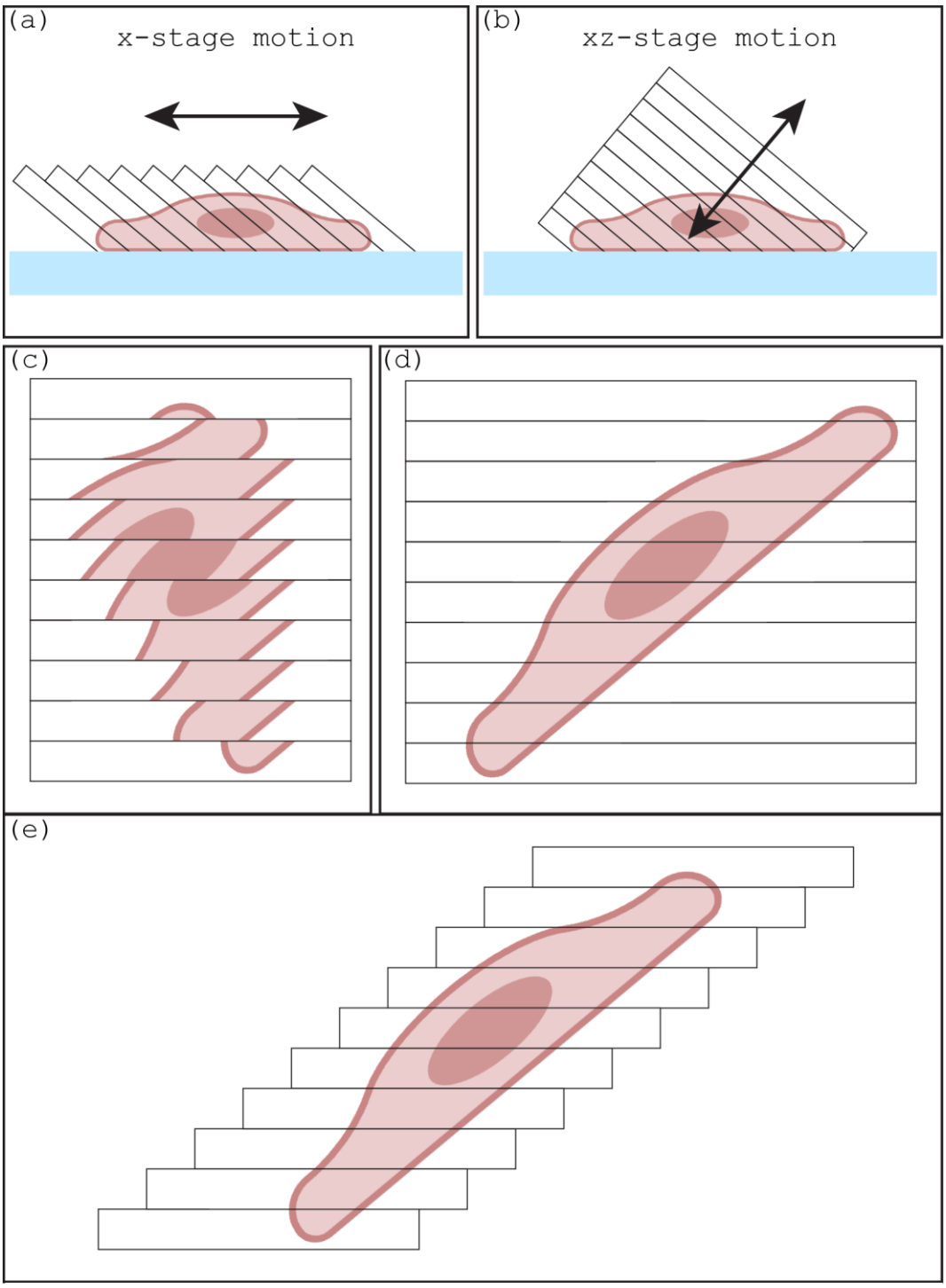

Figure 5.1. Stage motion and deskewing. (a) *Stack composed of images with the sample stage movement along the x-axis.* ***(b)*** *stack composed of images with the sample stage movement along the xz-axis.* ***(c)*** *non-deskewed stack captured with x-stage movement.* ***(d)*** *non-deskewed stack captured with xz-stage movement.* ***(e)*** *deskewed stack captured with x-stage movement.*

5.2 Imaging a test sample

The AP2-eGFP SVGA astrocytic cell lines were a generous gift from T. Kirchhausen. These cells have been genetically modified to express eGFP-tagged activator protein 2 (AP2) promoter. AP2s are adaptor proteins that recruit clathrin and initiate the formation of CCPs (clathrin-coated pits) during clathrin-mediated endocytosis (CME) [84], [85]. The cells were maintained in Dulbecco's Modified Eagle Medium (DMEM) containing 10 % fetal bovine serum (FBS), incubated at 37 ^{o}C and 5 % CO_2 in a humidified incubator.

In this experiment, we aimed to observe the creation and disassembly of CCPs. These CCPs have a size range of 50 to 200 nm, making them suitable diffraction-limited points for the instrument. Additionally, CME is a quick process that can take place within seconds.

The SVGA cells were imaged using the settings in **Table 5.1.** These settings were carefully chosen to provide optimal signal and resolution for visualizing the dynamics of CCP formation and disassembly, while also ensuring that the cells are not obviously subjected to harmful conditions during imaging. This allows us to maintain cell viability for extended periods of time (up to 6 hours) within the sample chamber. The 488 nm excitation laser was used to image the cells in a volume of 50 µm × 110 µm × 38 µm over 4 min.

***Table 5.1**. Imaging settings for the SVGA cells.*

Volume	
number of images per 3D stack	101
number of stacks	38
step size, x-axis, between images	0.5 µm
stage movement range, x-axis	50 µm
Timing	
exposure time per image	40 ms
stack capture time	4 s
rest between stacks	2 s
total acquisition time	4 min
Power	
488 nm	0.09 mW

The images of the SVGA cells from different perspectives are shown in **Figure 5.2**. **Figure 5.2a** is a side view, maximum intensity projection (MIP), where the flat bottom is the coverglass. **Figure 5.2b** is a top view MIP, while **Figure 5.2c** is a slice (one image) of the 3D stack.

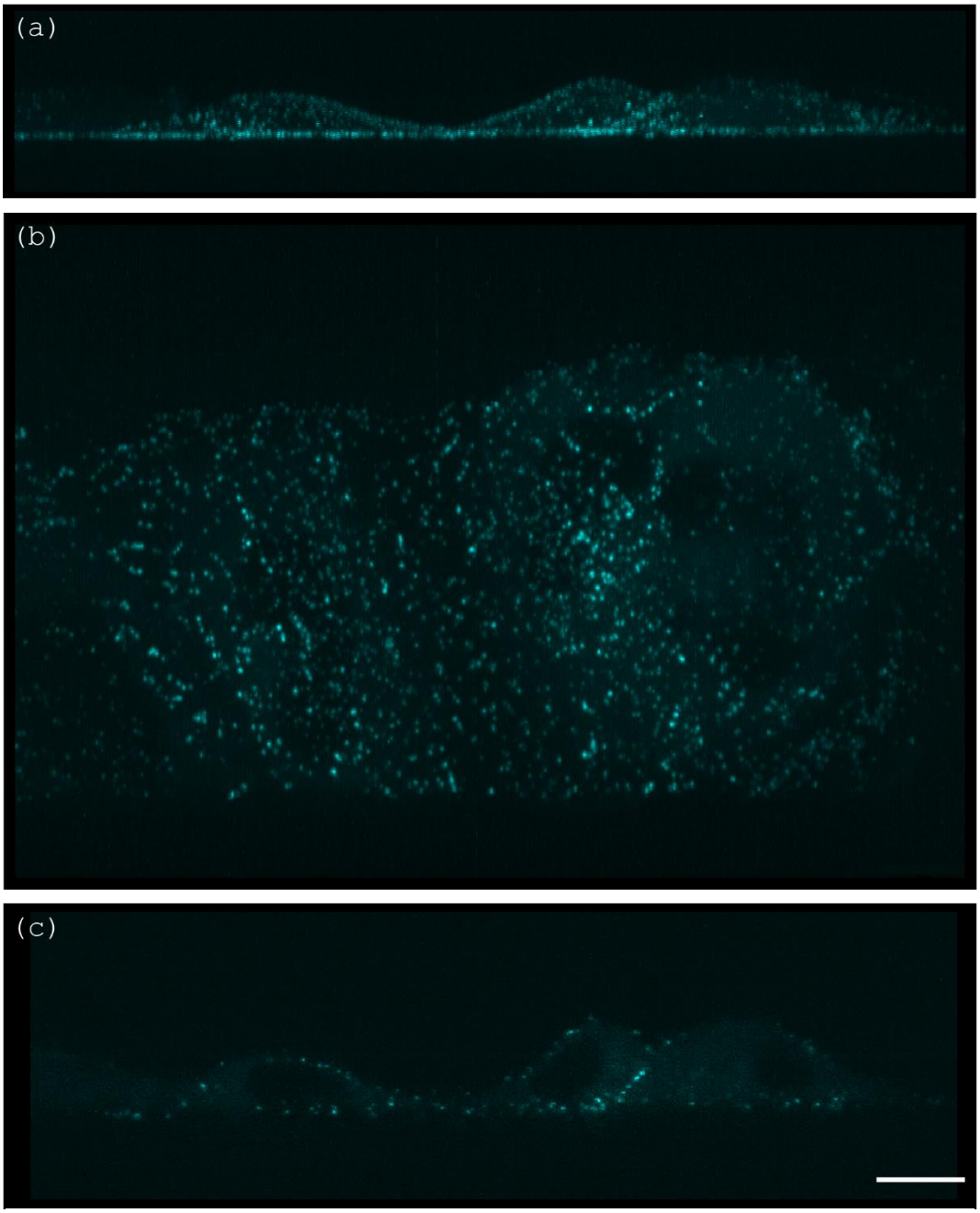

Figure 5.2. SVGA cells expressing eGFP under the AP2 promotor. *Clathrin coated pits appear as diffraction limited spots in the SVGA images.* ***(a)*** *Side-view MIP.* ***(b)*** *Top-view MIP.* ***(c)*** *A single image of the stack. The scalebar is 10 µm.*

I also tried three-color imaging of the SVGA cells by adding LysoTracker™ DnD-99 and CellMask™ Deep Red staining. The excitation and emission spectra of these markers are listed in **Figure 10.1** of the **Appendix**. These makers label lysosomes and plasma membranes, respectively. The imaging settings for this experiment are similar to **Table 5.1** with the addition of two channels: 560 nm excitation for the LysoTracker and 642 nm excitation for the

CellMask, both at 0.05 mW. Additionally, the acquisition time was three times as long as for a single color, since I acquired the channels sequentially. The 560 nm and 642 nm channels were captured on camera B whereas the 488 nm channel was captured on camera A. To gauge the cross-talk between the channels, the three-color imaging was performed on SVGA cells labeled with LysoTracker only, CellMask only, and with both Lysotracker and CellMask. The results of these three-color imaging experiments are shown in **Figure 5.3**.

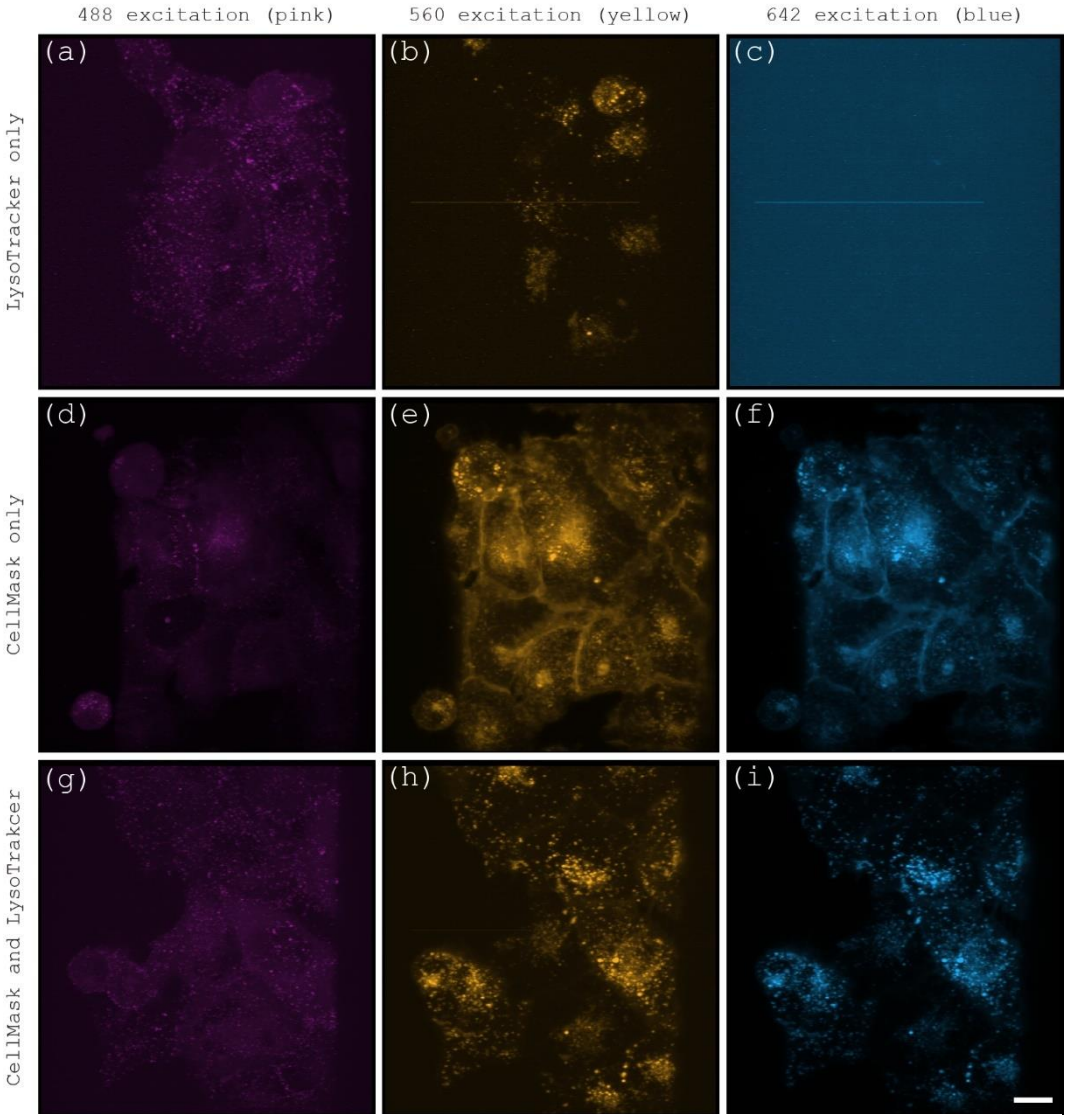

Figure 5.3. Three-color imaging of SVGA cells*. SVGA cells stained with LysoTracker only* ***(a) – (c)*** *shows clear channel separation and no crosstalk between the 488 nm, 560 nm and the 642 nm channels. Cells stained with CellMask only* ***(d) – (f)*** *have significant crosstalk between the 560 nm and the 642 nm channels. Combining both stains* ***(g)-(i)*** *results in expected crosstalk between 560 nm and 642 nm channels, while 488 nm channel remains isolated. The stripe in* ***(b)*** *and* ***(c)*** *is a dead pixel in the camera. The scalebar is 15 µm.*

Experiment III: Imaging with the LLS

For the SVGA cells stained with LysoTracker only, there is a clear separation between the different channels (**Figure 5.3a-c**). For the SVGA cells stained with CellMask only (**Figure 5.3d-f**), the 488 nm channel still shows a clear eGFP signal as expected. However, there seems to be a significant crosstalk between the 560 nm channel and the 642 nm channel excitations because the same structures are observed in both channels. It would have been ideal if the CellMask signal appeared only with 642 nm excitation. However, CellMask is also excited by the 560 nm laser (as shown in the appendix) and the current filter configuration does not allow to effectively distinguish the distinct fluorescence spectra of the two exogenous dyes. We should expect therefore significant crosstalk when using both Lysotracker and CellMask markers. For completeness, I also imaged SVGA cells stained with both Lysotracker and CellMask (**Figure 5.3g-i**). There is a lot of cross talk between the 560 nm and 642 nm channels, whereas the 488 nm channel is well isolated, as expected.

5.3 Imaging a 2D sample of isolated skin cells

The N/TERT-1 immortalized keratinocytes used in the study were sourced from JG Rheinwald's lab at the Harvard Institute of Medicine and Brigham & Women's Hospital and were prepared by our collaborators, Sally Dabelsteen, Fawzi Khoder Agha, and Mikkel Møller Aasted from the University of Copenhagen. These cells were grown in a keratinocyte serum-free medium (Gibco, Thermo Fischer Scientific), which was supplemented with 1.25 mg of bovine pituitary extract per 500 mL medium (Gibco, Thermo Fischer Scientific), 0.2 ng/mL of epidermal growth factor (EGF) (Thermo Fischer Scientific), and $CaCl_2$ (Sigma Aldrich) to a final Ca^{2+} concentration of 0.3 mmol/L.

The MGAT1KO are genetically modified keratinocytes generated using the CRISPR/Cas9 technology. This was accomplished by targeting the MGAT1 exons using validated gRNAs [86] or gRNAs predicted by GPP [87]. The gRNAs were cloned [88] using oligos (TAGC, Denmark) into lentiCRISPR-v2-Puro plasmid backbone (Addgene #52961) or lentiCRISPR-v2-Blast with a blasticidin resistance gene replacing the puromycin resistance gene (Brakebusch laboratory, BRIC, UCPH, DK). Directional cloning and insertion of the gRNA duplex using BsmBI and T4 ligase into the LentiCRISPR-v2 plasmid backbone was done as described in [89].

For the 2D skin sample, we wanted to compare and observe the accumulation of enlarged bodies in MGAT1KO cells. The gene modification disrupts the function of the MGAT1 gene in the cells, which is responsible for encoding the alpha-1,6-mannosylglycoprotein 6-alpha-N-acetylglucosaminyltransferase enzyme. This enzyme is involved in the biosynthesis of complex N-glycans. A knockout of MGAT1 can affect the normal functioning of this biosynthetic pathway, leading to changes in cellular physiology and cellular behavior. The MGAT1KO cells have been studied in various biological systems, including the skin. Studies have shown that MGAT1 abrogates the biosynthesis of all complex N-glycans [90] and MGAT1KO in mice leads to early embryonic lethality [91], [92]. Tissues generated with MGAT1KO formed skin with large lamellar bodies throughout the epithelium [93]. The accumulation of enlarged lamellar bodies in the MGAT1KO cells indicates that there are defects in the secretory pathway associated with N-linked glycans. This change in N-glycan biosynthesis can affect the functioning of the Golgi apparatus and lysosomes, which are key organelles involved in protein modification, sorting, and degradation.

Our first aim was to use live cell probes and mark secretory pathway organelles such as Golgi and lysosomes to observe minute changes and differences between wild type (WT) and MGAT1KO cells. The second aim was to follow the formation of lamellar bodies from the trans-Golgi until it fuses with lysosomes to identify at which location and at what time point fusion defects or accumulation occurs. Two experiments were designed to fulfill the objectives of visualizing lysosomes and Golgi apparatus as well as lamellar bodies. In the first experiment, the skin samples were treated with LysoTracker to visualize lysosomal structures and pHrodo Green staining, to visualize the Golgi apparatus. In the second experiment, pHrodo staining and Ceramide staining were used to label and visualize the lamellar bodies.

The sample was imaged using the settings in **Table 5.2**. The excitation lasers 488 nm and 560 nm were used to image the cells in a volume of 100 µm × 130 µm × 38 µm over 1 h.

Experiment III: Imaging with the LLS

Table 5.2. 2D skin sample imaging settings

Volume	
number of images per 3D stack	101
number of stacks	396
step size, x-axis, between images	1 µm
stage movement range, x-axis	100 µm
Timing	
exposure time per image	40 ms
stack capture time	4 s
rest between stacks	1.5 s
total acquistion time	1 h
Power	
488 nm	0.09 mW
560 nm	0.05 mW

Figure 5.4 illustrates the keratinocytes stained with LysoTracker and pHrodo. The MGAT1KO (**Figure 5.4d-f**) cells are characterized by the presence of large potential lamellar bodies. Normally, lamellar bodies are specialized organelles in the skin that help maintain skin hydration and barrier function. The lamellar bodies are composed of a combination of lipids and proteins.

The main challenges encountered during this experiment were due to the limitations imposed by fluorescence bleaching and cell death. After one hour of continuous imaging, the signal was too weak to observe secretory pathway changes and maturation of potential lamellar bodies.

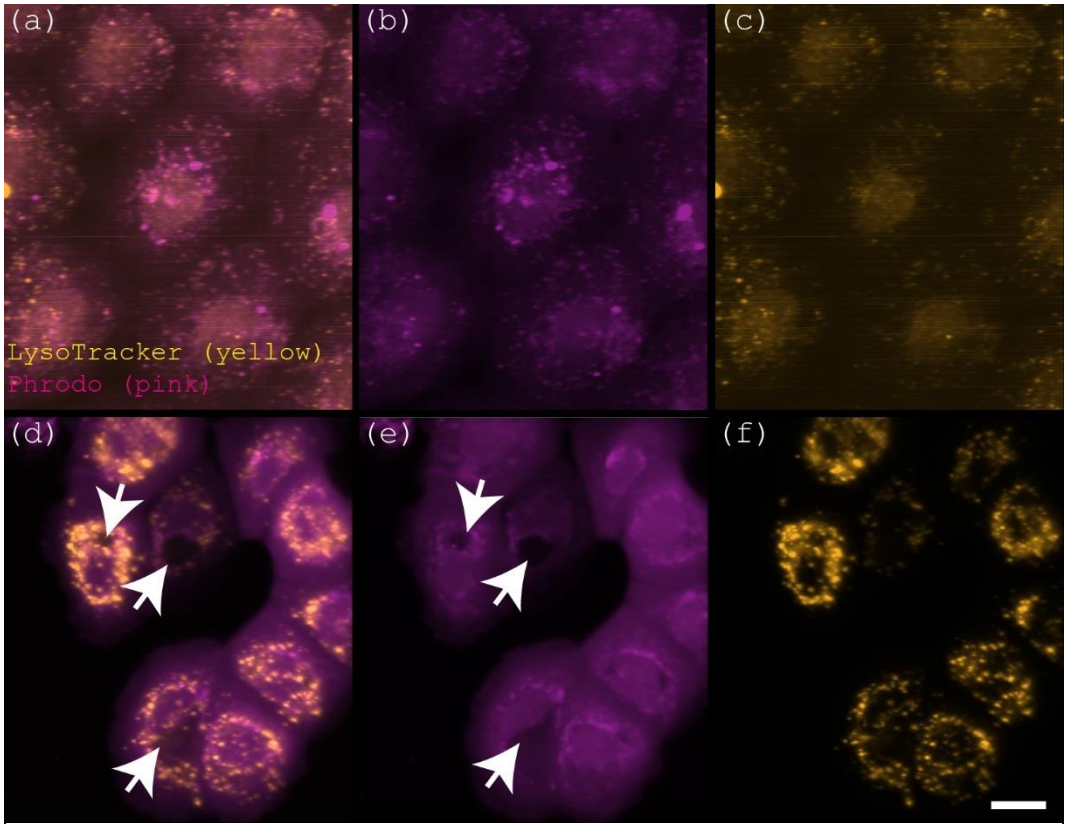

Figure 5.4. Potential lamellar bodies in MGAT1KO cells compared to wild type cells. *The cells were stained with LysoTracker (yellow) and pHrodo (pink).* ***(a)-(c)*** *Wild type keratinocytes and* ***(d)-(f)*** *MGAT1KO keratinocytes show phenotypical differences. The MGAT1KO cells are characterized by the presence of large lamellar bodies as pointed by the arrows. The scale bar is 10 µm.*

Figure 5.5 depicts the MGAT1KO cells stained with pHrodo and Ceramide. As previously noted, the presence of giant lamellar bodies is apparent (**Figure 5.5b**). Interestingly, the ceramide stain did not label the lamellar bodies (**Figure 5.5c**). However, a lamellar body was observed to become stained with pHrodo over time (encircled in **Figure 5.5b**). **Figure 5.6** illustrates this observation. Initially, at t = 0 (**Figure 5.6a,e,c**), the lamellar body was not stained with either ceramide or pHrodo. After one hour (**Figure 5.6b,d,f**), pHrodo accumulated inside the lamellar body but not the ceramide. This absence of ceramide accumulation within the giant lamellar bodies in MGAT1KO cells suggests a discrepancy in lipid composition compared to expectations.

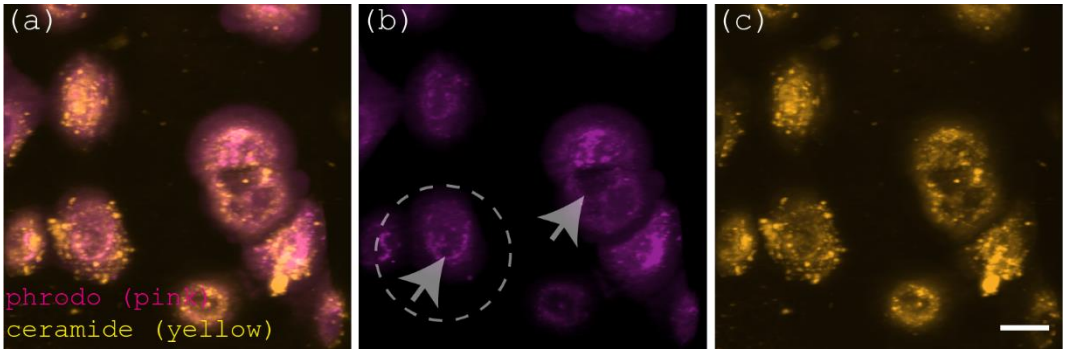

Figure 5.5. PHrodo and Ceramide staining of MGAT1KO cells. (a) *MGAT1KO cells stained with pHrodo and Ceramide.* ***(b)*** *The pHrodo channel.* ***(c)*** *The ceramide channel. The presence of giant lamellar bodies is indicated by arrows in* ***(b)****. The lamellar body in the encircled cell became stained with pHrodo over time. Ceramide did not label the lamellar bodies. The scale bar is 15 µm.*

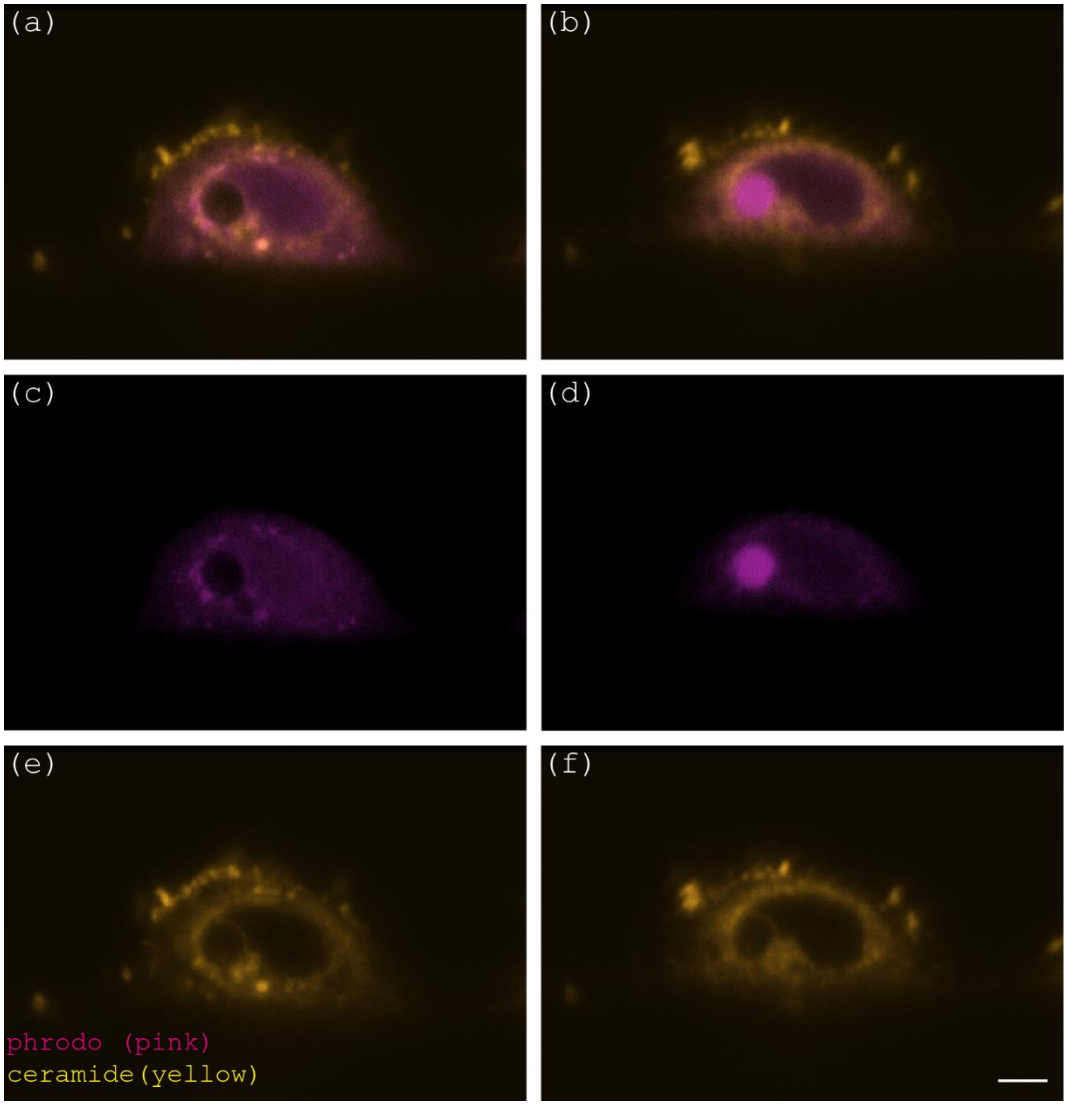

Figure 5.6. PHrodo inside the lamellar body of MGAT1KO cell*. The lamellar body was observed to be stained with pHrodo over time.* ***(a)****,****(c)*** *and* ***(e)*** *are images at t = 0, while* ***(b)****,* ***(d)*** *and* ***(f)*** *are images at t = 1 h. Initially, the lamellar bodies were not stained with either ceramide nor pHrodo. After one hour, the same lamellar body was filled with pHrodo but remained unstained with ceramide. The scale bar is 5 µm.*

5.4 Imaging a 3D organotypic model of skin

We imaged the 3D transwell organotypic skin model developed by Dabelsteen *et al*. [93]–[95]. Here, we wanted to observe how T cells migrate in a living 3D OSM. First, we aimed to determine if we can probe the T cells without slicing or destroying the skin barrier underneath the skin by imaging from the top layers of the skin. Second, we wanted to determine how fast they move and if there is a directionality to their movement.

Dabelsteen's 3D organotypic skin model involves the preparation of two types of hydrogels: an acellular gel and a cellular gel [94]. The acellular gel is prepared by mixing the following components in a 50 mL tube: 650 µL 10X MEM with Earle's salts, 70 µL L-glutamine (100x stock of 200 mM), 10 µL gentamicin sulfate (40 mg/mL), 725 µL fetal calf serum, 725 µL sodium bicarbonate (71.2 mg/mL), 5.5 mL rat tail collagen (4 mg/mL in 0.05 % acetic acid), and 850 µL 10 % calf serum DMEM. The pH is then neutralized with a few drops of 1 M NaOH and carefully pipetted into the wells of a six-well deepwell plate, which contains a cell culture insert in each well. The acellular gel is then allowed to polymerize in the incubator. The cellular gel is prepared by mixing the following components in a 50 mL tube: 1.7 mL 10X MEM with Earle's salts (without L-glutamine or sodium bicarbonate), 170 µL L-glutamine (100x stock of 200 mM), 25 µL gentamicin sulfate (40 mg/mL), 1.9 mL fetal calf serum, 525 µL sodium bicarbonate (71.2 mg/mL), 14.4 mL rat tail collagen (4 mg/mL in 0.05 % acetic acid), 850 µL 10 % calf serum DMEM, and 2.1 mL human fibroblasts suspended in 10 % calf serum DMEM, 1 x 10^5 GFP expressing human Jurkat T cells and 20 ng/mL interleukin-2. The mixture is then neutralized with a few drops of 1 M NaOH and quickly pipetted on top of the acellular gel to avoid creating air bubbles. The gel is then allowed to polymerize for approximately 30 minutes in the incubator. Lastly, the well is filled with DMEM containing 10 % FCS (18 mL) and an additional 2 mL was added on top of the gel.

After 4-6 days, the gels will have contracted and formed a slightly shrunken, white disk-like structure. This macroscopic change is the result of successful and reproducible deposition and reorganization of the extracellular matrix (ECM) by the fibroblasts, which is necessary for the formation of a functional *in vitro* tissue model.

Next, the keratinocytes are seeded on the gel. First, N/TERT-1 cells are trypsinized and the concentration is adjusted to 1.3 x 10^7 cells/mL. 3 x 10^5 cells need to be plated for each gel. Then, the medium is aspirated from the bottom of each well and the medium from the culture insert is removed. A cell suspension of 30 µL is then added to the center of the gel, in the concave area of the shrunken gel. The bottom of each well is then filled with 9 mL of organoid culture medium until it reaches the bottom of the culture insert. The gels are then incubated at 37 °C for 20 minutes to allow the cells to adhere. Then, 2 mL of organoid culture medium is carefully added on top of the adhered cells and the plates are placed in an incubator. Finally, the gels are incubated for 4 days before lifting. Specifically, on day 4 after keratinocyte seeding,

the culture medium is aspirated from the culture insert and plate wells. The insert is then transferred to a sterile 100 mm dish using sterile forceps. Two sterile airlift pads are added to the base of each well plate and the insert is placed back into the well over the pads. The plate is then incubated at 37°C in a humidified incubator and the medium in the deep wells are changed every other day. The gels are ready to be harvested in 10 days, and the models remain stable for up to three weeks.

I imaged the 3D OSM on day 1 and day 7 after the incubation period. We added CellMask Deep Red membrane staining to label the top layer of the skin. The imaging settings are found in **Table 5.3**. On day 1, I imaged a region of 240 µm × 70 µm × 400 µm over 15 min every 20 s. This area is composed of 2 × 2 tiling with 20 % overlap. Then, I focused on a smaller region and imaged that region for 1 hour every 20 s. On day 7, I imaged a larger region of 225 µm × 190 µm × 400 µm with a tiling of 6 × 3 with 20 % overlap for 6 hours every 7 min.

Table 5.3. *Imaging settings for the 3D OSM.*

Volume	**Day 1**	**Day 7**
number of images per 3D stack	201	201
number of stacks	10	324
step size, x-axis, between images	2 µm	2 µm
stage movement range, xz-axis	400 µm	400 µm
Tiling	2 x 2	6 x 3
Timing		
exposure time per image	50 ms	50 ms
stack capture time	20 s	25 s
rest between stacks	1 s	1 s
total acquisition time	15 min	5.8 h
Power		
488 nm	0.2 mW	0.2 mW
642 nm	0.5 mW	0.5 mW

The images captured on day 1 are shown in **Figure 5.7**. Panel **Figure 5.7a** shows the 3D organoid from a top view perspective while panels **Figure 5.7b** and **Figure 5.7c** show two orthogonal side perspectives. We can estimate that the size of the T cells are about 20 µm and that they are located about 30 to 50 µm deep in the skin model. Over an imaging period of 15 min, there was no significant migration of the T cells. I imaged the sample over a longer period of one hour but still, the T cells remained stationary.

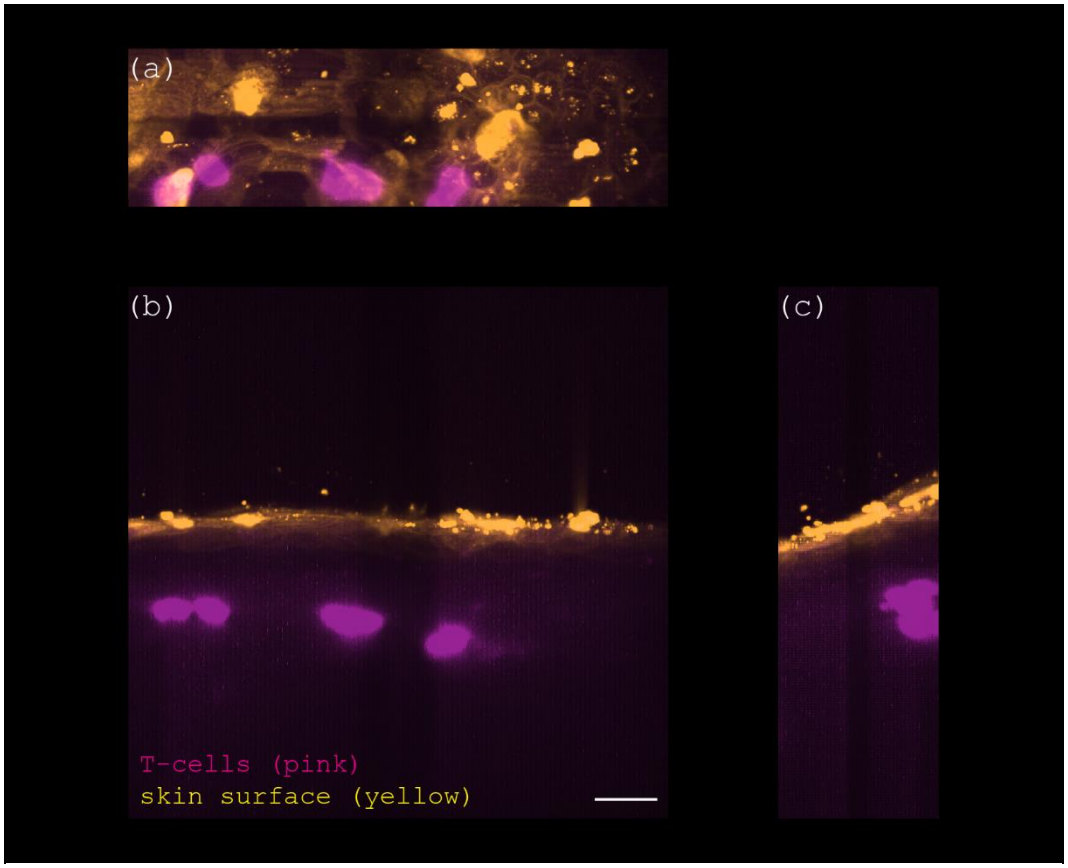

***Figure 5.7. 3D organotypic skin model on day 1**. **(a)** top view, **(b)** side view, **(c)** another side view of the 3D OSM. T cells are in pink (eGFP) and the top layer of skin cell membrane is in yellow (CellMask). The scalebar is 25 µm.*

On day 7, I imaged the sample for over 6 hours. The images for the first hour are shown in **Figure 5.8**. On day 7, it was harder to find the T cells in the sample. There is an eGFP signal in the middle of the field of view (arrow in **Figure 5.8**) which may originate from a T cell, however, its diameter is smaller compared to those observed on day 1. Moreover, the spot is closer to the surface than what was observed on day 1. Over the next hour, the signal also started to weaken and disappear as shown in **Figure 5.8**. During the remaining imaging period from 2-6 hours, there were no notable occurrences apart from a decrease in intensity in the 488 nm channel.

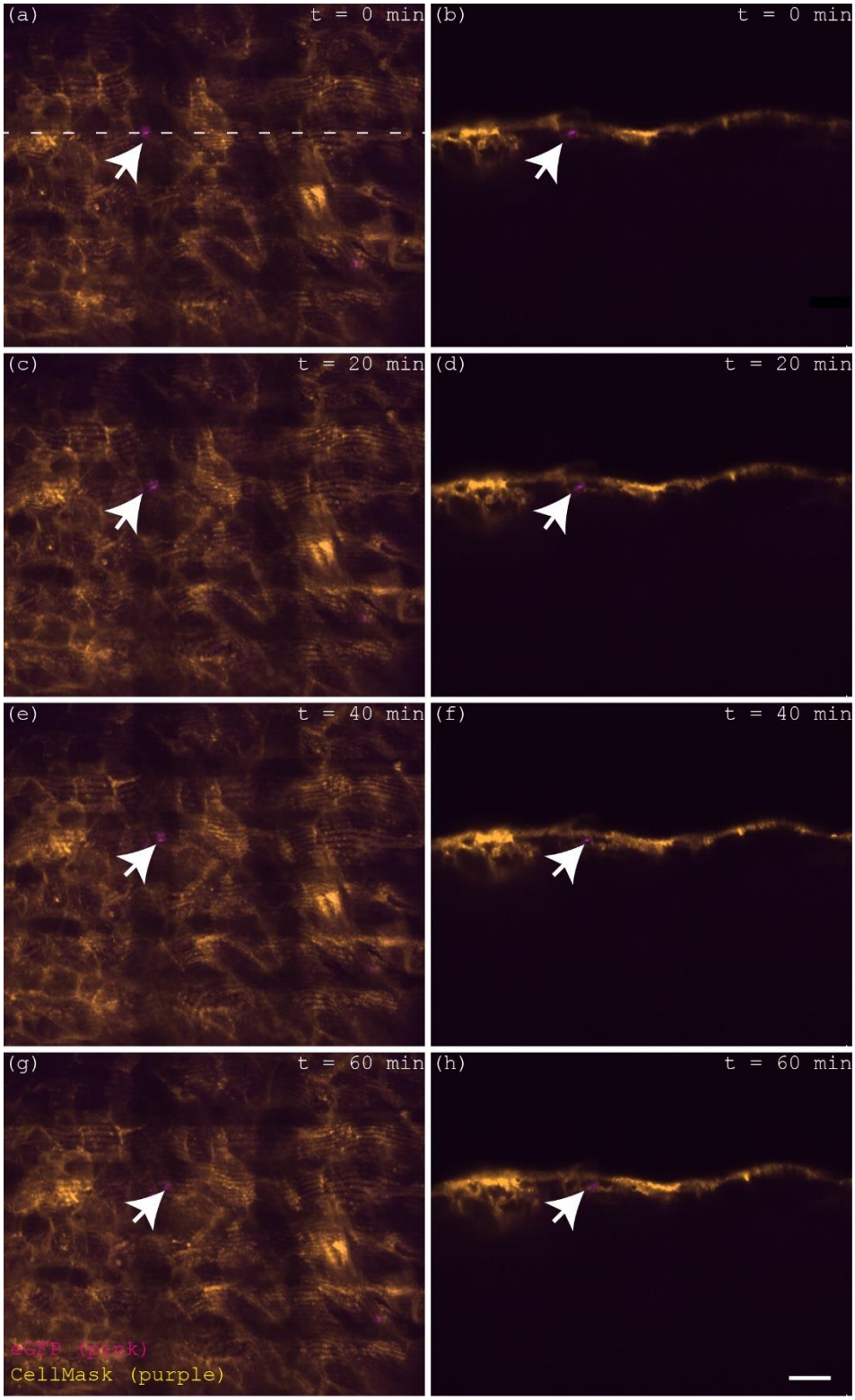

Figure 5.8. 3D organotypic skin model on day 7. *Top view perspective and slice of the OSM at* ***(a),(b)*** *0 min,* ***(c),(d)*** *20 min,* ***(e),(f)*** *40 min and* ***(g),(h)*** *60 min, respectively. The eGFP signal (white arrow) in the middle of the field could be from a T cell, but its diameter was smaller compared to day 1 and closer to the surface. Over the next 1 hour, the signal from the T cells started to weaken and disappear. The scale bar is 20 µm.*

These results have shown that we can observe the surface of the OSM and the immune cells under the surface. The size of the immune cells and their relative position to the OSM surface were estimated. By combining several 3D stacks, we can image a significant area of the OSM, though there are currently some stitching artifacts. These artifacts appear as regions of low intensity that can be seen from the top view in **Figure 5.8**. I suspect that this could be due to an averaging in the regions that overlap in the stitching. Despite our efforts, we were unable to demonstrate the ability to image the migration of immune cells within the OSM over an extended period. This was a result of the requirement to optimize the imaging parameters on day 1, as well as the loss of immune cells in later experiments on day 7. Additionally, a solution for moving the OSM surface between air and liquid during imaging was not pursued. This approach would have allowed for the skin to absorb less liquid, potentially affecting the properties of the skin surface.

5.5 Discussion

With three imaging experiments, we demonstrated our capability to image both 2D and 3D samples, showcasing the versatility of the instrument in capturing a wide range of spatiotemporal dynamics, including subcellular vesicle movement and whole cell activity. Our results showed that we were able to maintain live samples in our chamber for a substantial time of 6 hours, but the quality of the images was impacted by a decrease in fluorescence signal intensity caused by photobleaching.

We observed significant crosstalk when capturing the 560 nm channel and 642 nm channel in camera B. However, this could be solved in the future by using a different set of filters. For example, by replacing Di03-R561-25x36 with Di01-R488/561-25x36, allowing the 488 nm channel and 642 nm channel to be captured together in camera B while the 560 nm channel can be captured with camera A. It should still be verified if this filter works for a particular experiment since the crosstalk will depend on the specific markers in the sample. However, since the 560 nm excitation is between the 488 nm and 642 nm channel, separating it to another camera might reduce the occurrence of crosstalk in general.

A crucial aspect to consider when imaging in 2D versus 3D is the scanning direction of the sample. In the case of a 2D sample, a simple translation along the horizontal axis (x-axis)

provided a sufficient field of view. However, when imaging the 3D sample, I used a scanning direction along the xz-axis. This method resulted in a limited imaging area. To address this issue, I employed a tiling technique where the sample was scanned along the xz-axis in sections and then moved to the next section for scanning. The resulting tiled images were then stitched together to form a larger overall imaging area. The methods used to create 3D renderings from the images obtained by the different scanning directions also require different pre-processing. For images obtained by scanning along the xz-axis, creating a 3D rendering is straightforward and can be accomplished by simply stacking the images on top of each other. However, for images obtained by scanning along the x-axis, a step called deskewing is necessary to compensate for the distortion. The distortion occurs because the images were not collected along the optical axis of the detection path. This results in a rhomboidal volume rather than a rectangular one.

Another important insight gained in imaging the OSM was that the exogenous labels may have difficulties penetrating through the outer layers of the OSM. We were only able to label the surface of the skin with CellMask leading to difficulty in accurately identifying specific structures under the surface of the OSM. With the 3D OSM, it may be effective in the future to incorporate endogenous markers especially if the goal is to image the inner layers of the skin.

The mounting process of the OSM onto the coverglass is worth mentioning as it was a challenging task. The first step involved the removal of the organoid from the well insert by cutting around it to have access. To secure the OSM to the coverglass, a fibrinogen/thrombin solution glue was used. It proved to be effective in holding a relatively large OSM sample on the moving coverglass. This technique could be useful in mounting other 3D culture platforms for LLS imaging.

Finally, I found that it can be challenging to find a sample with the LLS. Since the LLS is only available in one magnification, it is difficult to determine which location, relative to the coverglass, is currently being imaged. Moreover, it was not straightforward to locate a sample in 3D. That is, it was challenging to find the surface of the sample. A simple trick that I use is to remove the multi-passband filter in front of the camera to detect the reflection off the surface of the sample. This reflection is usually more intense than the fluorescence and is thus easier

to spot. This trick is not only useful for a 3D sample but is also helpful in finding the surface of the coverglass when imaging a 2D sample, especially if the sample has a sparse signal.

Lastly, we acknowledge that further imaging experiments are necessary for uncovering new biological insights, but our results, imaging parameters, and procedures serve as a valuable resource in using the instrument for imaging both 2D and 3D live sample cultures.

Chapter 6. Experiment IV: Characterization of the LLS and data analysis

6.1 Introduction

The point spread function (PSF) is a quantity that describes how an infinitesimal point is imaged by an optical system. Measures of PSF size are commonly used to describe the resolving power of a microscope. In this section, I measure the PSF in the LLS and compare it with the measured PSF in a spinning disk microscope, a type of confocal microscope which uses multiple pinholes. I also calculate the theoretical size of the PSF in the LLS. Because of the configuration of the objectives in the LLS, the PSF is rotated relative to the sample coordinates. Thus, there is an increase in the z-resolution for the LLS in the sample coordinates, where ‘z’ is the axis orthogonal to the coverslip surface. I calculate the theoretical value for this “apparent” z-resolution in the sample coordinates. To explore caveats in the measurement and interpretation of the PSF, I also attempted to measure the apparent resolution from a 3D image stack that was processed to match the sample coordinates. When making this measurement (using a line-profile through the PSF recorded from a small emitter), one obtains a “false” measurement of the PSF, which I call the “misleading measurement of z-resolution”. This misleading measurement of the z-resolution is different from the measurement of the apparent z-resolution in the sample coordinates, and also different from the measurement of the z-resolution along the optical axis of the detection objective (i.e., along the long axis of symmetry in the PSF). My measures of the PSF in the spinning disk and my three different measures (long axis of symmetry, apparent, and misleading) of the PSF in the LLS are schematized in **Figure 6.1**.

In the next sections of this chapter, I describe the experiments I performed to measure the PSFs and discuss calculations of their expected sizes. I discuss how the PSF of the LLS can be recovered from an x-stack. I also derive an equation for the improved z-resolution in the sample coordinates. Moreover, I discuss a potential advantage of the improved (apparent) z-resolution in the sample coordinates resulting from the ‘tilted' objective configuration in LLS microscopy. Lastly, I apply the knowledge of PSF size in the LLS to track sub-diffraction sized CCPs in SVGA cells and I show examples of quantitative data that can be obtained from this analysis.

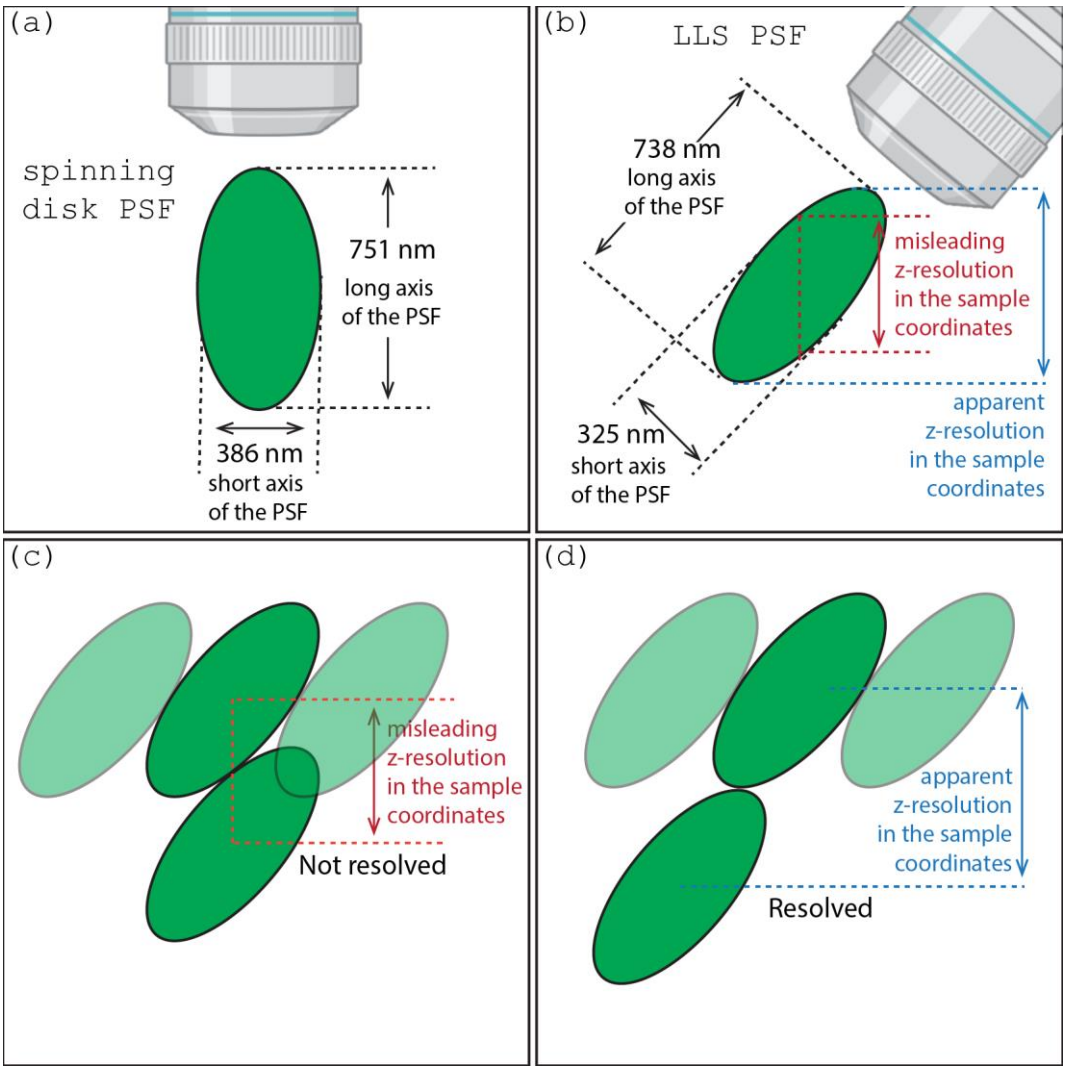

Figure 6.1. The configuration of how the different PSFs were measured. (a) *Measures of the spinning disk PSF.* ***(b)*** *Measures of the LLS PSF along its axes of symmetry.* ***(c)*** *Misleading z-resolution does not resolve the beads along the z-axis in the sample coordinates.* ***(d)*** *Apparent z-resolution resolves the beads along the z-axis in the sample coordinates.*

6.2 Measurement of the PSF

To measure the PSF, I imaged fluorescent beads (FluoSpheres™ carboxylate-modified 540 peak excitation/560 peak emission), 100 nm in diameter, with 488 nm excitation. These beads were attached to a cover glass following the **10.2 Bead gluing protocol** described in the **Appendix**. Using the LLS, a stack of 101 images in steps of 0.1 µm for a total range of 10 µm in the x-direction was captured (x-stack). For comparison, I also used a spinning disk microscope (Nikon Eclipse T2 inverted spinning disk, CFI Plan Apochromat Lambda, NA 1.40, WD 0.13 mm) to acquire a z-stack of the same sample, also in steps of 0.1 µm. A single image from each acquired stack is shown in **Figure 6.2**. Here, **Figure 6.2a** is an image in the

middle of the unprocessed stack captured with the LLS, and **Figure 6.2b** is the image where the beads are best in focus in the z-stack captured with the spinning disk microscope. Because of the tilted objective configuration in the LLS, the beads are only captured along the central vertical axis of the camera chip.

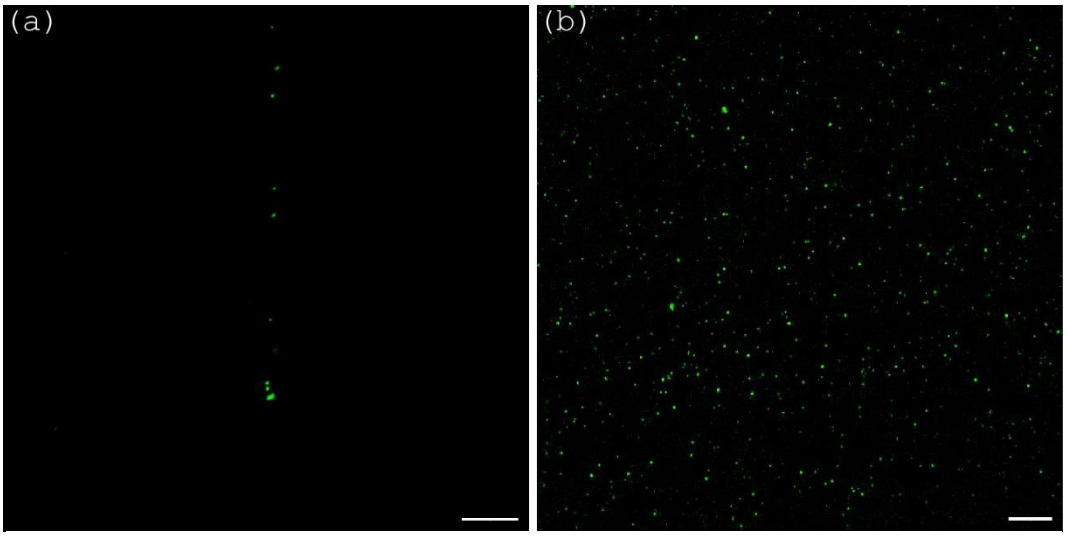

Figure 6.2. Beads on coverglass. *Selected images from 3D stacks captured with* ***(a)*** *LLS and* ***(b)*** *spinning disk microscope. The scalebars are 10 µm.*

To make a meaningful 3D representation of the images captured with the LLS, the image stack needs to be deskewed. As shown in **Figure 6.3**, deskewing is also necessary to recover the PSF. With the deskewed stack, the PSF of the LLS is readily measured along the axes of symmetry in the PSF. However, to match the coordinates of the sample, additional processing such as rotating and reslicing are required. The reslicing is necessary so that the depth of the stack corresponds to the z-axis of the sample coordinates. Moving forward, I call a stack that has been deskewed, rotated, and resliced the “processed stack”. The measurement of the PSF in the processed stack is an attempt to measure the resolution in the sample coordinates.

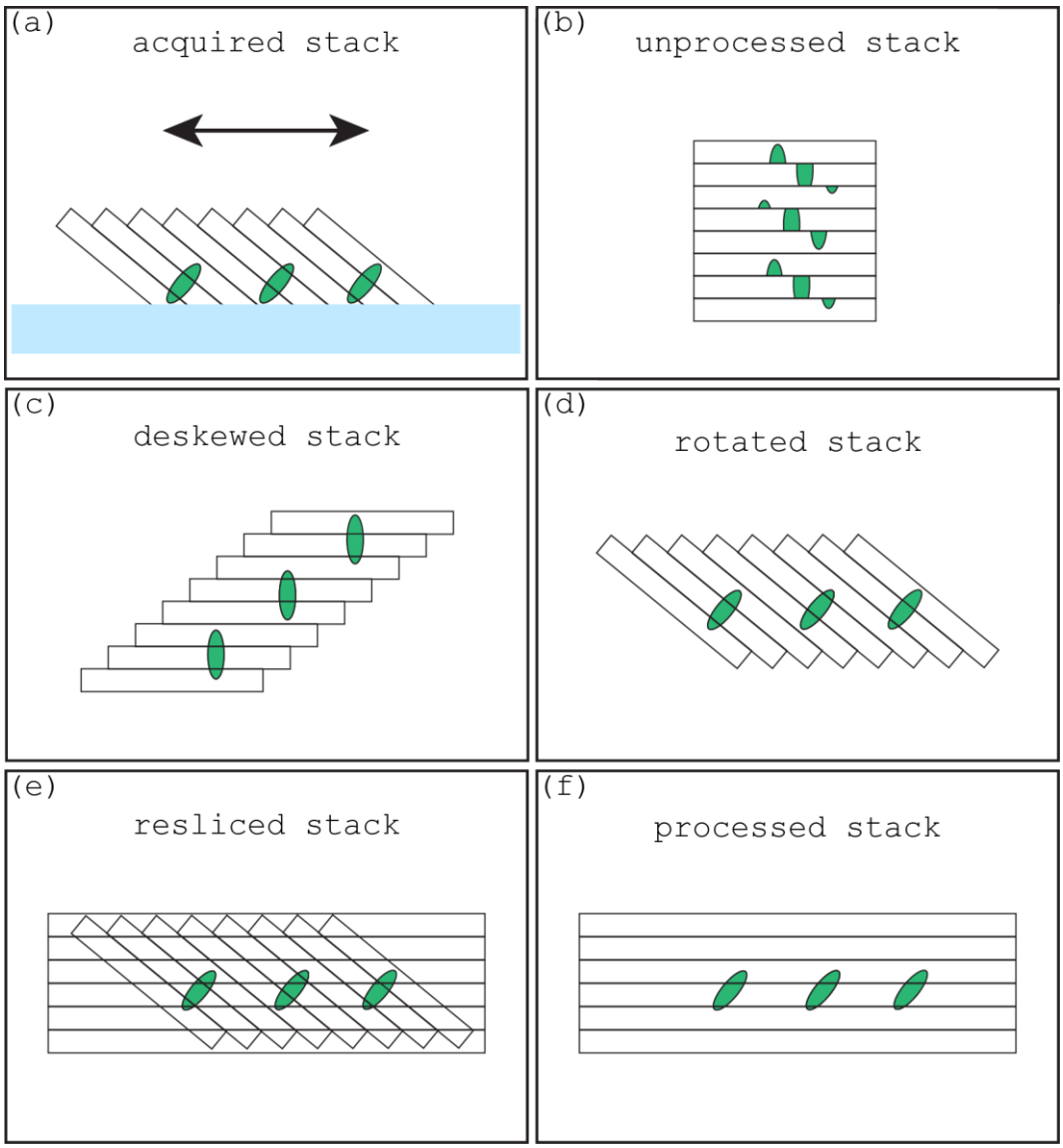

Figure 6.3. X-stack acquisition and processing*. These are the processing steps required to display a 3D image stack in a 3D grid aligned to the sample coordinates.* ***(a)*** *Acquired stack with x-stage movement.* ***(b)*** *Unprocessed stack.* ***(c)*** *Deskewed stack.* ***(d)*** *Rotated stack.* ***(e)*** *Resliced stack.* ***(f)*** *Processed stack.*

From the spinning disk stack, deskewed LLS stack, and processed LLS stack I manually selected beads which were isolated within a 15 × 15 pixel ROI and were not located at the edge of the image.

To measure the lateral resolutions, the focal plane for each bead was first determined by measuring the sum of intensities over the 15 × 15 pixels ROI. This is important for the deskewed LLS stack since the focal plane for each bead is at different image planes in the deskewed stack. Then, the 2D Gaussian function (below) was fitted to the intensity of the bead at this plane,

Experiment IV: Characterization of the LLS and data analysis

$$I(x,y) = \frac{1}{2\pi\sigma_x\sigma_y}\exp\left(-\frac{(x-x_o)^2}{2\sigma_x^2} - \frac{(y-y_o)^2}{2\sigma_y^2}\right) \tag{3}$$

Where x_o, y_o is the location of the center of the 2D Gaussian function while σ_x and σ_y describe the standard deviation of the Gaussian function along the x and y-axes, respectively. The FWHM is then calculated by: $\text{FWHM} = 2\sqrt{2\ln(2)}\,\sigma \approx 2.355\,\sigma$. For the axial resolution, a 1D Gaussian function was fitted to the intensity values along the z-linescan transecting the central coordinates x_o, y_o. As with the lateral resolution, the FWHM was calculated from the standard deviation σ_z of the 1D Gaussian function. This method was applied to the deskewed LSS stack, the processed LLS stack, and the spinning disk stack.

6.3 Comparison and calculation of PSFs

The "raw" z-linescans from a single bead in the deskewed LLS stack, processed LLS stack, and the spinning disk stack are shown in **Figure 6.4**. Before fitting a Gaussian function, the intensity values were normalized to a range from 0 to 100. Furthermore, the step size (of the x-stage) was multiplied by $\cos(58^o) \approx 0.53$ for the deskewed stack. The measurements for the other beads are found in **10.3 Bead PSF** in the **Appendix**.

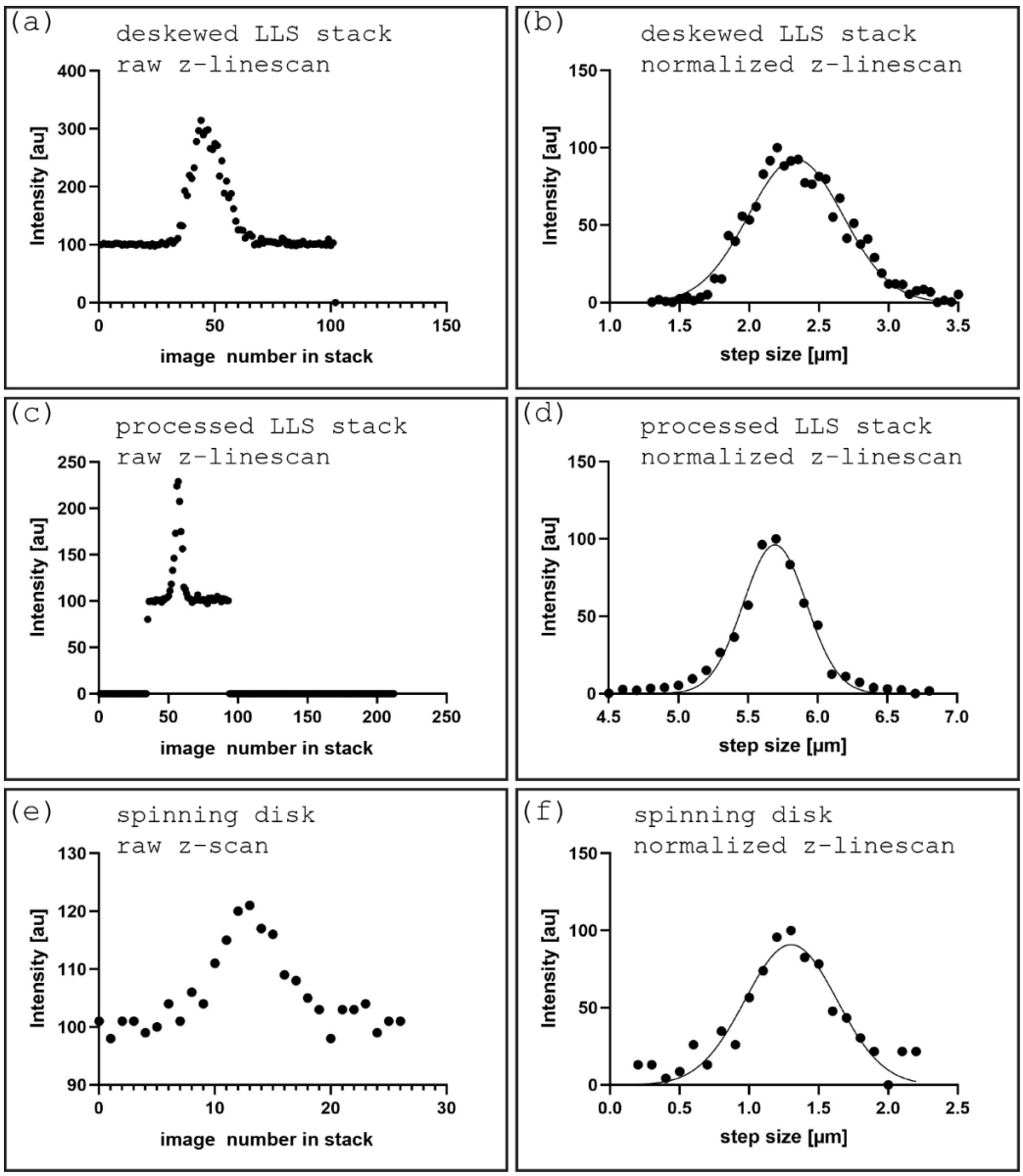

Figure 6.4. Z-linescan and Gaussian fit of representative beads. (a),(b) *LLS deskewed stack (z-axis is parallel with the optical axis of the detection objective).* ***(c),(d)*** *LLS processed stack (z-axis is orthogonal to the coverglass).* ***(e),(f)*** *Spinning disk (z-axis is orthogonal to the coverglass and parallel to the optical axis of the objective).*

Figure 6.5 provides a summary of the z-resolutions (measured as depicted in **Figure 6.4**) and the x/y-resolution measured via 2D Gaussian fitting. The mean (standard deviation) values for the XYZ resolutions measured from the deskewed LLS stack are 325 (22) nm, 316 (18) nm and 738 (35) nm, respectively. This corresponds to the measurement of the PSF in the LLS along its axis of symmetry. The XYZ resolution measured from the processed stack of the LLS are 429 (32) nm, 364 (27) nm and 550 (24) nm, respectively. This corresponds to the misleading measurements of the PSF in the LLS. While the XYZ resolution for the spinning disk are 386 (62) nm, 383 (65) nm and 751 (111) nm, respectively.

Experiment IV: Characterization of the LLS and data analysis

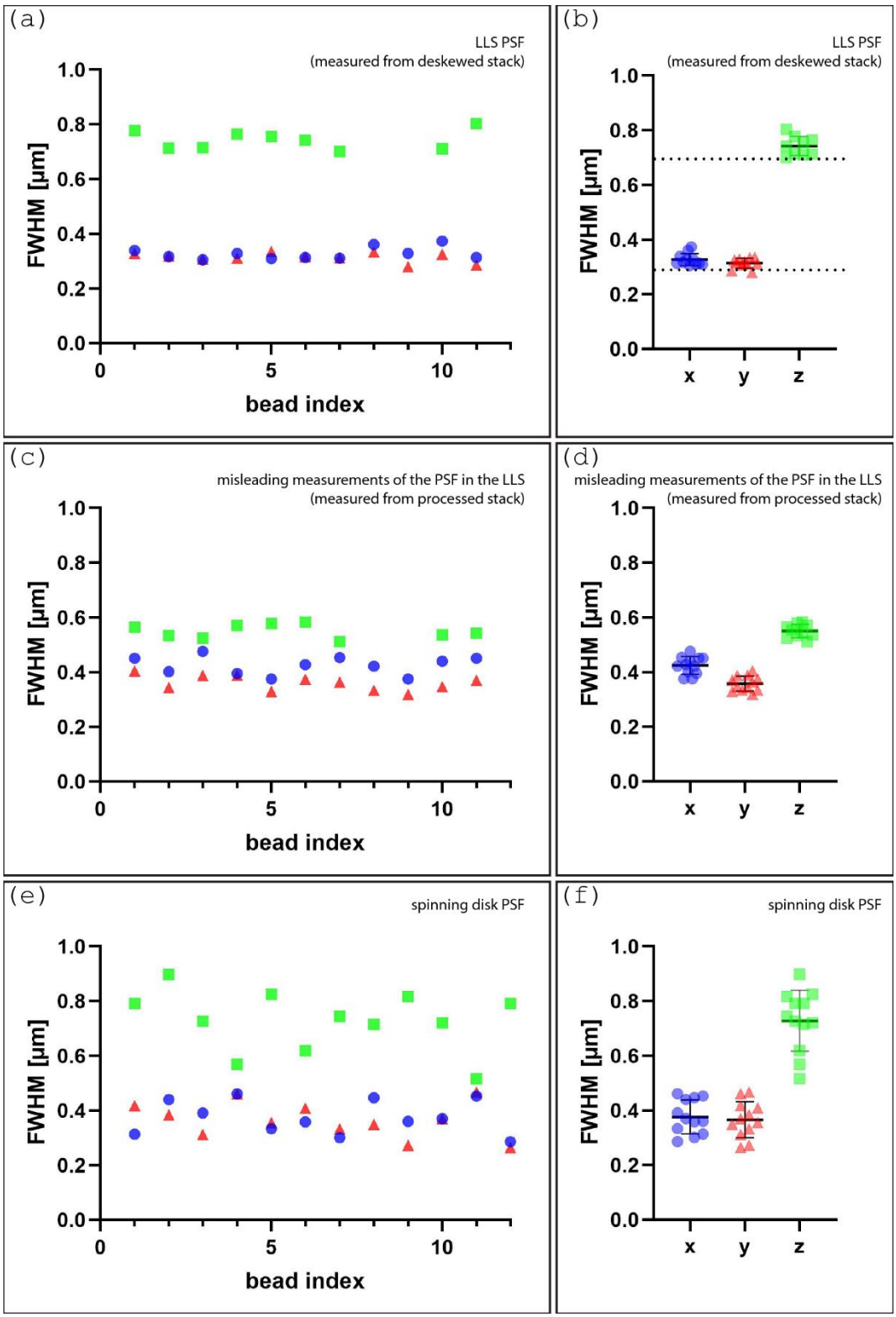

Figure 6.5. PSF measurements. (a),(b) *LLS PSF measured from the deskewed stack.* ***(c),(d)*** *Misleading measurements in the PSF in the LLS measured from the processed stack.* ***(e),(f)*** *Spinning disk PSF. The dotted lines in* ***(b)*** *are the theoretical values for the PSFs in the LLS.*

The expected (theoretical) x and y resolution of the LLS can be calculated using the Rayleigh criterion, $R_{x,y} = 0.61\frac{\lambda}{NA} = 0.61\ \frac{(550\text{ nm})}{1.0} = 335\text{ nm}$. However, the Rayleigh criterion measures the resolution as the radial distance from the center to the first intensity minimum of the Airy disk. To obtain the FWHM, the Rayleigh resolution must be multiplied by a factor of 0.85, $335\text{ nm} \times 0.85 \approx 285\text{ nm}$.

The expected (theoretical) z resolution of the LLS can be approximated by assuming that the illumination profile and the detection profile of the detection objective are both Gaussian functions along the axis of the detection objective, $\text{Illumination}(z) \sim \exp\left(-\frac{z^2}{\sigma_{LS}^2}\right)$, $\text{detection}(z) \sim \exp\left(-\frac{z^2}{\sigma_d^2}\right)$. The resulting PSF will then also have a Gaussian profile $PSF_z \sim \exp\left(-\frac{z^2}{\sigma_z}\right)$ where $\frac{1}{\sigma_z^2} = \frac{1}{\sigma_{LS}^2} + \frac{1}{\sigma_d^2}$.

The standard deviation of the best fit Gaussian function applied to the thickness of the LLS was measured to be $\sigma_{LS} = 448$ nm. This measurement is shown in **10.4 LLS thickness measurement** in the **Appendix**. The Rayleigh criterion for z resolution gives $R_z = \frac{2\lambda}{NA^2} = \frac{2\ (550\text{ nm})}{1} = 1.1\ \mu\text{m}$. From this, the standard deviation of the Gaussian detection profile can be calculated as $\sigma_d = (R_z)\ \frac{0.85}{2.355} = 397\text{ nm}$.

Finally, from σ_{LS} and σ_d, σ_z is calculated to be,

$$\sigma_z = \sqrt{\frac{1}{\frac{1}{\sigma_{LS}^2} + \frac{1}{\sigma_d^2}}} = \sqrt{\frac{1}{\frac{1}{0.448^2} + \frac{1}{0.397^2}}} = 297\ nm \qquad (4)$$

This standard deviation σ_z corresponds to a FWHM of 700 nm. The expected (theoretical) FWHM measures of the PSF are indicated by the dotted lines in **Figure 6.5b**. Relative to these expected values, the measured PSF of the LLS (from the deskewed stack) deviate by 5% (for the FWHM in z), 14% (for the FWHM in x) and 11% (for the FWHM in y).

Experiment IV: Characterization of the LLS and data analysis

6.4 Tracking of CCPs in SVGA cells

Having established the shape and size of the PSF, it becomes possible to track sub-diffraction-sized structures (i.e., fluorescence-labeled structures that are significantly smaller than the PSF), as such structures will appear in the known shape of the PSF when imaged. **Figure 6.6** shows LLS images of SVGA cells expressing eGFP on CCPs and the localization of these spots. The method for imaging these SVGA cells was covered previously in **5.2 Imaging a test sample**. To track these CCPs, I used the Fiji plugin TrackMate, which is popular for single particle tracking [96], [97]. The tracking algorithm requires an estimation of the spot size for these CCPs as input. Given that the CCPs are smaller than the resolution of the LLS, their size will correspond to the PSF when imaged.

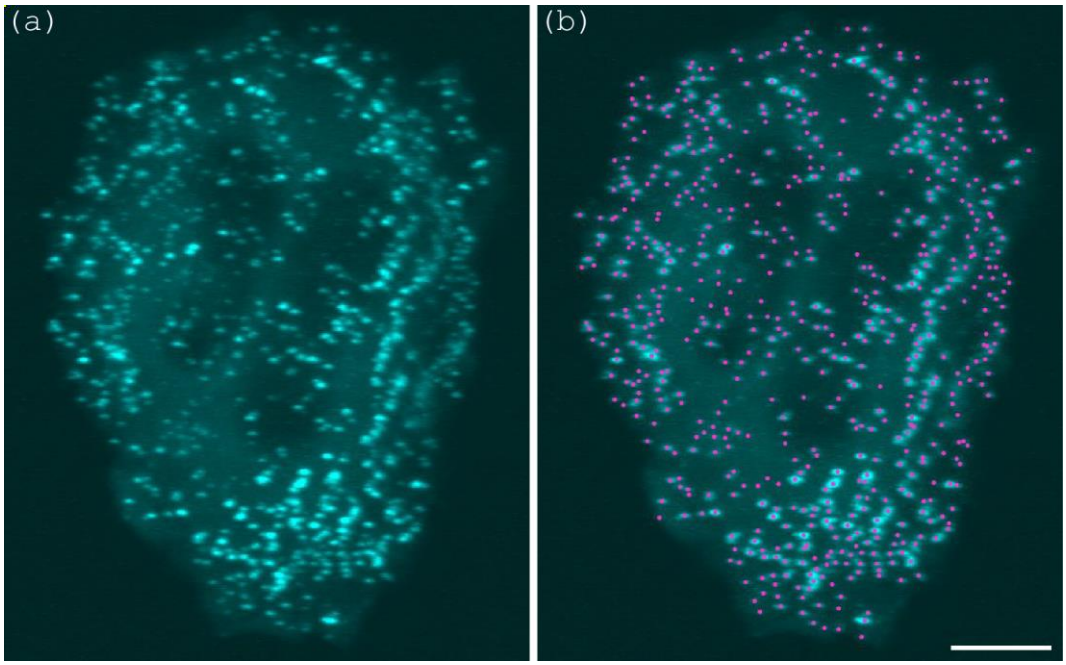

Figure 6.6. CCP tracking. *Maximum intensity projection images of* ***(a)*** *SVGA expressing eGFP on CCPs.* ***(b)*** *Localization of the CCPs. The scalebar is 10 µm.*

Figure 6.7 displays the estimated locations of the CCPs in 3D space as determined by TrackMate. In **Figure 6.8**, the speed and trajectory of the CCPs are visualized. Furthermore, **Figure 6.9** presents various quantities (such as location, speed, and intensity) that can be easily extracted using TrackMate. Notably, **Figure 6.9a** and **Figure 6.9b** show the spatial distribution of the CCPs across the x, y, and z-axes in the sample coordinates, revealing that a majority of

the spots are situated at the bottom of the cells. By examining the cumulative distribution in **Figure 6.9c**, it is evident that approximately 90% of the CCPs are located within the bottom 4 µm of the cell (from 5 µm to 9 µm relative z-position). Additionally, **Figure 6.9d** demonstrates that brighter spots tend to be concentrated at the bottom of the cell, while **Figure 6.9e** illustrates the decay of intensity over time. Lastly, the occurrence of different speeds exhibited by the CCPs is depicted in **Figure 6.9f**.

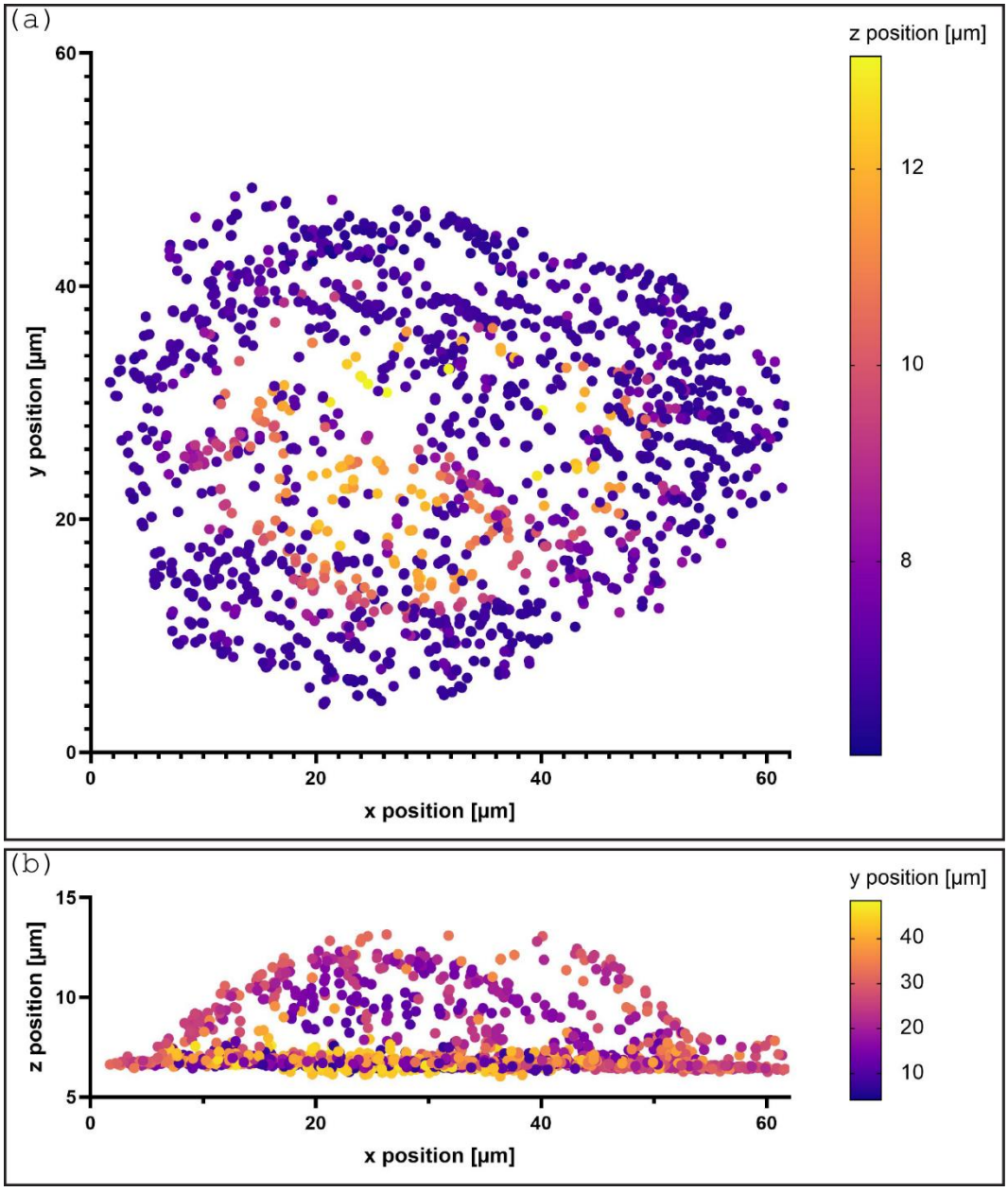

*Figure 6.7. Distribution of the spots is space. **(a)** Top view. **(b)** Side view.*

Experiment IV: Characterization of the LLS and data analysis

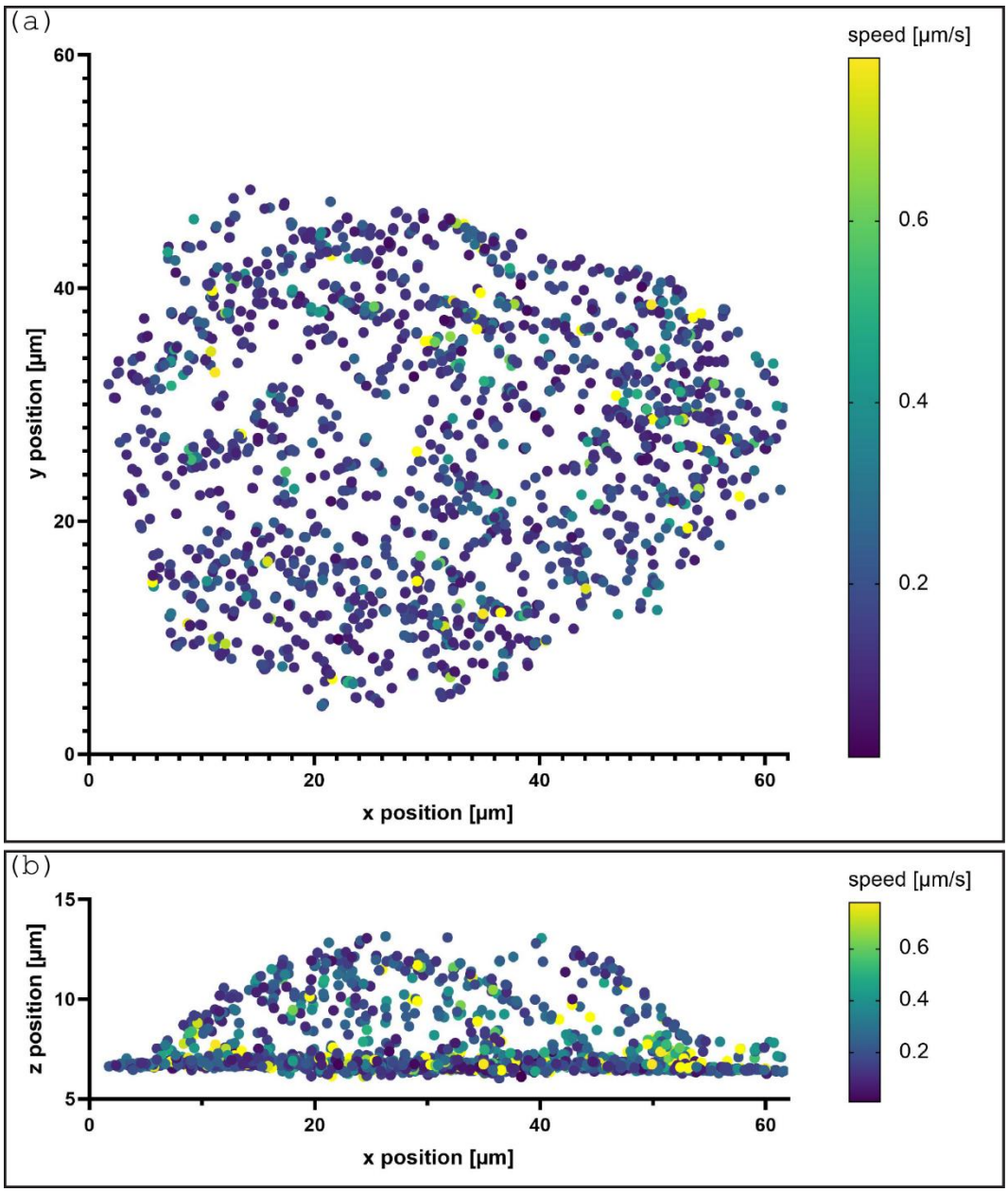

Figure 6.8. Distribution of the speed of the spots. (a) *Top view.* ***(b)*** *Side view.*

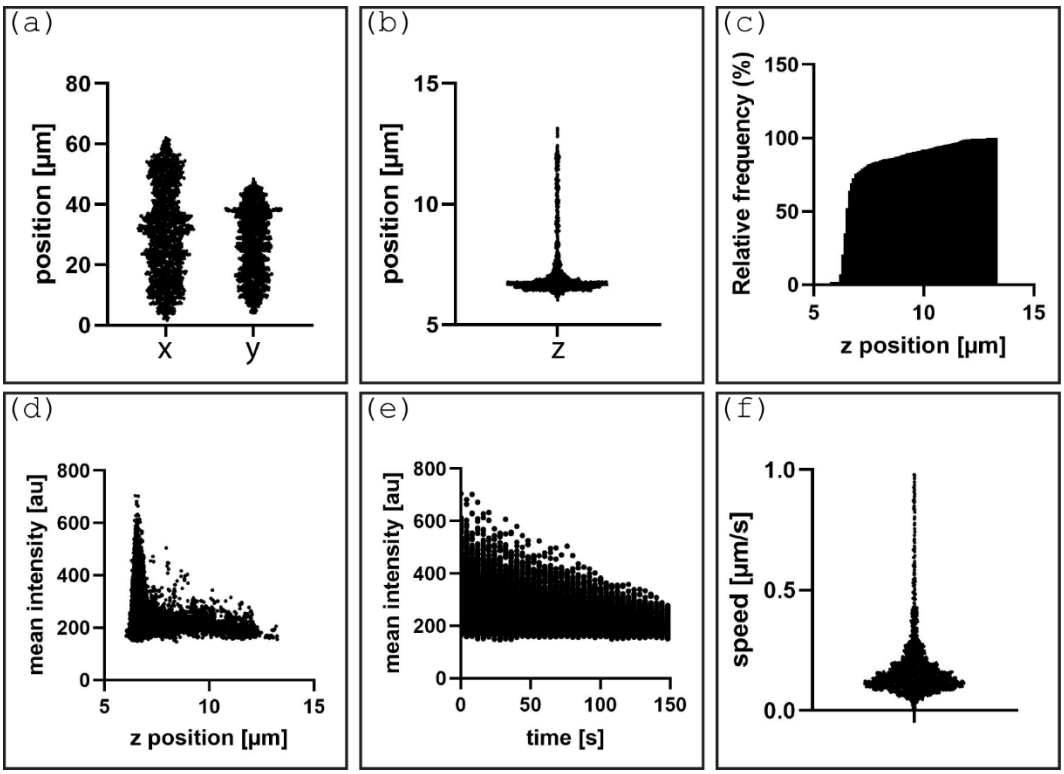

***Figure 6.9. Quantitative measurements from tracking of the CCPs**. **(a)** Distribution of the CCPs in the x and y axes in the sample coordinates. **(b)** Distribution of the CCPs in the z-axis in the sample coordinates. **(c)** Cumulative distribution of the CCPs along the z-axis. **(d)** Intensity of the CCPs s along the z-axis. **(e)** Mean intensity of the CCPs over time. **(f)** Occurrence of different speeds of the CCPs.*

Here, my primary aim is not to uncover groundbreaking biological discoveries. Instead, my focus lies in illustrating the vast wealth of information that can be extracted by utilizing image-analysis methods like particle tracking with images captured with the LLS.

6.5 Discussion

The PSF of the LLS measured from a deskewed stack that is acquired with the x-stage movement (horizontal motion) yields the same estimate of the size of the PSF measured (previously in **Figure 4.11**) from a stack acquired with xz-stage movement (detection objective direction). However, it is important to note that when calculating the z-resolution from an x-stack, that a unit movement of the x-axis is equivalent to cos(58º) ≈ 0.5 units of movement along the axis of the detection objective. Consequently, the step size was rescaled by this factor

before fitting a Gaussian function. I chose to acquire an x-stack instead of an xz-stack to maximize the number of captured beads in a stack.

With respect to the sample coordinates, the PSF of the LLS is rotated. Thus, leading to an apparent increase in the z-resolution in the sample coordinates. I measured this apparent resolution by first processing the stack. That is, by deskewing, rotating and reslicing the stack to match the sample coordinates. Then, I took an axial linescan of the intensity and fitted a Gaussian function – as one would normally do. However, blindly applying this method leads to a misleading measurement of the PSF. The misleading measurement of the PSF is not necessarily enough to resolve (along the z-axis) two beads located close to each other along the x and y-axes and roughly above each other (along the z-axis), as shown **Figure 6.1c,** while the apparent measurement of the PSF is the minimum distance (along the z-axis) required to ensure that two such beads are resolved, as shown in **Figure 6.1d**. It is not straightforward to establish the apparent measure of the PSF. However, it can be calculated from a 3D image acquisition of the PSF and the angle of acquisition. In **10.5 Analytical expression for the apparent z-resolution in the sample coordinates in the LLS** in the **Appendix**, I calculated the value of the apparent z-resolution in the sample coordinates by calculating the height of a rotated ellipse defined by the PSF of the LLS. This leads to an apparent z-resolution of

$$PSF_{z-apparent} = 2R_z \sin(\theta)\cos(t) + 2R_x \cos(\theta)\sin(t) = 649 \text{ nm} \qquad (5)$$

where $t = \tan^{-1}(\frac{R_x}{R_z \tan(\theta)})$, θ is the angle between the optical axis of the detection objective and the coverslip, $2R_z$ is the FWHM of the PSF in the LLS along the optical axis of the detection objective, and $2R_x$ is the FWHM of the PSF in the LLS along the axis that is orthogonal to the optical axis of the detection objective. This gives an apparent z-resolution of 649 nm which is in between the misleading measurement of the z-resolution and the correct measurement of the z-resolution. In the calculation, I used the measured values of the PSFs, $2R_z$ = 738 nm, $2R_x = 325$ nm and θ = 58º. It must be noted that this apparent z-resolution in the sample coordinates depends on the angle of acquisition. In the extreme case where the detection objective is rotated 0º, the apparent z-resolution given by **Equation 5** approaches the value of $2R_x = 325$ nm, as expected. Here, I focused on the apparent z-resolution in the sample coordinates, but since the PSF is rotated in the xz-plane, the same analysis can be applied to

the apparent x-resolution in the sample coordinates. However, instead of an increase in resolving power, there is a decrease in the x-resolution in the sample coordinates. **Equation 5** can be useful in tuning the angle of acquisition of the LLS for a desired resolution trade-off between the z and x-resolutions in the sample coordinates. In the y-axis, the resolution does not change in the sample coordinates.

These apparent resolutions in the sample coordinates are rarely reported in the literature. Usually, only the size of the PSF along the axis of the detection objective (and the orthogonal directions) are reported. However, in some cases, the apparent resolution in the sample coordinates may be more relevant. For example, Hundahl *et al.* [98] investigated the transport of peptides through a 2D culture of Caco-2 cells using an inverted spinning disk microscope, as depicted in **Figure 6.10a**. **Figure 6.10b** illustrates the sample before the addition of the peptide, while **Figure 6.10c** shows the sample after the peptide has been added. There was a noticeable increase in the intensity of the green channel (peptide), indicating a movement of the peptide from the medium to the bottom of the cells. However, the spinning disk that was used to capture these images did not have the adequate resolution to capture whether the peptides ended up outside the cell (in the narrow spaces between the cells and the substrate) or inside the cell (along the bottom of the cell membrane). When deciding whether an LLS imaging system would be a better alternative to the used spinning disk microscope, in this particular scenario, it would be more relevant to consider the apparent z-resolution in the sample coordinates compared to the z-resolution along the detection objective.

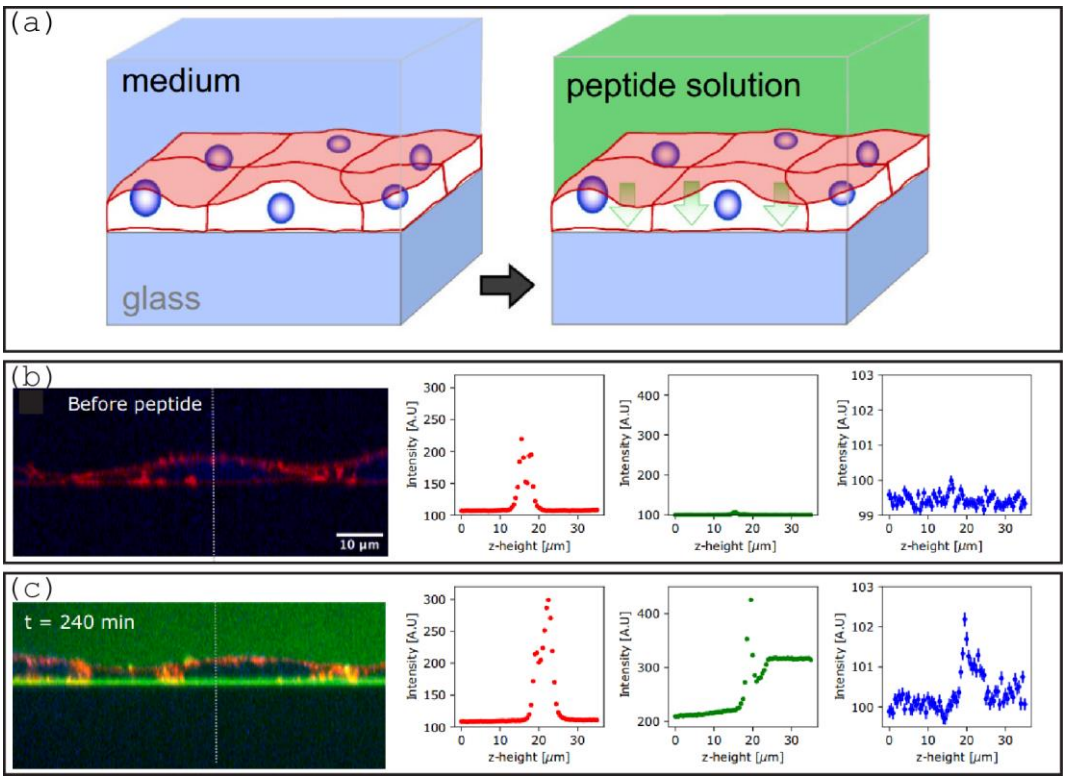

Figure 6.10. Peptide transport by Caco-2 cells. (a) *Caco-2 cells on coverglass transport the peptide from the top to the bottom of the sample.* ***(b)*** *Before addition of the peptide.* ***(c)*** *4h after adding the peptide. There is an increase in the green channel (peptide) in the bottom of the cell. Imaging with high resolution along the axis perpendicular to the substrate might reveal whether the peptide locates to the substrate, to the basal plasma membrane of the cells, or to the space in between. Reproduced from* [98] *with permission from Elsevier.*

Lastly, I presented quantitative data obtained from tracking of the CCPs in the images captured with the LLS. For the tracking analysis, I used the processed stack as it allowed me to obtain the positions relative to the sample coordinates. Alternatively, a deskewed stack could also be used to extract these quantities. However, it is worth noting that with TrackMate analysis, the stack depth is interpreted as the z-axis while the image plane as the xy-axis. Thus, using the deskewed stack in TrackMate will require additional calibration of the position outputs. Moreover, it would be more appropriate to localize the CCPs by utilizing a fitting routine that allows for rotational degrees of freedom that would enable the alignment of the actual shape of the rotated PSF with the CCP "spots" in the acquired 3D image. Understanding the

characteristics of the PSF and the processing steps applied to the stack is crucial for accurate quantitative data analysis of the images captured with the LLS.

In this context, the primary objective is not centered around revealing revolutionary biological findings. Rather, the emphasis is on demonstrating the extensive range of valuable information that can be derived through the application of image-analysis techniques with images acquired using the LLS with the hope to inspire and encourage further exploration and utilization of the instrument.

Chapter 7. Discussion

I have built and implemented the lattice light-sheet microscope following the blueprints of the MOSAIC microscope from the Betzig group. Moreover, I have demonstrated the capability of the instrument to image both 2D samples and 3D biomimetic cultures, showcasing the versatility of the instrument in capturing a wide range of spatiotemporal dynamics, including subcellular vesicle movement and whole cell activity.

Although the design of the MOSAIC was well-documented, I have encountered some complexities and issues during the building process that could be solved or simplified. These practical considerations were outlined to help other builders of the MOSAIC. Some of the central findings in this thesis are:

- Discovering some flaws in the manufacturing of custom-made components.
- Documenting challenges in building the instrument and suggestions practical considerations that can solve them.
- Discovering absorption of fluorescent dye in the detection objectives.
- Discovering the shift in focus when aligning using medium versus water.
- Establishing a way to simulate widefield illumination using lattice light-sheet excitation.
- Suggesting a different filter to reduce crosstalk between the 560 nm channel and 642 nm channel.
- Establishing a protocol for the imaging of 3D OSM and optimizing the scanning direction of the sample stage for probing deeper into the sample versus probing a larger area of the sample.
- Establishing a mounting procedure for relatively large samples onto the coverglass for the imaging of 3D cultures.
- Suggesting a method to quickly find samples with the single magnification objective of the instrument.
- Measuring and calculating the PSF of the LLS and comparing it with the spinning disk
- Deriving and calculating the apparent resolution of the LLS relative to the sample coordinates.

- Illustrating some quantitative data that can be obtained from LLS images.

Compared to the optical designs of the stand-alone LLS in [38], and stand-alone LLS with adaptive optics in [99], the design of the LLS in the MOSAIC was more complex due to the presence of other imaging modes that share components with the LLS path. This complexity can lead to an increase in optical aberrations. To mitigate these system aberrations, I performed aberration corrections using the SLM and the deformable mirror. The instrument also allows to correct for sample-induced aberrations using the deformable mirror, although this function is currently not operational. Moreover, one strength of the MOSAIC is the capability to combine multiple different imaging modes in a single instrument. However, we did not have time to test and use this feature in this project.

The most important advantage of the LLS in the MOSAIC compared to the earlier version in [38] is the bigger sample chamber and sample holder that would enable imaging of larger samples. Additionally, new custom-made optical components are found in this version of the LLS which could enable simultaneous imaging of multiple channels (up to 7 channels). Furthermore, a new design of the mask allows to quickly vary the light-sheet parameters. Unfortunately, these cannot be discussed here due to the confidentiality agreement with Janelia Research Campus. Nevertheless, these advantages have made the MOSAIC an attractive option for our goal of imaging 3D biomimetic cultures.

In addition to imaging a 3D transwell skin culture, I also attempted to image a 3D organoid culture and a 3D printed scaffold for an organ-on-chip. However, I encountered several challenges while imaging these complex samples. One of the difficulties arose when imaging an apical-out 3D organoid culture. These samples are particularly delicate to immobilize because attaching them to a support inhibits their apical-out polarization. To address this, we experimented with partially embedding the organoids in a 3D printed resin. Unfortunately, we observed that this approach led to cell death and fragmentation, rendering the samples unsuitable for imaging. Further exploration is required to find alternative methods that preserve the structural integrity of apical-out organoid cultures during imaging.

We investigated another set of samples consisting of 3D printed columns protruding from the base at regular intervals as a kind of sample holder for the organoids. These columns had the

purpose of limiting the motion of each organoid during visualization. They have a radius of 0.05 mm and a height of 0.7 mm and were composed of 20% PEGDA 700 (poly(ethylene glycol) diacrylate with a mean molar weight of 700 g/mol) and 80% water. The refractive index of this mixture is approximately n = 1.36. One major challenge encountered when imaging the column structures was the presence of significant aberration. As the objectives of the LLS were positioned at an angle, both the illumination and detection paths must travel through the thickness of the columns. To illuminate the side facing the detection objectives, the excitation beam must go through the column, from left to right. Consequently, the fluorescence signal emitted from the left side of the column also must go through the thickness of the column, further increasing the distortion. Although we managed to observe some fluorescence signal, the resulting images were heavily distorted, making it difficult to discern specific features.

In this thesis, I experimentally compared resolution measures in the LLS (excitation NA = 0.6 and detection NA = 1.0) to resolution measures in a high-end spinning disk microscope with an inverted objective (NA = 1.4). The measured FWHM of the PSF are 325 nm, 316 nm, and 738 nm XYZ resolution for the LLS while 386 nm, 383 nm, and 751 nm XYZ resolution for the spinning disk. With a higher NA of the objective in the spinning disk, it could be expected to provide a better resolution. However, I observed a larger standard deviation in the measurements of the PSF in the spinning disk compared to the measurements of the PSF in the LLS. The standard deviations are 62 nm, 65 nm, and 111 nm for the XYZ resolution of the spinning disk, while standard deviations are 22 nm, 18 nm, and 35 nm for the XYZ resolution of the LLS. This increased variability may be attributed to the presence of more background noise in the images captured by the spinning disk microscope compared to the LLS. The LLS is inherently better at reducing the background noise since the vertical layers above and below the PSF are not excited. Thus, the LLS system provides a better photon budget for achieving a given signal-to-noise ratio leading to higher quality recordings.

Furthermore, while both spinning disk and LLS have comparable measured resolutions, one advantage of the LLS is its potential for lower photodamage due to the light-sheet illumination as discussed in **1.2.3.1 Principles of light-sheet microscopy**. However, it is important to acknowledge that LLS has its own limitations, particularly related to the use of two objectives, which restrict the size and geometry of the 3D cultures that can be imaged. In contrast, the spinning disk microscope provides more flexibility in accommodating large 3D samples. Its

inverted configuration allows for faster switching of samples and imaging multiple culture dishes or multi-well plates. However, the most relevant configuration, whether inverted or upright will be entirely sample dependent. For the 3D transwell culture in **5.4 Imaging a 3D organotypic model of skin**, the upright (but tilted) configuration of the objectives in the LLS is preferable to avoid imaging through the basal layers of the sample. Moreover, the tilted configuration of the objectives in the LLS provides an apparent improvement in the z-resolution in the sample coordinates. This apparent z-resolution in the z-axis of the sample coordinates was calculated to be 649 nm.

Additionally, it is worth noting another modality that offers optical sectioning for imaging thick biological samples is two-photon microscopy. Two-photon microscopy utilizes longer-wavelength excitation light, typically in the near-infrared range, which allows for deeper penetration into the sample compared to conventional fluorescence microscopy. This enables the imaging of thicker specimens. However, two-photon microscopy also has certain limitations. One of the main disadvantages is the relatively long image acquisition time due to the inherent point-scanning approach. The excitation laser must be scanned across the sample point by point, which can be time-consuming, especially for large field-of-view or high-resolution imaging. Typically, point scanning methods achieve frame rates of around 30 frames per second (fps) [100]. In contrast, the LLS has the potential to significantly improve the acquisition speed, offering the capability to capture images at rates of up to 100 fps. Furthermore, the requirement for focused excitation and high laser power for two-photon excitation can potentially be damaging to living samples [101,102]. While the MOSAIC has the potential to combine two-photon with light-sheet imaging, this was not explored in this thesis. Nonetheless, with the LLS, I was able to capture a volume of 400 um x 225 um x 190 um over 6 hours every 7 mins by tiling 6 x 3 stacks in the imaging of the 3D skin culture.

The MOSAIC can be effective in imaging large, self-sustaining samples, such as zebrafish and drosophila, which possess inherent natural barriers and exhibit resilience to external factors. However, when adapting the MOSAIC for imaging 3D biomimetic cultures, certain additional features can be improved. One important aspect is modifying the sample chamber to provide long-term life support for the cultured samples. A mini-incubator could be incorporated into the sample chamber to ensure the viability of the samples for long-term live imaging. Moreover, with the current design of the sample chamber, the entire volume of the chamber is

contaminated by the sample. The development of a fast and efficient method for sample placement and replacement while at the same time isolating each sample from the rest of the instrument to prevent contamination of the entire sample chamber could also be explored. For example, Moore *et. al* [103] developed a microfluidic device made of FEP that is compatible with the LLS and that separates the sample from the sample chamber. It can be securely sealed off from the external environment, enabling easy removal and reattachment to the LLS while maintaining sterility. Adapting a similar device to accommodate larger samples would be advantageous for imaging 3D biomimetic structures using the LLS.

In the case of imaging 3D skin samples, we were fortunate that these samples were relatively robust and presented a natural barrier. However, this natural barrier also presented a drawback. The penetration of exogenous markers through the skin barrier proved to be challenging, emphasizing the importance of using fluorescent genetic labels (like eGPF in **5.2 Imaging a test sample)**.

Ultimately, the choice of technique should be based on the specific requirements of the study, taking into consideration factors such as imaging speed, photodamage concerns and geometric compatibility related to fitting the sample into the instrument.

Finally, since the instrument can acquire a huge amount of data, it is important to consider how to handle and store the acquired data files. A single Orca Camera can capture a 16-bit grayscale image with dimensions of 2048 × 2048 pixels that would have a size of approximately 8 MB. Ultimately, the amount of data will depend on the experiment and the acquisition settings. For the imaging experiments in Chapter 5, a two-color stack that consists of 100 images captured at 100 time intervals has a size of about 160 GB. So far, the acquisition computer is not connected to the DTU network and the image data is stored locally. As the storage can be depleted quickly, in the future the instrument can be connected to a data server to stream the images after acquisition.

Although optical lattices are widely used in lattice light-sheet microscopy and have recently been incorporated into commercial systems, some reports have questioned the superiority of lattice light-sheets over Gaussian light-sheets. While these interests remain regarding the lattice light-sheet and MOSAIC microscopes, the findings of this thesis contribute to the advancement

of the field of LLSM and provided practical guidance for future builders of the MOSAIC. The results and recommendations of this study can inform and guide future research and development of the MOSAIC microscope, as well as similar instruments, to further improve their imaging capabilities and performance.

Chapter 8. Conclusion

In this thesis, I presented the construction, optimization, and utilization of the lattice light-sheet mode of the MOSAIC microscope for imaging 3D cultures. The MOSAIC is a multimodal optical scope with adaptive imaging correction that integrates various imaging modes, including LLS, into a single instrument, allowing for dynamic switching between modes without the need to move the sample.

The design of the LLS component of the MOSAIC was based on the blueprints of the Betzig group. The construction process was modular, with components snapping into position with the help of guides such as holes, pins, and pegs. This made the building process simpler and faster, but it relied on very precise manufacturing of the custom-made components. During the building process, I encountered some complexities and issues that could be solved or simplified, which I have outlined in this thesis. The design of the LLS path in the MOSAIC was complex due to the presence of other imaging modes that share components with the LLS path, which can lead to optical aberrations. To mitigate these aberrations, I established optimization techniques and routines, including calibrating the SLM to achieve uniformity in the excitation beam and correcting system aberrations in both the excitation and detection paths using PWFC and phase retrieval algorithms, respectively. Furthermore, the LLS was optimized for long-term live sample imaging by incorporating temperature, CO_2, and evaporation controls in the sample chamber.

In our imaging experiments, we demonstrated the versatility of the MOSAIC in capturing a wide range of spatiotemporal dynamics, including subcellular vesicle movement and whole cell activity. Our results showed that we were able to maintain live samples in our chamber for a substantial time, but the quality of the images was impacted by a decrease in fluorescence signal intensity caused by photobleaching. A crucial aspect of MOSAIC's success was its ability to correct for both, system- and sample-induced aberrations, using adaptive optics, although the sample-induced correction was currently not operational due to the unavailability of a two-photon laser.

The PSF of the LLS was measured and compared with a spinning disk microscope. The expected (theoretical) PSFs were also calculated. Interestingly, because of the configuration of the objectives of the LLS, there is an apparent increase in the z-resolution relative to the sample coordinates. An equation is presented that gives this increased z-resolution in the sample coordinate. Moreover, tracking of the CCPs was demonstrated to highlight the wealth of information that can be effectively extracted with LLS imaging and subsequent image analysis. The primary aim of the analysis is not to uncover revolutionary biological discoveries. Instead by exemplifying these capabilities, I hope to inspire and encourage further exploration and utilization of the LLS.

In conclusion, the MOSAIC microscope has the potential to be a powerful tool for imaging 3D cultures with high axial resolution, minimal photobleaching, and illumination of the entire field of view. The results of this thesis contribute to the advancement of lattice light-sheet microscopy and provide important practical considerations for future builders of the MOSAIC.

Chapter 9. References

[1] J. R. Spence *et al.*, “Directed differentiation of human pluripotent stem cells into intestinal tissue in vitro,” *Nature*, vol. 470, no. 7332, pp. 105–110, Feb. 2011, doi: 10.1038/nature09691.

[2] T. Sato *et al.*, “Single Lgr5 stem cells build crypt-villus structures in vitro without a mesenchymal niche,” *Nature*, vol. 459, no. 7244, pp. 262–265, May 2009, doi: 10.1038/nature07935.

[3] M. A. Lancaster *et al.*, “Cerebral organoids model human brain development and microcephaly,” *Nature*, vol. 501, no. 7467, pp. 373–379, 2013, doi: 10.1038/nature12517.

[4] T. Kadoshima *et al.*, “Self-organization of axial polarity, inside-out layer pattern, and species-specific progenitor dynamics in human ES cell-derived neocortex,” *Proc Natl Acad Sci U S A*, vol. 110, no. 50, pp. 20284–20289, Dec. 2013, doi: 10.1073/pnas.1315710110.

[5] M. Takasato *et al.*, “Directing human embryonic stem cell differentiation towards a renal lineage generates a self-organizing kidney,” *Nat Cell Biol*, vol. 16, no. 1, pp. 118–126, Jan. 2014, doi: 10.1038/ncb2894.

[6] A. Taguchi *et al.*, “Redefining the in vivo origin of metanephric nephron progenitors enables generation of complex kidney structures from pluripotent stem cells,” *Cell Stem Cell*, vol. 14, no. 1, pp. 53–67, Jan. 2014, doi: 10.1016/j.stem.2013.11.010.

[7] R. E. Rayner, P. Makena, G. L. Prasad, and E. Cormet-Boyaka, “Optimization of Normal Human Bronchial Epithelial (NHBE) Cell 3D Cultures for in vitro Lung Model Studies,” *Sci Rep*, vol. 9, no. 1, Dec. 2019, doi: 10.1038/s41598-018-36735-z.

[8] “Novel Role for Netrins in Regulating Epithelial Behavior during Lung Branching Morphogenesis”, doi: 10.1016/j.

[9] S. R. Finkbeiner, X. L. Zeng, B. Utama, R. L. Atmar, N. F. Shroyer, and M. K. Estesa, "Stem cell-derived human intestinal organoids as an infection model for rotaviruses," *mBio*, vol. 3, no. 4, 2012, doi: 10.1128/mBio.00159-12.

[10] M. Eiraku *et al.*, "Self-Organized Formation of Polarized Cortical Tissues from ESCs and Its Active Manipulation by Extrinsic Signals," *Cell Stem Cell*, vol. 3, no. 5, pp. 519–532, Nov. 2008, doi: 10.1016/j.stem.2008.09.002.

[11] J. F. Dekkers *et al.*, "A functional CFTR assay using primary cystic fibrosis intestinal organoids," *Nat Med*, vol. 19, no. 7, pp. 939–945, Jul. 2013, doi: 10.1038/nm.3201.

[12] M. Ader and E. M. Tanaka, "Modeling human development in 3D culture," *Current Opinion in Cell Biology*, vol. 31, no. 1. Elsevier Ltd, pp. 23–28, 2014. doi: 10.1016/j.ceb.2014.06.013.

[13] A. Fatehullah, S. H. Tan, and N. Barker, "Organoids as an in vitro model of human development and disease," *Nature Cell Biology*, vol. 18, no. 3. Nature Publishing Group, pp. 246–254, Feb. 25, 2016. doi: 10.1038/ncb3312.

[14] M. Huch and B. K. Koo, "Modeling mouse and human development using organoid cultures," *Development (Cambridge)*, vol. 142, no. 18. Company of Biologists Ltd, pp. 3113–3125, Sep. 23, 2015. doi: 10.1242/dev.118570.

[15] P. J. Schweiger and K. B. Jensen, "Modeling human disease using organotypic cultures," *Current Opinion in Cell Biology*, vol. 43. Elsevier Ltd, pp. 22–29, Dec. 01, 2016. doi: 10.1016/j.ceb.2016.07.003.

[16] E. R. Shamir and A. J. Ewald, "Three-dimensional organotypic culture: Experimental models of mammalian biology and disease," *Nature Reviews Molecular Cell Biology*, vol. 15, no. 10. Nature Publishing Group, pp. 647–664, Jan. 01, 2014. doi: 10.1038/nrm3873.

[17] F. Pampaloni, N. Ansari, P. Girard, and E. H. K. Stelzer, "Light sheet-based fluorescence microscopy (LSFM) reduces phototoxic effects and provides new means for the modern life sciences," in *Optics InfoBase Conference Papers*, 2011. doi: 10.1117/12.889443.

[18] P. P. Laissue, R. A. Alghamdi, P. Tomancak, E. G. Reynaud, and H. Shroff, “Assessing phototoxicity in live fluorescence imaging,” *Nature Methods*, vol. 14, no. 7. Nature Publishing Group, pp. 657–661, Jun. 29, 2017. doi: 10.1038/nmeth.4344.

[19] M. Jemielita, M. J. Taormina, A. Delaurier, C. B. Kimmel, and R. Parthasarathy, “Comparing phototoxicity during the development of a zebrafish craniofacial bone using confocal and light sheet fluorescence microscopy techniques,” *J Biophotonics*, vol. 6, no. 11–12, pp. 920–928, Dec. 2013, doi: 10.1002/jbio.201200144.

[20] J. Swoger, M. Muzzopappa, H. López Schier, and J. Sharpe, “4D retrospective lineage tracing using SPIM for zebrafish organogenesis studies,” *J Biophotonics*, vol. 4, no. 1–2, pp. 122–134, Jan. 2011, doi: 10.1002/jbio.201000087.

[21] T. Ichikawa *et al.*, “Live Imaging of Whole Mouse Embryos during Gastrulation: Migration Analyses of Epiblast and Mesodermal Cells,” *PLoS One*, vol. 8, no. 7, Jul. 2013, doi: 10.1371/journal.pone.0064506.

[22] B. Schmid *et al.*, “High-speed panoramic light-sheet microscopy reveals global endodermal cell dynamics,” *Nat Commun*, vol. 4, 2013, doi: 10.1038/ncomms3207.

[23] F. Pampaloni, N. Ansari, P. Girard, and E. H. K. Stelzer, “Light sheet-based fluorescence microscopy (LSFM) reduces phototoxic effects and provides new means for the modern life sciences,” in *Optics InfoBase Conference Papers*, 2011. doi: 10.1117/12.889443.

[24] P. J. Scherz, J. Huisken, P. Sahai-Hernandez, and D. Y. R. Stainier, “High-speed imaging of developing heart valves reveals interplay of morphogenesis and function,” *Development*, vol. 135, no. 6, pp. 1179–1187, Mar. 2008, doi: 10.1242/dev.010694.

[25] K. Mellman, J. Huisken, C. Dinsmore, C. Hoppe, and D. Y. Stainier, “Fibrillin-2b regulates endocardial morphogenesis in zebrafish,” *Dev Biol*, vol. 372, no. 1, pp. 111–119, Dec. 2012, doi: 10.1016/j.ydbio.2012.07.015.

[26] V. Trivedi, T. v. Truong, L. A. Trinh, D. B. Holland, M. Liebling, and S. E. Fraser, “Dynamic structure and protein expression of the live embryonic heart captured by 2-

photon light sheet microscopy and retrospective registration," *Biomed Opt Express*, vol. 6, no. 6, p. 2056, Jun. 2015, doi: 10.1364/boe.6.002056.

[27] R. Opitz *et al.*, "Transgenic zebrafish illuminate the dynamics of thyroid morphogenesis and its relationship to cardiovascular development," *Dev Biol*, vol. 372, no. 2, pp. 203–216, Dec. 2012, doi: 10.1016/j.ydbio.2012.09.011.

[28] P. J. Keller, A. D. Schmidt, J. Wittbrodt, and E. H. K. Stelzer, "Reconstruction of Zebrafish Early Embryonic Development by Scanned Light Sheet Microscopy." [Online]. Available: www.sciencemag.org

[29] J. H. Hoh, W. F. Heinz, and J. L. Werbin, "Spatial information dynamics during early zebrafish development," *Dev Biol*, vol. 377, no. 1, pp. 126–137, May 2013, doi: 10.1016/j.ydbio.2013.02.005.

[30] P. J. Keller, "In vivo imaging of zebrafish embryogenesis," *Methods*, vol. 62, no. 3, pp. 268–278, Aug. 2013, doi: 10.1016/j.ymeth.2013.03.015.

[31] F. Pinto-Teixeira, M. Muzzopappa, J. Swoger, A. Mineo, J. Sharpe, and H. López-Schier, "Intravital imaging of hair-cell development and regeneration in the zebrafish," *Front Neuroanat*, vol. 7, no. OCT, Oct. 2013, doi: 10.3389/fnana.2013.00033.

[32] E. Rebollo, K. Karkali, F. Mangione, and E. Martín-Blanco, "Live imaging in Drosophila: The optical and genetic toolkits," *Methods*, vol. 68, no. 1, pp. 48–59, Jun. 2014, doi: 10.1016/j.ymeth.2014.04.021.

[33] N. Jährling, K. Becker, C. Schönbauer, F. Schnorrer, and H. U. Dodt, "Three-dimensional reconstruction and segmentation of intact Drosophila by ultramicroscopy," *Front Syst Neurosci*, vol. 4, no. FEB, Feb. 2010, doi: 10.3389/neuro.06.001.2010.

[34] P. J. Keller, A. D. Schmidt, J. Wittbrodt, and E. H. K. Stelzer, "Reconstruction of Zebrafish Early Embryonic Development by Scanned Light Sheet Microscopy." [Online]. Available: www.sciencemag.org

[35] F. O. Fahrbach, P. Simon, and A. Rohrbach, “Microscopy with self-reconstructing beams,” *Nat Photonics*, vol. 4, no. 11, pp. 780–785, Nov. 2010, doi: 10.1038/nphoton.2010.204.

[36] T. A. Planchon *et al.*, “Rapid three-dimensional isotropic imaging of living cells using Bessel beam plane illumination,” *Nat Methods*, vol. 8, no. 5, pp. 417–423, May 2011, doi: 10.1038/nmeth.1586.

[37] T. Vettenburg *et al.*, “Light-sheet microscopy using an Airy beam,” *Nat Methods*, vol. 11, no. 5, pp. 541–544, 2014, doi: 10.1038/nmeth.2922.

[38] B.-C. Chen *et al.*, “Lattice light-sheet microscopy: Imaging molecules to embryos at high spatiotemporal resolution.” [Online]. Available: http://science.sciencemag.org/

[39] R. Gräf, J. Rietdorf, and T. Zimmermann, “Live cell spinning disk microscopy,” *Advances in Biochemical Engineering/Biotechnology*, vol. 95. pp. 57–75, Mar. 27, 2005. doi: 10.1007/b102210.

[40] B.-C. Chen *et al.*, “Lattice light-sheet microscopy: Imaging molecules to embryos at high spatiotemporal resolution.” [Online]. Available: http://science.sciencemag.org/

[41] C. Y. Chen *et al.*, “The applications of lattice light-sheet microscopy for functional volumetric imaging of hippocampal neurons in a three-dimensional culture system,” *Micromachines (Basel)*, vol. 10, no. 9, Sep. 2019, doi: 10.3390/mi10090599.

[42] J. Schöneberg *et al.*, “4D cell biology: big data image analytics and lattice light-sheet imaging reveal dynamics of clathrin-mediated endocytosis in stem cell–derived intestinal organoids,” *Mol Biol Cell*, vol. 29, no. 24, pp. 2959–2968, Nov. 2018, doi: 10.1091/mbc.E18-06-0375.

[43] J. R. Lakowicz, *Principles of fluorescence spectroscopy*. Springer, 2006.

[44] B. Valeur, *Molecular fluorescence : principles and applications*.

[45] J. W. Lichtman and J. A. Conchello, “Fluorescence microscopy,” *Nature Methods*, vol. 2, no. 12. pp. 910–919, Dec. 2005. doi: 10.1038/nmeth817.

[46] R. Y. Tsien, “THE GREEN FLUORESCENT PROTEIN,” 1998. [Online]. Available: www.annualreviews.org

[47] W. T. Mason, *Fluorescent and luminescent probes for biological activity*. Academic Press, 1993.

[48] A. Periasamy, *Methods in cellular imaging*. Springer, 2013.

[49] R. Rudolf, M. Mongillo, R. Rizzuto, and T. Pozzan, “Looking forward to seeing calcium,” *Nat Rev Mol Cell Biol*, vol. 4, no. 7, pp. 579–586, 2003.

[50] R. Y. Tsien, “Chapter 5 Fluorescent Indicators of Ion Concentrations.”

[51] S. Bassnett, L. Reinisch, and D. C. Beebe, “Intracellular pH measurement using single excitation-dual emission fluorescence ratios.”

[52] A. P. Demchenko, “Photobleaching of organic fluorophores: Quantitative characterization, mechanisms, protection,” *Methods and Applications in Fluorescence*, vol. 8, no. 2. IOP Publishing Ltd, 2020. doi: 10.1088/2050-6120/ab7365.

[53] I. D. Johnson, “Practical considerations in the selection and application of fluorescent probes,” *Handbook of biological confocal microscopy*, pp. 353–367, 2006.

[54] R. A. Hoebe, C. H. van Oven, T. W. J. Gadella, P. B. Dhonukshe, C. J. F. van Noorden, and E. M. M. Manders, “Controlled light-exposure microscopy reduces photobleaching and phototoxicity in fluorescence live-cell imaging,” *Nat Biotechnol*, vol. 25, no. 2, pp. 249–253, Feb. 2007, doi: 10.1038/nbt1278.

[55] H. C. Ishikawa-Ankerhold, R. Ankerhold, and G. P. C. Drummen, “Advanced fluorescence microscopy techniques-FRAP, FLIP, FLAP, FRET and FLIM,” *Molecules*, vol. 17, no. 4. pp. 4047–4132, Apr. 2012. doi: 10.3390/molecules17044047.

[56] C. de Los Santos, C. W. Chang, M. A. Mycek, and R. A. Cardullo, “FRAP, FLIM, and FRET: Detection and analysis of cellular dynamics on a molecular scale using fluorescence microscopy,” *Molecular Reproduction and Development*, vol. 82, no. 7–8. John Wiley and Sons Inc., pp. 587–604, Jul. 01, 2015. doi: 10.1002/mrd.22501.

[57] K. L. Tosheva, Y. Yuan, P. Matos Pereira, S. n. Culley, and R. Henriques, “Between life and death: Strategies to reduce phototoxicity in super-resolution microscopy,” *Journal of Physics D: Applied Physics*, vol. 53, no. 16. Institute of Physics Publishing, Apr. 15, 2020. doi: 10.1088/1361-6463/ab6b95.

[58] J. Icha, M. Weber, J. C. Waters, and C. Norden, “Phototoxicity in live fluorescence microscopy, and how to avoid it,” *BioEssays*, vol. 39, no. 8. John Wiley and Sons Inc., Aug. 01, 2017. doi: 10.1002/bies.201700003.

[59] M. M. Knight, S. R. Roberts, D. A. Lee, and D. L. Bader, “Live cell imaging using confocal microscopy induces intracellular calcium transients and cell death,” 2003, doi: 10.1152/ajpcell.00276.2002.-Isolated.

[60] J. B. Pawley, “Points, pixels, and gray levels: digitizing image data,” *Handbook of biological confocal microscopy*, pp. 59–79, 2006.

[61] W. Denk *et al.*, “Anatomical and functional imaging of neurons using 2-photon laser scanning microscopy,” *J Neurosci Methods*, vol. 54, no. 2, pp. 151–162, 1994.

[62] P. J. Verveer, J. Swoger, F. Pampaloni, K. Greger, M. Marcello, and E. H. K. Stelzer, “High-resolution three-dimensional imaging of large specimens with light sheet-based microscopy,” *Nat Methods*, vol. 4, no. 4, pp. 311–313, Apr. 2007, doi: 10.1038/nmeth1017.

[63] E. Remacha, L. Friedrich, J. Vermot, and F. O. Fahrbach, “How to define and optimize axial resolution in light-sheet microscopy: a simulation-based approach,” *Biomed Opt Express*, vol. 11, no. 1, p. 8, Jan. 2020, doi: 10.1364/boe.11.000008.

[64] B.-J. Chang, K. M. Dean, and R. Fiolka, “Systematic and quantitative comparison of lattice and Gaussian light-sheets,” *Opt Express*, vol. 28, no. 18, p. 27052, Aug. 2020, doi: 10.1364/oe.400164.

[65] Y. Shi, T. A. Daugird, and W. R. Legant, “A quantitative analysis of various patterns applied in lattice light sheet microscopy,” *Nat Commun*, vol. 13, no. 1, Dec. 2022, doi: 10.1038/s41467-022-32341-w.

[66] J. W. Hardy, *Adaptive optics for astronomical telescopes*, vol. 16. Oxford University Press on Demand, 1998.

[67] N. Ji, “Adaptive optical fluorescence microscopy,” *Nature Methods*, vol. 14, no. 4. Nature Publishing Group, pp. 374–380, 2017. doi: 10.1038/nmeth.4218.

[68] J. Liang, D. R. Williams, and D. T. Miller, “Supernormal vision and high-resolution retinal imaging through adaptive optics,” 1997.

[69] R. Aviles-Espinosa *et al.*, “Medical and biological imaging; (180.4315) Nonlinear microscopy; (190.4180) Multiphoton processes; (220.1080) Active or adaptive optics,” 2011.

[70] O. Azucena *et al.*, “Adaptive optics wide-field microscopy using direct wavefront sensing,” 2011.

[71] O. Azucena *et al.*, “Three-dimensional computation of light scattering from cells,” Cold Spring Harbor Laboratory Press, 1977. [Online]. Available: http://www.invitrogen.com/site/us/en/home/support/Research-Tools/Fluorescence-SpectraViewer.reg.us.html,

[72] R. Jorand *et al.*, “Deep and clear optical imaging of thick inhomogeneous samples.,” *PLoS One*, vol. 7, no. 4, 2012, doi: 10.1371/journal.pone.0035795.

[73] M. A. A. Neil, R. Juškaitis, M. J. Booth, T. Wilson, T. Tanaka, and S. Kawata, “Adaptive aberration correction in a two-photon microscope,” *J Microsc*, vol. 200, no. 2, pp. 105–108, 2000, doi: 10.1046/j.1365-2818.2000.00770.x.

[74] W. Lubeigt, S. P. Poland, G. J. Valentine, A. J. Wright, J. M. Girkin, and D. Burns, “Search-based active optic systems for aberration correction in time-independent applications,” 2010.

[75] P. N. Marsh, D. Burns, J. M. Girkin, D. S. Wan, M. Rajadhyaksha, and R. H. Webb, “Practical implementation of adaptive optics in multiphoton microscopy,” 2003. [Online]. Available: http://www.photonics.ac.uk/

[76] C. Bourgenot *et al.*, “Active or adaptive optics; (110.1085) Adaptive imaging; (110.0180) Microscopy,” 2009.

[77] D. Débarre, E. J. Botcherby, T. Watanabe, S. Srinivas, M. J. Booth, and T. Wilson, “180.2520, 180.6900, 180.4315, 170.3880,” 2009.

[78] D. Débarre, E. J. Botcherby, M. J. Booth, and T. Wilson, “Adaptive optics for structured illumination microscopy,” 2008.

[79] M. Pedrazzani, V. Loriette, P. Tchenio, S. Benrezzak, D. Nutarelli, and A. Fragola, “Sensorless adaptive optics implementation in widefield optical sectioning microscopy inside in vivo Drosophila brain,” 2016, doi: 10.1117/1.

[80] O. Albert, L. Sherman, G. Mourou, T. B. Norris, and G. Vdovin, “Smart microscope: an adaptive optics learning system for aberration correction in multiphoton confocal microscopy,” 2000.

[81] N. Ji, D. E. Milkie, and E. Betzig, “Adaptive optics via pupil segmentation for high-resolution imaging in biological tissues,” *Nat Methods*, vol. 7, no. 2, pp. 141–147, Feb. 2010, doi: 10.1038/nmeth.1411.

[82] M. G. L G U S Ta F S S O N, D. A. Ag A R D, and J. W. S E Dat, “Phase-retrieved pupil functions in wide-field fluorescence microscopy,” 2004.

[83] N. Ji, D. E. Milkie, and E. Betzig, “Adaptive optics via pupil segmentation for high-resolution imaging in biological tissues,” *Nat Methods*, vol. 7, no. 2, pp. 141–147, Feb. 2010, doi: 10.1038/nmeth.1411.

[84] R. E. Mino, Z. Chen, M. Mettlen, and S. L. Schmid, “An internally eGFP-tagged α-adaptin is a fully functional and improved fiduciary marker for clathrin-coated pit dynamics,” *Traffic*, vol. 21, no. 9, pp. 603–616, Sep. 2020, doi: 10.1111/tra.12755.

[85] “Endocytosis by Random Initiation and Stabilization of Clathrin-Coated Pits.” [Online]. Available: http://www.cell.com/cgi/content/full/

[86] Y. Narimatsu *et al.*, “A validated gRNA library for CRISPR/Cas9 targeting of the human glycosyltransferase genome,” *Glycobiology*, vol. 28, no. 5, pp. 295–305, May 2018, doi: 10.1093/glycob/cwx101.

[87] J. G. Doench *et al.*, “Optimized sgRNA design to maximize activity and minimize off-target effects of CRISPR-Cas9,” *Nat Biotechnol*, vol. 34, no. 2, pp. 184–191, Feb. 2016, doi: 10.1038/nbt.3437.

[88] F. A. Ran, P. D. Hsu, J. Wright, V. Agarwala, D. A. Scott, and F. Zhang, “Genome engineering using the CRISPR-Cas9 system,” *Nat Protoc*, vol. 8, no. 11, pp. 2281–2308, 2013, doi: 10.1038/nprot.2013.143.

[89] N. E. Sanjana, O. Shalem, and F. Zhang, “Improved vectors and genome-wide libraries for CRISPR screening,” *Nature Methods*, vol. 11, no. 8. Nature Publishing Group, pp. 783–784, 2014. doi: 10.1038/nmeth.3047.

[90] P. Stanley, “Golgi glycosylation,” *Cold Spring Harb Perspect Biol*, vol. 3, no. 4, pp. 1–13, Apr. 2011, doi: 10.1101/cshperspect.a005199.

[91] E. Ioffe and P. Stanley, “Mice lacking N-acetylglucosaminyltransferase I activity die at mid-gestation, revealing an essential role for complex or hybrid N-linked carbohydrates (glycobiology/homologous recombiation/glycosyltransferase gene/mouse development),” 1994. [Online]. Available: https://www.pnas.org

[92] M. Metzler, A. Gertz, M. Sarkar, H. Schachter, J. W.schrader, and J. D. Marth, “Complex asparagine-linked oligosaccharides are required for morphogenic events during post-implantation development,” *EMBO Journal*, vol. 13, no. 9, pp. 2056–2065, 1994, doi: 10.1002/j.1460-2075.1994.tb06480.x.

[93] S. Dabelsteen *et al.*, “Essential Functions of Glycans in Human Epithelia Dissected by a CRISPR-Cas9-Engineered Human Organotypic Skin Model,” *Dev Cell*, vol. 54, no. 5, pp. 669-684.e7, Sep. 2020, doi: 10.1016/j.devcel.2020.06.039.

[94] I. N. Marinova, H. H. Wandall, and S. Dabelsteen, “Protocol for CRISPR-Cas9 modification of glycosylation in 3D organotypic skin models,” *STAR Protoc*, vol. 2, no. 3, Sep. 2021, doi: 10.1016/j.xpro.2021.100668.

[95] S. Dabelsteen, P. Hercule, P. Barron, M. Rice, G. Dorsainville, and J. G. Rheinwald, “Epithelial cells derived from human embryonic stem cells display P16 INK4A senescence, hypermotility, and differentiation properties shared by many P63+ somatic cell types,” *Stem Cells*, vol. 27, no. 6, pp. 1388–1399, Jun. 2009, doi: 10.1002/stem.64.

[96] J. Y. Tinevez *et al.*, “TrackMate: An open and extensible platform for single-particle tracking,” *Methods*, vol. 115, pp. 80–90, Feb. 2017, doi: 10.1016/j.ymeth.2016.09.016.

[97] D. Ershov *et al.*, “TrackMate 7: integrating state-of-the-art segmentation algorithms into tracking pipelines,” *Nat Methods*, vol. 19, no. 7, pp. 829–832, Jul. 2022, doi: 10.1038/s41592-022-01507-1.

[98] A. C. Hundahl *et al.*, “Quantitative live-cell imaging of lipidated peptide transport through an epithelial cell layer,” *Journal of Controlled Release*, vol. 355, pp. 122–134, Mar. 2023, doi: 10.1016/j.jconrel.2023.01.066.

[99] T. L. Liu *et al.*, “Observing the cell in its native state: Imaging subcellular dynamics in multicellular organisms,” *Science (1979)*, vol. 360, no. 6386, Apr. 2018, doi: 10.1126/science.aaq1392.

[100] D. Boiroux, Y. Oke, F. Miwakeichi, and Y. Oku, “Pixel timing correction in time-lapsed calcium imaging using point scanning microscopy,” *J Neurosci Methods*, vol. 237, pp. 60–68, Nov. 2014, doi: 10.1016/j.jneumeth.2014.08.008.

[101] B. R. Masters *et al.*, “Mitigating thermal mechanical damage potential during two-photon dermal imaging,” *J Biomed Opt*, vol. 9, no. 6, p. 1265, 2004, doi: 10.1117/1.1806135.

[102] A. Hopt and E. Neher, “Highly nonlinear photodamage in two-photon fluorescence microscopy,” *Biophys J*, vol. 80, no. 4, pp. 2029–2036, 2001, doi: 10.1016/S0006-3495(01)76173-5.

[103] R. P. Moore *et al.*, “A multi-functional microfluidic device compatible with widefield and light sheet microscopy,” *Lab Chip*, vol. 22, no. 1, pp. 136–147, Jan. 2022, doi: 10.1039/d1lc00600b.

[104] J. Jonkman, C. M. Brown, G. D. Wright, K. I. Anderson, and A. J. North, “Guidance for quantitative confocal microscopy,” *Nat Protoc*, Mar. 2020, doi: 10.1038/s41596-020-0307-7.

[105] N. López-Gil *et al.*, “Effect of third-order aberrations on dynamic accommodation,” *Vision Res*, vol. 47, no. 6, pp. 755–765, Mar. 2007, doi: 10.1016/j.visres.2006.08.010.

Chapter 10. Appendix

10.1 Excitation/Emission spectra of markers

Figure 10.1 shows the excitation and emission spectra of the markers used in the experiments.

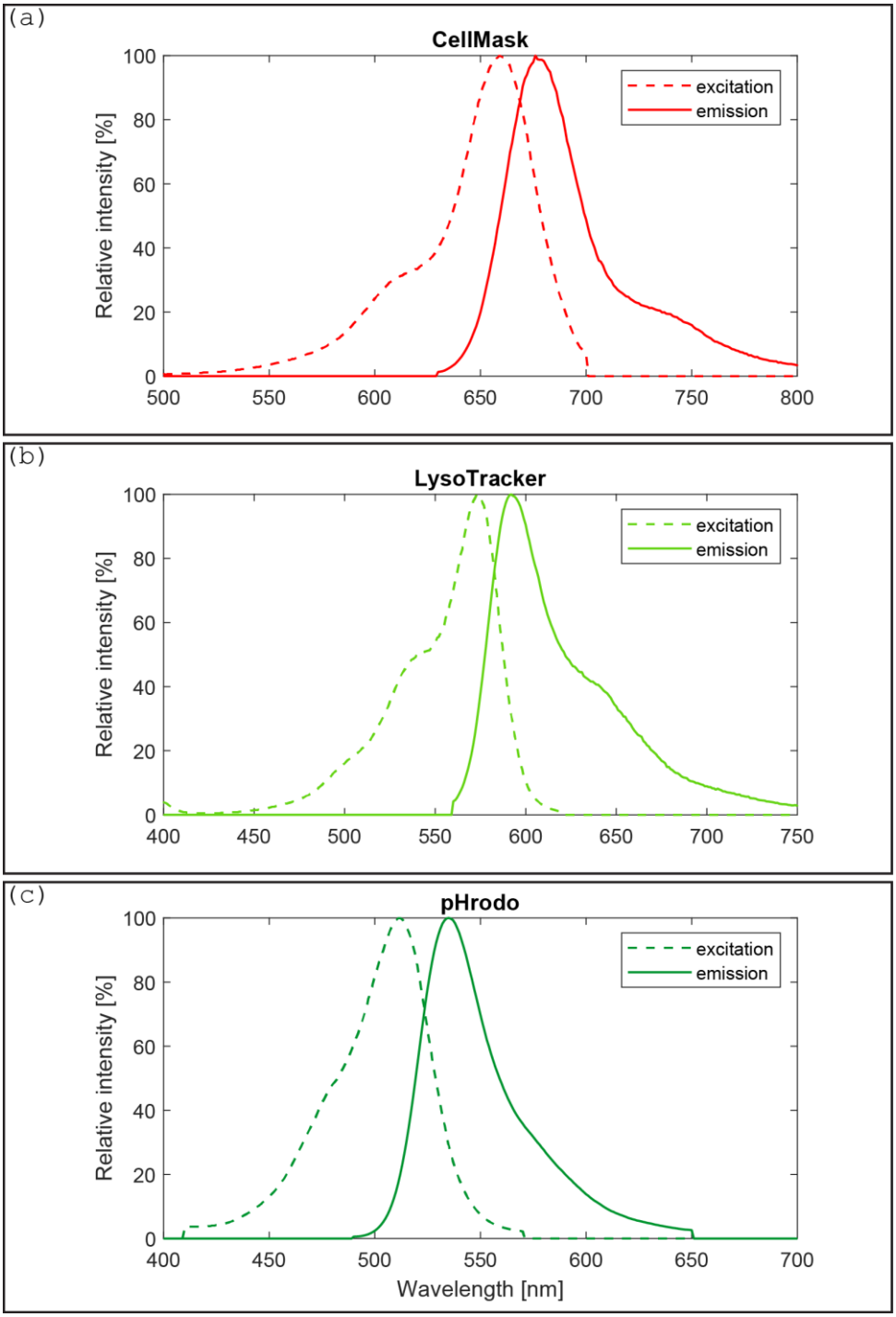

Figure 10.1.Excitation/Emission spectra. (a) *CellMask.* ***(b)*** *Lysotracker.* ***(c)*** *pHrodo.*

10.2 Bead gluing protocol

The beads for calibrating the instrument were glued to the cover glass by first pipetting 10 µL Poly-L-lysine (PLL) 0.1% w/v in H_2O on the center of a circular coverglass. Then, PLL was allowed to dry for 15 min. Next, the cover glass was washed with Milli-Q water. It was allowed to dry for 15 min. Then, 10 µL of 0.1 µm FluoSpheres™ beads diluted to about 10^6 particles/mL was pipetted on the coverglass. Finally, the sample was left to dry further for 15 min.

10.3 Bead PSF

Figure 10.2, **Figure 10.3**, and **Figure 10.4** show the axial PSFs for the spinning disk, deskewed LLS stack, and processed LLS stack, respectively.

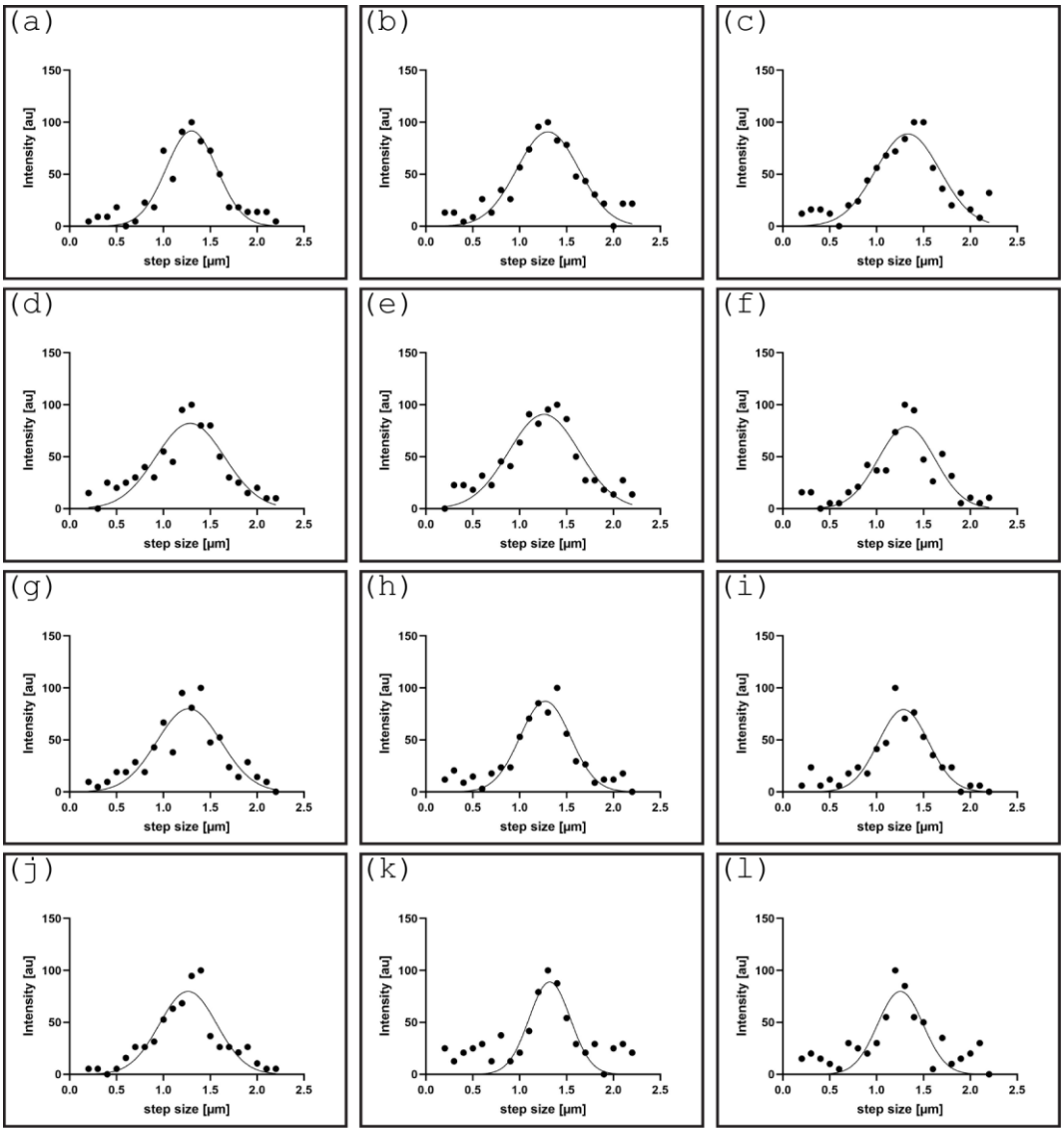

Figure 10.2 Gaussian fit for the z-linescan of the beads captured with the spinning disk. *The z-axis is orthogonal to the coverglass and parallel to the optical axis of the objective.*

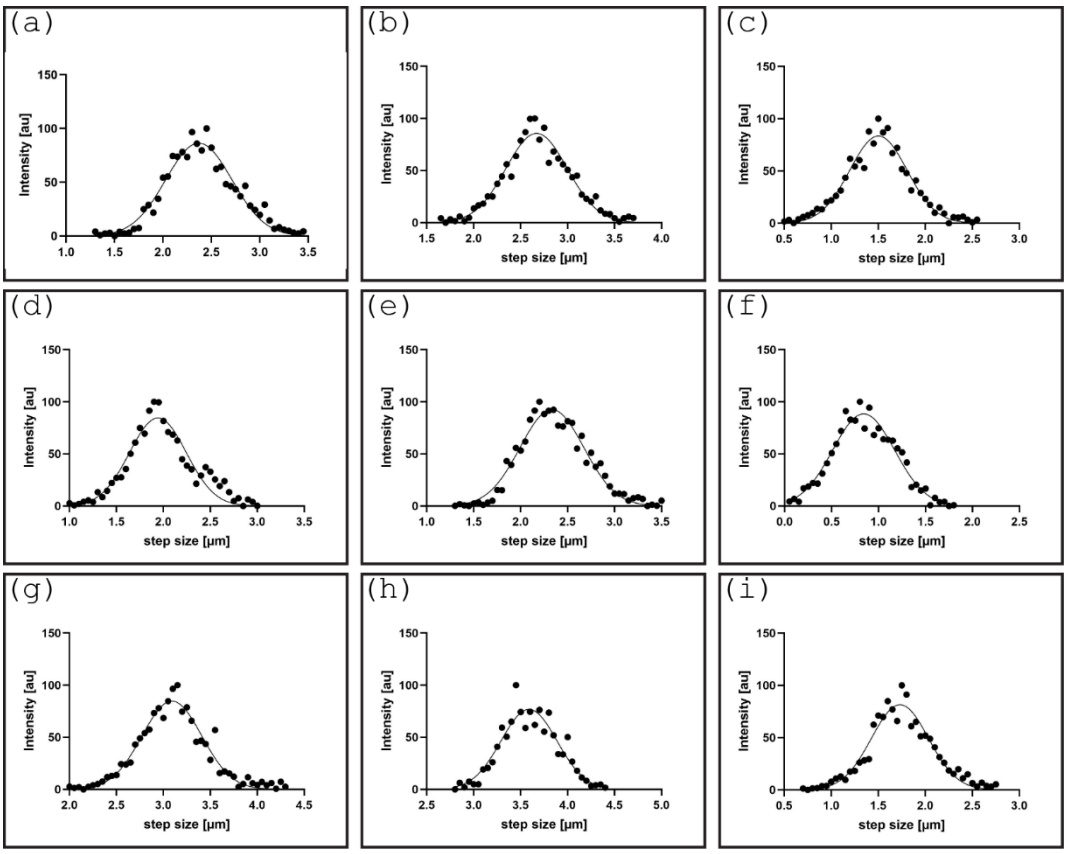

Figure 10.3 Gaussian fit to the z-linescan of the beads in the deskewed LLS stack. *The z-axis is parallel with the optical axis of the detection objective.*

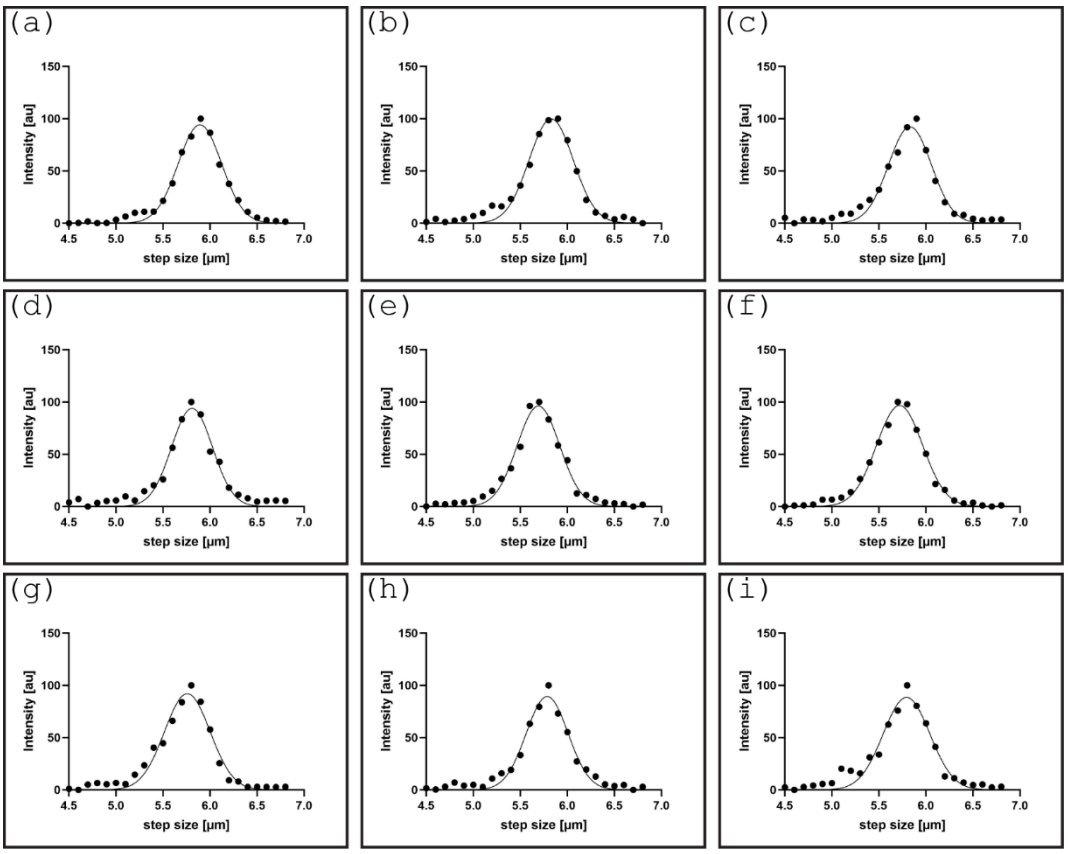

Figure 10.4. Gaussian fit to the z-linescan of the beads in the processed LLS stack. *The z-axis is orthogonal to the coverglass.*

10.4 LLS thickness measurement

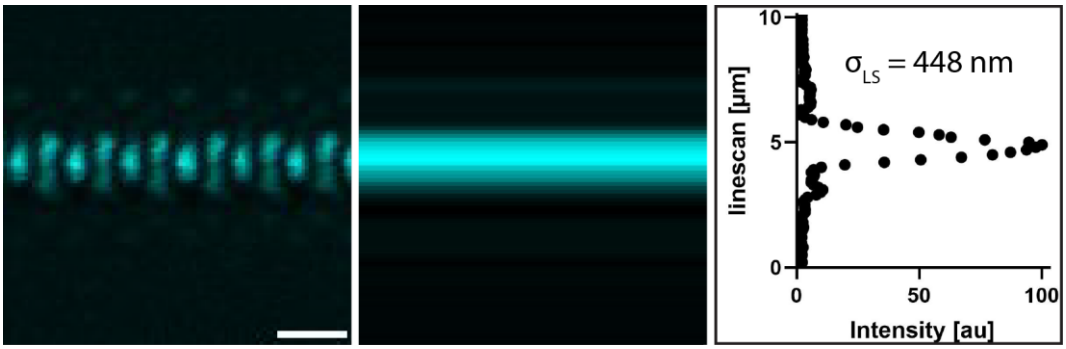

Figure 10.5. Thickness measurement of the LLS. (a) *Cross section of the excitation light.* ***(b)*** *Sum of horizontal pixels.* ***(c)*** *Standard deviation of the best fit Gaussian function applied to the thickness of the light-sheet. This is for a light-sheet with length 26.5 µm. The scalebar is 2 µm.*

10.5 Analytical expression for the apparent z-resolution in the sample coordinates in the LLS

I calculated the apparent z-resolution of the LLS by calculating the height of the rotated ellipse defined by the real PSF of the LLS. A schematic of the configuration is shown in **Figure 10.6**.

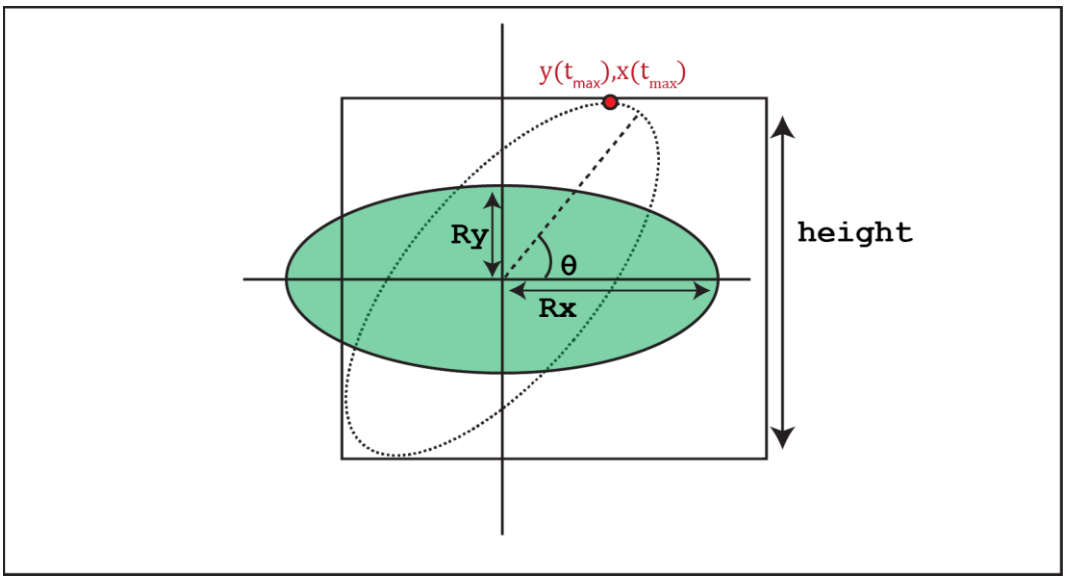

Figure 10.6 Rotated ellipse. *The apparent z-PSF can be calculated from the height of the ellipse defined by the real PSF.*

The parametric equation of an ellipse centered at the origin with radius R_x and R_y is given by,

$$x(t) = R_x \cos(t)$$

$$y(t) = R_y \sin(t)$$

For the same ellipse rotated θ counter-clockwise with respect to the x-axis,

$$x(t) = R_x \cos(t)\cos(\theta) - R_y \sin(t)\sin(\theta)$$

$$y(t) = R_x \cos(t)\sin(\theta) + R_y \sin(t)\cos(\theta)$$

To get the height H, I solve for the parameter t, that optimizes $y(t)$,

$$\frac{dy}{dt} = 0 = R_y \cos(\theta)\cos(t) - Rx \sin(\theta)\sin(t)$$

giving,

$$t_{max} = \tan^{-1}\left(\frac{R_y}{R_x \tan(\theta)}\right)$$

The height is thus $2y(t_{max})$,

$$H = 2y(t_{max}) = 2R_x \cos(t_{max}) \sin(\theta) + 2R_y \sin(t_{max}) \cos(\theta) .$$

10.6 Article in Proceedings Volume 11786, Optical Methods for Inspection, Characterization, and Imaging of Biomaterials V; 117861R (2021)

Imaging complex organ-on-chip systems

J. P. C. Narag[1], N. Taebnia[1], R. Zhang[1], T. L. Andresen[1], N. B. Larsen[1], E. B. Kromann*[1]
[1]Center for Intestinal Absorption and Transport of Biopharmaceuticals,
Department of Health Technology, Technical University of Denmark,
Ørsteds Plads 345C, Kgs. Lyngby, Denmark DK-2800

*ebkro@dtu.dk

ABSTRACT

Oral drug delivery is a preferred method for drug administration because it is economical and convenient to the patient [1]. Uptake from the gut to the blood is mediated by the intestinal barrier, which exhibits some selectivity, i.e., mechanisms in the intestinal barrier define which compounds are absorbed and which are not. The limited understanding of these mechanisms impedes the design and development of new oral drugs. On the horizon: Emerging organ-on-chip models of the intestine may provide new insights into structure-function relationships in biological barriers like the gut-blood interface of the intestine. These small 'artificial organs' can host live cells, which mimic the natural behavior of intestinal cells, thus providing a highly controlled platform for fundamental bioresearch and, ultimately, drug-screening [2]. Our groups develop and implement optical imaging technologies specifically geared for imaging organ-on-chip systems. At the SPIE conference "Optical Methods for Inspection, Characterization, and Imaging of Biomaterials V" we will present the application of two-photon microscopy for imaging of relatively thick 3D printed organ-on-chip systems and discuss imaging-challenges related to sample-induced aberrations [3]. We will also present our ongoing work to implement an adaptive optics-enabled lattice light sheet microscope [4], which (we anticipate) will enable long-term, high-resolution imaging inside complex organ-on-chip systems by reducing phototoxicity and compensating sample-induced aberrations.

Keywords: Optical microscopy, optical aberrations, organ-on-chip

1. INTRODUCTION

To advance fundamental and application-oriented research in biology we need tools to observe biological structures and processes as they unfold in living, multicellular, specimens. Traditional bioresearch has taken departure in observations of cells either in monolayers or in whole tissues (excised or intact in animals). As such, researchers have primarily worked at the polar extremes of model system ease and scalability (*high in monolayers; low in tissues*) and biological relevance (*low in monolayers; high in tissues*). Emerging organ-on-chip systems represent a middle ground abundant with research potential, particularly for simultaneous probing of compound-cell interactions, cell-cell interactions, and structure-function relationships governed by the spatial organization of cells. In short, organ-on-chip systems aim to recapitulate the natural structure of organs and their spatial distribution of different cell types [5]. While somewhat akin to organoids in an application-perspective, organ-on-chip systems always comprise a synthetic scaffold and/or enclosure, with a limited number of access points (like input/output-pins in a chip), which can support the formation of complex biological structures, deliver nutrients during differentiation and maturation, and provide a well-defined window for sample observation, as key examples. The potential advantages and applications of organ-on-chip systems are many. Yet, the organ-on-chip technology is still young, and its further development hinges on improved techniques for manufacturing the synthetic chips, improved techniques for maturing cells inside the chips, and (as we explore here) improved techniques for observing structures and processes in the resulting organ-mimics, both during development and application.

Many organ-on-chip systems comprise only two near-parallel flow channels that run very close to each other, thus allowing to form a chemical gradient across cells between the two channels, e.g. [6]. These systems are, by design, relatively straightforward to image. However, the structural complexity of organ-on-chip systems is increasing rapidly with the advent of microscale 3D printing techniques. Using high-resolution stereolithography, we have prototyped an

organ-on-chip system that mimics the intestinal barrier in the human small intestine. The purpose of this system is to enable early-stage screening of metabolites and new drug candidates for oral drug delivery, i.e., a testbed for observing whether introduced compounds traverse the intestinal barrier or not. In the human small intestine, a strong chemical gradient exists between the lumen of the intestine and the base of the finger-like protrusions, villi, densely present on the small intestine to increase its surface-area. By recapitulating these villi in an organ-on-chip system, we place a high demand on imaging capacity: (1) The synthetic villi are relatively large (500 µm height, 350 µm diameter), thus posing a need for fast 3D imaging, (2) Repeated observation is required during week- to month-long maturation, thus prohibiting the use of destructive observation methods, and (3) The specimen is thick and its index of refraction (RI~1.36) does not accurately match the culture medium (~1.33), thus introducing optical aberrations. The effects of the last item, optical aberrations, is demonstrated in **Figure 1a**, which shows a 3D-printed test-sample (details below). This pyramid-shaped sample has two sides with low inclination angle and two sides that are relatively steep. On the steep sides, the fluorescence signal is lost relatively fast as imaging depth increases. **Figure 1b** clarifies how this loss of signal results from sample-induced optical aberrations, which distort the laser focus and reduces the peak-intensity below levels required for two-photon excitation.

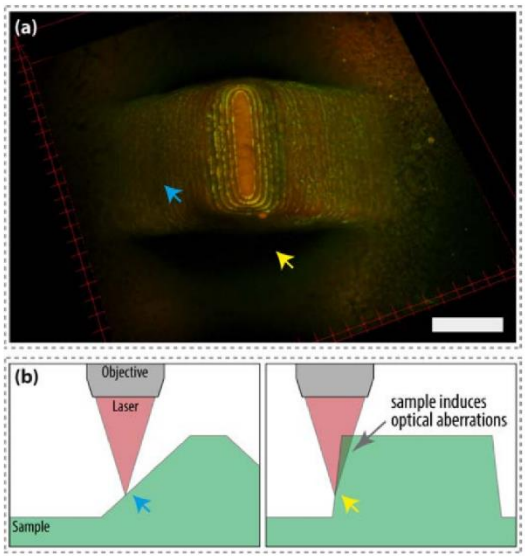

Figure 1. (a) Test-sample: 3D printed hydrogel seeded with Caco-2 cells (two-photon excitation, NA = 1.0, scalebar = 200 µm). Sample-induced optical aberrations reduce fluorescence signal from the steep sides of the sample (dark area indicated by yellow arrow). **(b)** Schematic showing why optical aberrations are more pronounced on the steep sides (right, yellow arrows) of the sample compared to the sides with lower inclination angles (left, blue arrows).

While the test sample shown here has little relevance in a biological context, the obvious loss of signal near the steep sides of the sample presents a significant challenge for routine imaging of stratified 3D-printed hydrogels using two-photon microscopy. Additionally, two-photon microscopy can induce significant photodamage and phototoxicity, which is unacceptable for repeated imaging of organ-on-chip systems that mature at long time scales (weeks or months). As discussed here, we may find a sound alternative to two-photon microscopy in light sheet microscopy (for reducing sample exposure) and adaptive optics (for compensating sample-induced aberrations) [7,8].

2. METHODOLOGY AND RESULTS

2.1 Organ-on-chip system with morphological and functional characteristics mimicking the intestinal barrier.

We produced a hydrogel-based organ-on-chip system using high-resolution projection stereolithography [2,9]. In short, this method enables fabrication of three-dimensional (3D) structures, by exposing a photo-crosslinkable liquid resin (20%w/v poly(ethylene glycol) diacrylate (PEGDA), molar weight M_n 700 g/mol) to ultraviolet light (365 nm) in a layer-by-layer fashion. During production, a digital micromirror device (Texas Instruments, DLP9500 UV, DMD) adjusts the light exposure profile dynamically, thus solidifying the resin only in targeted regions of each new layer with an effective 3D-printing resolution of W×D×H ~ 10×10×20 μm^3 [2]. We printed a hydrogel structure with dimensions mimicking villi in the human small intestine and seeded it with Caco-2 cells. We cultured the sample for up to 45 days and confirmed barrier integrity between the basal and apical side [Manuscript in preparation]. Finally, for imaging, we fixed the sample and stained for nucleic acid (cell nuclei) and zonula occludens-1 (ZO-1; associated with tight junctions).

2.2 Imaging with two-photon microscopy.

Referencing schematics from Rosenegger *et al.* [3], we constructed an upright two-photon laser-scanning microscope comprising a tunable femtosecond laser (Coherent, Chameleon Discovery TPC), two galvanometric scanning mirrors (Cambridge Technology, 6210HM40), two detectors (Thorlabs, PMT2101/M), and a long working distance objective (Olympus, XLPLN25XSVMP2: 25X, 1.0 NA, 4 mm WD). For imaging, we used two-photon excitation wavelengths of 980 and 1100 nm for excitation of green- and red-light emitting fluorophores, respectively. Fluorescence was directed to the detectors via two dichroic filters (Semrock, FF735-Di02-25x36; Chroma T560lpxr) and two detection bands (Chroma, ET525/50m [for ZO-1; displayed in green color] and ET605/70m [for nuclei; displayed in blue color]). We used the built-in dispersion compensator (in the laser) to optimize signal intensity while imaging the organ-on-chip prototype (a single villus structure) shown in **Figure 2**.

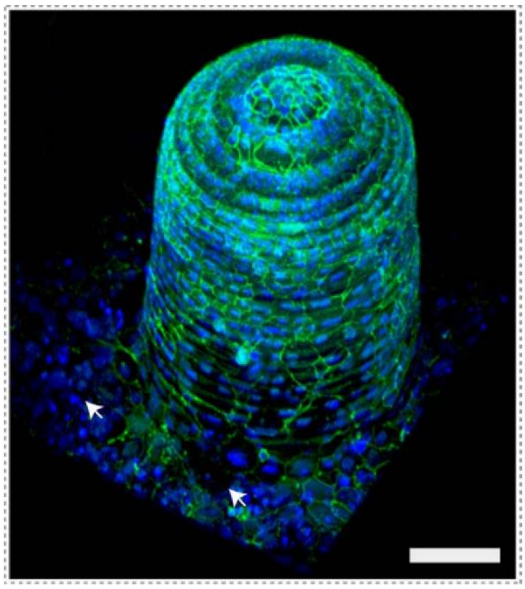

Figure 2. 3D representation of image-stack capturing a 3D printed hydrogel mimicking a villus in the small intestine. Fluorescence-labeled Caco-2 cells cover the surface of the hydrogel (nucleic acid = blue, ZO-1 = green). White arrows indicate regions where ZO-1 (tight junctions) is either absent or not captured due to sample-induced aberrations. Two-photon excitation, NA = 1.0, scalebar = 100 µm.

2.3 Implementing an adaptive optics enabled lattice light sheet microscope.

Seeing that two-photon microscopy does not consistently allow imaging deep into our 3D printed samples (**Figures 1,2**), we are now implementing a light sheet microscope, which others have shown to be applicable for long-term, thick-sample 3D imaging [4]. Specifically, we are following schematics from the Betzig Lab (Janelia Research Campus, VA, USA) detailing a new microscope-iteration that allows quick toggling between multiple different imaging modes, including two-photon imaging and light sheet imaging. Down the road, this will allow a more direct and 'fairer' comparison of how different optical imaging modalities perform in our organ-on-chip systems. At present, our primary interest lies with the adaptive optics-enabled light sheet imaging mode, which allows beam forming and aberration correction in the excitation path (using a spatial light modulator) and aberration correction in the detection path (using a deformable mirror). While we have not yet used this microscope to image our organ-on-chip systems, preliminary tests show acceptable excitation beam profiles (**Figure 3a**), and a detection point-spread function (PSF), which is readily improved by correcting system aberrations with adaptive optics. Finally, the combination of adaptive optics and light-sheet illumination produces a good imaging PSF (**Figure 3b**), suitable for imaging fluorescent beads embedded in hydrogels akin to the material used for organ-on-chip manufacturing (**Figure 3c**).

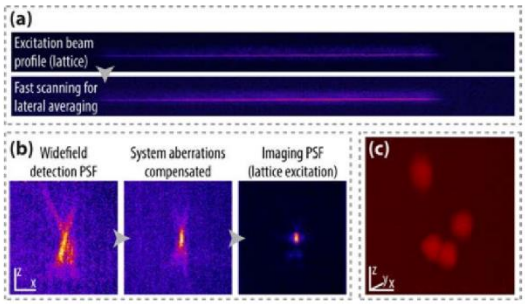

Figure 3. Preliminary characterization of light sheet microscope for imaging hydrogels. **(a)** Excitation beam profile without (top) and with (bottom) fast scanning for lateral averaging of the profile. Wavelength = 488 nm. **(b)** PSFs acquired by scanning a fluorescent bead (100 nm) along the optical axis of the detection objective (z-axis). Insets from left to right: (i) Maximum-intensity projection of 3D image stack capturing the fluorescent bead under widefield illumination prior to aberration correction, (ii) Same bead imaged after aberration correction (only system-aberrations), and (iii) Same bead imaged with lattice light-sheet illumination. The final inset (iii) represents the imaging PSF. Scalebars = 200 nm. **(c)** 3D representation of image-stack: Very large fluorescent beads (2 µm) embedded in a hydrogel. Scalebar = 2 µm.

3. DISCUSSION

Organ-on-chip technology represents an exciting avenue for exploring biology and for informing the development of new medicines. While two-photon (or multi-photon) imaging has been the gold standard for imaging thick and inhomogeneous specimens, we find that this imaging modality does not reliably enable high-resolution imaging of our structurally complex organ-on-chip prototypes. The likely cause of this shortfall is sample-induced optical aberrations. Additionally, we are weary of photodamage and phototoxic effects imparted by the high-powered (and focused) two-photon laser. Given these (potential) drawbacks of two-photon microscopy and the relatively long image acquisition-time inherent to point-scanning methods, it seems the obvious choice to try light sheet imaging instead. In doing this, we must avoid jumping to conclusions by treating the adaptive optics technology separately from light sheet imaging modality. We may well find that adaptive optics enabled multi-photon imaging yields the best possible images (although image acquisition will remain relatively slow). While pursuing the modality best suited for imaging our organ-on-chip

systems, it is worth keeping in mind that we may also optimize the shape of the organ-on-chip system to improve imaging performance, for example, by ensuring that light enters the sample through flat surfaces perpendicular to the optical axis of the objective(s). For light sheet microscopy (which uses two objectives), this would require a wedge-shaped organ-on-chip system. Additionally, we must investigate whether the 3D printing method can be optimized to produce structures with a more homogenous index of refraction. Currently, the pixelated format of the DMD in the 3D printer does introduce a greater degree of crosslinking (and so, a greater index of refraction) near pixel centers, compared to the pixel edges, where small gaps between neighboring mirrors are present. Hence, an upgrade of the 3D printing system may improve the optical clarity of the sample. In conclusion, the increasing complexity of organ-on-chip systems poses a need for a careful comparison of existing thick-sample imaging instruments and for new thinking to improve not only the imaging instrument but also the organ-on-chip system itself to optimize image quality.

ACKNOWLEDGEMENTS

The work presented in this article is supported by Novo Nordisk Foundation grants NNF16OC0022166 (Challenge Programme) and NNF20OC0059893 (New Explorative Research and Discovery).

REFERENCES

[1] P. Viswanathan, Y. Muralidaran, and G. Ragavan, *Challenges in oral drug delivery: a nano-based strategy to overcome*, Nanostructures for Oral Medicine, Elsevier, 173-201 (2017)
[2] R. Zhang and N.B. Larsen, *Stereolithographic hydrogel printing of 3D culture chips with biofunctionalized complex 3D perfusion networks*, Lab on a Chip, 24, 4273-4282 (2017)
[3] D. G. Rosenegger *et al.*, *A high performance, cost-effective, open-source microscope for Scanning two-photon microscopy that is modular and readily adaptable*, PLoS ONE, e110475 (2014)
[4] T. Liu, S. Upadhyayula, *et al.*, *Observing the cell in its native state: Imaging subcellular dynamics in multicellular organisms*, Science, eaaq1392 (2018)
[5] L. A. Low *et al.*, *Organs-on-chips: Into the next decade.* Nature Reviews Drug Discovery, 20, 345–361 (2021)
[6] C. Blundell *et al.*, *Placental Drug Transport-on-a-Chip: A microengineered in vitro model of transporter-mediated drug efflux in the human placental barrier*, Adv. Healthcare Mater., 7, 1700786 (2018)
[7] A. H. Voie, D. H. Burns, and F. A. Spelman, *Orthogonal-plane fluorescence optical sectioning: Three-dimensional imaging of macroscopic biological specimens*, Journal of Microscopy, 170, 229-236 (1993)
[8] M. J. Booth, *Adaptive optical microscopy: The ongoing quest for a perfect image*, Light: Science & Applications 3, e165 (2014)
[9] Y. Lu *et al.*, *A digital micro-mirror device-based system for the microfabrication of complex, spatially patterned tissue engineering scaffolds*, J. Biomed. Mater. Res. A, 77, 396–405 (2006)